



Simon Prato

# Numerical Investigation of TEM Cells and Antenna Coupling

**Master Thesis**

Studies: Electrical Engineering

submitted to

**Technical University of Graz**

Supervisor

Dr. Thomas Bauernfeind



Graz, August 2024

## **Abstract**

# Contents

<b>1</b>	<b>Introduction</b>	<b>1</b>
<b>2</b>	<b>Dipole Theory</b>	<b>1</b>
2.1	Electric Dipoles . . . . .	1
2.1.1	Infinitesimal Electric Dipoles . . . . .	1
2.1.2	Small Electric Dipoles . . . . .	3
2.2	Magnetic Dipoles . . . . .	5
2.3	Crossed Dipoles . . . . .	7
2.4	Radiated Field . . . . .	7
2.5	Field regions . . . . .	7
<b>3</b>	<b>Guided Waves</b>	<b>9</b>
3.1	Lorentz Reciprocity Theorem . . . . .	9
3.2	Green's Function . . . . .	10
3.2.1	Scalar Green's Function . . . . .	10
3.2.2	Dyadic Green's Function . . . . .	11
3.3	Modes in a TEM Cell . . . . .	13
3.3.1	Rectangular Waveguides as non-TEM structures . . . . .	13
3.3.2	TEM mode in the TEM cell . . . . .	14
3.3.3	Higher-order modes . . . . .	16
3.3.4	Field distributions . . . . .	19
3.4	Electrically Small Radiating Sources in TEM Cells . . . . .	22
3.4.1	Arbitrary source . . . . .	22
3.4.2	Equivalent dipole moments . . . . .	23
3.4.3	Electrically small antennas . . . . .	25
3.5	Shielding . . . . .	27
3.5.1	ASTM ES7-83 Method . . . . .	29
3.5.2	Dual TEM cell . . . . .	30
<b>4</b>	<b>Numerical Investigations</b>	<b>31</b>
4.1	Finite Element Method . . . . .	31
4.1.1	General Idea . . . . .	31
4.1.2	Dividing a computational domain into finite elements . . . . .	32
4.1.3	Solving the differential equation . . . . .	34
4.1.4	Adaptive solution process . . . . .	35
4.2	Conceptual framework and modeling of antennas . . . . .	35
4.3	Monopole Antenna . . . . .	40
4.3.1	Setup . . . . .	40
4.3.2	Equivalent dipole moments . . . . .	41
4.3.3	Electrical characteristics . . . . .	42
4.3.4	Current distribution on septum and antenna offset . . . . .	45
4.3.5	Electromagnetic energy in the TEM cell . . . . .	46
4.4	Loop antenna . . . . .	47
4.4.1	Setup . . . . .	47

4.4.2	Equivalent dipole moments . . . . .	48
4.4.3	Electrical characteristics . . . . .	48
4.4.4	Equivalent circuit model . . . . .	50
4.4.5	Current distribution on septum and higher order modes . . . . .	52
4.5	Loop antenna with gap . . . . .	55
4.5.1	Setup and geometrical analysis . . . . .	55
4.5.2	Equivalent dipole moments . . . . .	56
4.5.3	Electrical characteristics . . . . .	57
4.6	Inverted F-antenna . . . . .	58
4.7	Center Fed Monopole Antenna . . . . .	60
4.8	Dipole Moments . . . . .	62
4.8.1	Orientation and position in TEM Cell . . . . .	62
4.8.2	Combining dipole moments with antennas . . . . .	63
4.8.3	Application of dipole moments . . . . .	63
4.9	Investigation of field regions . . . . .	63
4.10	Shielding materials . . . . .	66
4.10.1	Shielding effectiveness of graphite . . . . .	66
4.10.2	Shield effectiveness of FR4 . . . . .	66
4.10.3	Dual TEM Cell . . . . .	67

## List of Figures

2.1	Geometrical arrangement of an infinitesimal electric dipole. It contains a capacitor-plate at each end of the wire to provide a constant current $\mathbf{I}(z)$ . . . . .	2
2.2	Geometrical arrangement of a linear, center-fed wire antenna with a feed-point indicated in the center. The feedpoint consists of a small gap providing current $I_0$ to the antenna. . . . .	4
2.3	Current distribution across linear wire antenna. It has a maximum at the feedpoint, and drops to zero at points $d/2$ and $-d/2$ . . . . .	5
2.4	Geometrical arrangement of a current loop fed by a current $I_0$ , producing a magnetic dipole moment. Alternatively, a magnetic current $I_m$ flows perpendicular to the loop's area along the distance $L$ , which produces an equivalent magnetic dipole moment. . . . .	6
2.5	Behavior of Expression 1 and Expression 2 in Equation 2.21 over distance $r$ . The distance $r$ is normalized to the radian distance $\lambda/2\pi$ . The magnitude of both expressions is normed to 1 at radian distance for better comparison. . . . .	8
2.6	Field regions of an antenna, here specifically a linear wire antenna. However, they are applicable for any antenna, as long as their largest dimension $d$ is known. . . . .	9
3.1	Dominant modes in a rectangular waveguide. . . . .	13
3.2	TEM cell with vertical antenna inserted . . . . .	14
3.3	Cross section of the TEM cell . . . . .	17
3.4	Propagation of TEM, TE <sub>01</sub> and TE <sub>10</sub> modes in TEM cell . . . . .	18
3.5	Transversal electric fields in cross section of TEM cell . . . . .	19
3.6	Normalized e-field distribution along z-axis at center of septum for visualization, where the y-axis is the magnitude and the x-axis is the point in the height position in the TEM cell. . . . .	20
3.7	TODO: This is how the dimensions in these formulas are defined in [28] . . . . .	20
3.8	Output power and norm. E-field over offset . . . . .	21
3.9	Output power and norm. E-field over height . . . . .	21
3.10	TEM cell with an arbitrary current source $\mathbf{J}_1$ along the curve $\tau$ . $\mathbf{E}$ and $\mathbf{H}$ are the field intensities induced by the current. $\mathbf{e}_n^+$ and $\mathbf{e}_n^-$ are outgoing fields towards both output ports of the TEM cell of arbitrary form. $\mathbf{S}$ indicates the surface, and $V$ the volume of the domain in question. . . . .	23
3.11	Incident, reflected and transmitted electric fields due to interaction with shielding material . . . . .	27
3.13	Dual TEM cell with aperture . . . . .	31
4.1	Tetrahedron with points on the edge and vertices. . . . .	32
4.2	Face of the finite element with unknowns . . . . .	33
4.3	Adaptive solution process . . . . .	35
4.4	Geometry of an antenna's feedpoint used in simulation. The antenna is fed through a waveport. This geometry leads to a port impedance of $50\Omega$ . . . . .	36
4.5	Geometrical arrangement of the TEM cell used in simulations. The front shows the xy-plane, and the side the yz-plane of the TEM cell. . . . .	37
4.6	Geometry of monopole antenna inserted into TEM cell with its electric near-field. . . . .	41

4.7	The equivalent dipole moments of the monopole antenna and the corresponding induced phase shift between the wave ports are presented in separate figures. . . . .	42
4.8	Effective electric current and effective voltage at feedpoint of monopole antenna over frequency. . . . .	42
4.9	Output power and electric field data of antenna and equivalent dipole moments	43
4.10	At 3 GHz . . . . .	44
4.11	At 1 MHz . . . . .	44
4.12	Effective electric current distribution along the monopole antenna at frequencies 1 MHz and 3 GHz . . . . .	44
4.13	Magnitude and phase of monopole antenna's impedance. . . . .	44
4.14	Chu equivalent circuit of short dipole . . . . .	45
4.15	Current surface densities at different frequencies, below and above the cut-off frequency of the $TE_{01}$ mode. . . . .	46
4.16	Peak electromagnetic energy in the TEM cell generated by the monopole antenna . . . . .	47
4.17	Geometry of loop antenna inserted into the TEM cell with its magnetic near-field. The return path leads into the conducting surface of the cell. . . . .	47
4.18	Dipole moments and phase shift of loop antenna. . . . .	48
4.19	. . . . .	48
4.20	Voltage and current at feedpoint of the loop antenna. . . . .	49
4.21	Peak currents of loop antenna at feedpoint and return path. . . . .	49
4.22	Magnitude and phase of the impedance of the current loop antenna. . . . .	50
4.23	Equivalent circuits of the small loop antenna. . . . .	50
4.24	Circuit representing the TEM cell, small loop antenna and their coupling. .	51
4.25	Equivalent dipole moments derived by the equivalent circuit compared to the dipole moments of the loop antenna in Figure 4.18a. . . . .	52
4.26	Current surface densities at different frequencies, below and above the cut-off frequency of the $TE_{01}$ mode. . . . .	53
4.27	Output power transmitted by the antenna to an output ports through the TEM and $TE_{01}$ separately over frequency. TODO: log scale, bigger frequency range . . . . .	54
4.28	Output power of the loop antenna compared with the output power produced by the dipole moments . . . . .	54
4.29	Geometry of loop antenna with a gap in the return path inserted in the TEM cell. . . . .	55
4.30	Dipole moments and phase shift of loop antenna . . . . .	56
4.31	Comparison of dipole moments and output power at different gap heights. .	57
4.32	Dipole moments and phase shift of loop antenna . . . . .	57
4.34	Inverted F-antenna used in the simulation . . . . .	58
4.35	Dipole moments and phase shift of loop antenna . . . . .	59
4.36	Output power and electric field at output. . . . .	59
4.37	Voltage and current at feedpoint of inverted-F antenna. . . . .	60
4.38	Phase and magnitude of the inverted-F antenna's impedance over frequency.	60
4.39	Center fed monopole antenna used in simulation . . . . .	61
4.40	Phase shift . . . . .	61

4.41	Dipole moments . . . . .	61
4.42	Output power and electric field of center-fed monopole antenna . . . . .	62
4.43	Magnitude and phase of center-fed monopole antenna's impedance. . . . .	62
4.44	Voltage and current at feedpoint of center-fed monopole antenna. . . . .	62
4.45	Comparison of normalized output power of electric dipole moments . . . . .	63
4.46	TEM cell containing dipole moments . . . . .	64
4.47	Moments in small TEM cell . . . . .	64
4.48	Moments in normal TEM cell . . . . .	64
4.49	$k \cdot r$ in small TEM cell . . . . .	65
4.50	$k \cdot r$ for other TEM cells . . . . .	65
4.51	Output powers . . . . .	65
4.52	Phase shifts . . . . .	65
4.53	Shielding effectiveness of graphite . . . . .	66

## **List of Tables**

1	Cut-off frequencies of higher order modes depending on TEM cell dimensions	19
2	Forward transmission coefficients . . . . .	67

## 1 Introduction

## 2 Dipole Theory

Magnetic and electric dipoles are an effective approach for modeling the radiation of electrically small antennas. They are defined as antennas with dimensions much less than one-tenth of the wavelength ( $l \ll \lambda$ )[2, p. 151]. By calculating the respective dipole moments, the coupling between antennas and TEM cells can be numerically estimated. This section provides a brief introduction to the underlying theory of this concept.

Explanation  
Dipole  
Moments  
modeling,  
antennas  
and fields

### 2.1 Electric Dipoles

#### 2.1.1 Infinitesimal Electric Dipoles

An electric dipole can be modeled as two tiny charged metal spheres or two capacitor-plates connected by a linear wire of length  $d$  and diameter  $a$  [8, p. 467], [2, p. 151]. The charges accelerate along the wire and radiate. In case of an ideal, infinitesimal dipole, the wire is very thin ( $a \ll \lambda$ ) and very small ( $d \ll \lambda$ ) compared to the wavelength  $\lambda$  [2, p. 151], [8, p. 468]. For an antenna to be accurately modeled as an infinitesimal electric dipole, its length usually must be smaller than a fiftieth of the wavelength ( $d < \lambda/50$ ) [2, p. 156]. They are not very practical, but serve as a basic building block for more complex geometries or as a useful excitation method in numerical investigations.

An electric dipole is shown in Figure 2.1 and will now be analyzed. The dipole is aligned with the z-axis, which simplifies the mathematical calculations. Time variation according to  $e^{-j\omega t}$  is assumed and therefore omitted. A current flows in the wire, which is spatially uniform throughout the wire. This is expressed as [2, p. 151]

$$\mathbf{I}(z) = \hat{\mathbf{a}}_z I_0. \quad (2.1)$$

The capacitances modeled at the end of the wire enable the constant current flow, which would otherwise be physically impossible. Next, the vector potential  $\mathbf{A}$  is determined through the general expression

$$\mathbf{A}(\mathbf{x}) = \frac{\mu}{4\pi} \frac{e^{-jkr}}{r} \iiint_V \mathbf{J}(\mathbf{x}') dv'. \quad (2.2)$$

The vector  $\mathbf{x} = \hat{\mathbf{a}}_x x + \hat{\mathbf{a}}_y y + \hat{\mathbf{a}}_z z$  represents the observation point coordinates, while  $\mathbf{x}' = \hat{\mathbf{a}}_x x' + \hat{\mathbf{a}}_y y' + \hat{\mathbf{a}}_z z'$  represents the source point coordinates. The vectors  $\hat{\mathbf{a}}_x$ ,  $\hat{\mathbf{a}}_y$ , and  $\hat{\mathbf{a}}_z$  are unit vectors along the x-, y-, and z-directions, respectively.  $\mathbf{J}$  is the current density in the source region. The variable  $r$  is the distance from any source point to the observation point  $|\mathbf{x} - \mathbf{x}'|$ . In this case, the source point  $\mathbf{x}' = \mathbf{0}$ , due to the infinitesimal dipole [2, p. 152]. The permeability is described by  $\mu$  and the propagation of the wave by  $e^{jkr}$ , where  $k = 2\pi/\lambda$  is the propagation factor, or often called wavenumber.

The integration is performed over the volume  $V$  of the antenna. This leads to [2, p. 153]

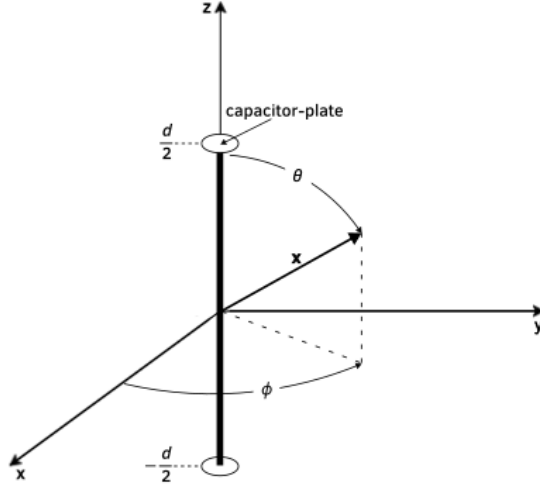


**Figure 2.1** Geometrical arrangement of an infinitesimal electric dipole. It contains a capacitor-plate at each end of the wire to provide a constant current  $\mathbf{I}(z)$ .

$$\mathbf{A}(\mathbf{x}) = \hat{\mathbf{a}}_z \frac{\mu I_0}{4\pi r} e^{-jkr} \int_{-d/2}^{+d/2} dz' = \hat{\mathbf{a}}_z \frac{\mu I_0 d}{4\pi r} e^{-jkr}. \quad (2.3)$$

Any other field quantities can be derived out of the vector potential  $\mathbf{A}$ , such as the electric field intensity  $\mathbf{E}$  and magnetic field intensity  $\mathbf{H}$ . To simplify this process, the Cartesian components of  $\mathbf{A}$  are first transformed into spherical ones. This transform is given in matrix form as [2, p. 153]

$$\begin{bmatrix} A_r \\ A_\theta \\ A_\phi \end{bmatrix} = \begin{bmatrix} \sin \theta \cos \phi & \sin \theta \sin \phi & \cos \theta \\ \cos \theta \cos \phi & \cos \theta \sin \phi & -\sin \theta \\ -\sin \phi & \cos \phi & 0 \end{bmatrix} \begin{bmatrix} A_x \\ A_y \\ A_z \end{bmatrix}, \quad (2.4)$$

where  $\theta$  is the polar angle and  $\phi$  is the azimuthal angle of the observation point  $\mathbf{x}$ .  $\mathbf{E}$  and  $\mathbf{H}$  are then expressed by [2, p. 153],

$$\mathbf{H} = \frac{1}{\mu r} \left[ \frac{\partial}{\partial r} (r A_\theta) - \frac{\partial A_r}{\partial \theta} \right] \hat{\mathbf{a}}_\phi, \quad (2.5a)$$

$$\mathbf{E} = -j\omega \mathbf{A} - j \frac{1}{\omega \mu \epsilon} \nabla (\nabla \cdot \mathbf{A}). \quad (2.5b)$$

Substituting  $\mathbf{A}$  into Equations (2.5a) and (2.5b) reduces them to

$$E_r = \eta \frac{I_0 d \cos \theta}{2\pi r^2} \left[ 1 + \frac{1}{jkr} \right] e^{-jkr}, \quad (2.6a)$$

$$E_\theta = j\eta \frac{kI_0 d \sin \theta}{4\pi r} \left[ 1 + \frac{1}{jkr} - \frac{1}{(kr)^2} \right] e^{-jkr}, \quad (2.6b)$$

$$E_\phi = 0. \quad (2.6c)$$

and,

$$H_r = H_\theta = 0, \quad (2.7a)$$

$$H_\phi = j \frac{kI_0 d \sin \theta}{4\pi r} \left[ 1 + \frac{1}{jkr} \right] e^{-jkr}, \quad (2.7b)$$

$\eta = \sqrt{\frac{\mu}{\epsilon}}$  is the wave impedance of the medium in which the waves travel.

The total radiated power of the dipole is obtained by integrating the complex Poynting vector  $\mathbf{W}$  over a closed surface surrounding the dipole [2, p. 154]. The real part of the total radiated power provides information about energy transferred by radiation, while the imaginary part about the antenna's reactive behavior.  $\mathbf{W}$  is defined by

$$\mathbf{W} = \frac{1}{2} (\mathbf{E} \times \mathbf{H}^*). \quad (2.8)$$

The real power transfer is derived through the time-averaged Poynting vector  $\mathbf{W}_{av}$  [2, p. 160], which is calculated by

$$\mathbf{W}_{av} = \frac{1}{2} \Re\{\mathbf{E} \times \mathbf{H}^*\}. \quad (2.9)$$

The complex power  $P$  is derived by integrating  $\mathbf{W}$  over a closed surface around the dipole, which leads to [2, p. 154]

$$P_r = \eta \frac{\pi |I_0 l|^2}{3 \lambda} \left[ 1 - j \frac{1}{(kr)^3} \right]. \quad (2.10)$$

Equation 2.10 demonstrates, that the imaginary part of the power radiated by the infinitesimal electric dipole shows capacitive behavior.

### 2.1.2 Small Electric Dipoles

Wires that are too long to be modeled as an infinitesimal dipole, but short enough to be considered electrically small ( $\lambda/50 < l \leq \lambda/10$ ), are classified as small physical dipoles [2, pp. 162-163]. They are a more accurate and useful representation of a linear wire antenna, and now investigated further.

A current  $I_0$  is fed into the short, center-fed, linear antenna shown in Figure 2.1. The current along the antenna arms  $I(z)$  linearly drops to zero [12, p. 412], as visualized in Figure 2.3. Mathematically, it is described by,

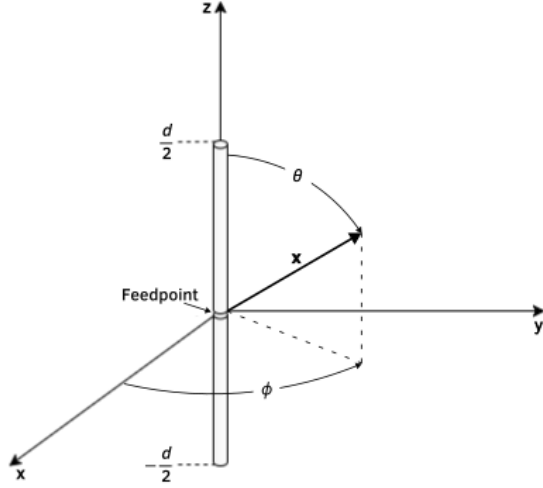


**Figure 2.2** Geometrical arrangement of a linear, center-fed wire antenna with a feed-point indicated in the center. The feedpoint consists of a small gap providing current  $I_0$  to the antenna.

$$\mathbf{I}(z) = \hat{\mathbf{a}}_z I_0 \left( 1 - \frac{2|z|}{d} \right). \quad (2.11)$$

This is different to the current distribution of the infinitesimal dipole. The capacitor-plates are therefore not needed in this model. Furthermore, charge accumulates along the antenna due to the linear drop of current  $\mathbf{I}$ . It is expressed as a charge per unit length  $\rho'$ , which is appropriate due to the thin wire. It is derived by the continuity equation  $j\omega\rho = \nabla \cdot \mathbf{J}$ , which leads to [12, pp. 410-412]

$$\rho' = \pm \frac{d}{dz} j \frac{I(z)}{\omega} = \pm j \frac{2I_0}{\omega d}. \quad (2.12)$$

$\rho'$  is uniformly distributed along each antenna arm.

An important metric is the electric dipole moment  $\mathbf{p}$ . It is defined as the product of charge density  $\rho$  along the antenna and their source point  $\mathbf{x}'$  [12, p.410], and generally expressed as

$$\mathbf{p} = \iiint_V \mathbf{x}' \rho(\mathbf{x}') dv'. \quad (2.13)$$

The charge distribution  $\rho'$  enables the calculation of the electric dipole moment  $\mathbf{p}$ , which results in

$$\mathbf{p} = \int_{-\frac{d}{2}}^{\frac{d}{2}} z \rho'(z) dz \cdot \hat{\mathbf{a}}_z = j \frac{I_0 d}{2\omega} \cdot \hat{\mathbf{a}}_z. \quad (2.14)$$



**Figure 2.3** Current distribution across linear wire antenna. It has a maximum at the feedpoint, and drops to zero at points  $d/2$  and  $-d/2$ .

The electric dipole moment  $\mathbf{p}$  is parallel to the antenna's arms and points in the  $z$ -direction [12, p. 412], [8, p. 155]. Next, the vector potential  $\mathbf{A}$  is determined using Equation 2.2. The calculations of  $\mathbf{A}$  simplify to [12, p. 410],

$$\mathbf{A}(\mathbf{x}) = -j \frac{\mu\omega}{4\pi} \mathbf{p} \frac{e^{-jkr}}{r} \quad (2.15)$$

The formulation of  $\mathbf{A}$  now contains an additional factor of  $1/2$ , compared to the previously derived  $\mathbf{A}$  of the infinitesimal dipoles in Equation 2.3. This is due to the integration process of  $\mathbf{I}$ . When integrated over the same interval  $[-d/2, d/2]$ , the linearly dropping  $\mathbf{I}$  yields half the value of a constant  $\mathbf{I}$ . Furthermore, it makes sense to keep  $\mathbf{x}' = \mathbf{0}$  for simplicity reasons. It has been shown, that this approximation is sufficient for large  $r$ , and the amplitude error remains negligible for small  $r$  [12, p. 409], [2, pp. 164-168].

The short physical electric dipole described in this section approximate the behavior of electrically short antennas. Special care must be taken of the excitation method and shape, as it influences the behavior [12, p. 413]. Additionally, any antenna investigated through this method must remain as small as possible compared to the wavelength  $\lambda$ , to reduce any analytical approximation errors.

Image theory may be added for TEM cell explanations [Balanis]

This makes it reasonable to model electrically small antennas with infinitesimal dipoles

## 2.2 Magnetic Dipoles

The magnetic dipole moment characterizes the strength of a magnetic source. A small current loop fed with a current  $I_0$  can be used to model the magnetic dipole, as demonstrated in Figure 2.4. This relation holds as long as its overall length is smaller than a tenth of the wavelength ( $2b\pi < \lambda/10$ ) and as long as the the wire is very thin [2, p. 231]. Furthermore, the radiation pattern of the magnetic dipole is equal to that of the electric dipole, with the role of the electric and magnetic fields interchanged [8, p. 254].

The magnetic dipole moment  $\mathbf{m}$  is given by [12, p. 413]



**Figure 2.4** Geometrical arrangement of a current loop fed by a current  $I_0$ , producing a magnetic dipole moment. Alternatively, a magnetic current  $I_m$  flows perpendicular to the loop's area along the distance  $L$ , which produces an equivalent magnetic dipole moment.

$$\mathbf{m} = \frac{1}{2} \iiint_V (\mathbf{x}' \times \mathbf{J}) dv'. \quad (2.16)$$

Furthermore, the magnetic current  $I_m$  and the electric current  $I_0$  in the loop are related with [2, p. 237]

$$I_m L = j A \omega \mu_0 I_0 \quad (2.17)$$

with  $A = b^2 \pi$  being the area of the current loop. Analogous to the separation distance  $d$  in the electric dipole,  $L$  is the length of the magnetic dipole.  $I_m$  and  $L$  may be used to model the magnetic dipole moment instead of the current loop. The fields  $\mathbf{E}$  and  $\mathbf{H}$  generated are the same in both cases. This means, that the infinitesimal magnetic dipole can be replaced with an electrically small loop [2, p. 237]. This was not the case for the infinitesimal and electrically small electric dipoles.  $\mathbf{E}$  and  $\mathbf{H}$  of the magnetic dipole moment or electrically small current loop are then determined with [2, p. 237]

$$E_r = E_\theta = 0, \quad (2.18a)$$

$$E_\phi = -j \frac{k I_m d \sin \theta}{4\pi r} \left[ 1 + \frac{1}{jkr} \right] e^{-jkr}, \quad (2.18b)$$

and,

$$H_r = \frac{I_m d \cos \theta}{2\pi r^2 \eta} \left[ 1 + \frac{1}{jkr} \right] e^{-jkr}, \quad (2.19a)$$

$$H_\theta = j \frac{k I_m d \sin \theta}{4\pi r \eta} \left[ 1 + \underbrace{\frac{1}{jkr}}_{\text{Expression 1}} - \underbrace{\frac{1}{(kr)^2}}_{\text{Expression 2}} \right] e^{-jkr}, \quad (2.19b)$$

$$H_\phi = 0. \quad (2.19c)$$

The complex power density  $\mathbf{W}$  can be derived analogous to the electric dipole case in Equation 2.8. For the magnetic dipole, the imaginary part of  $\mathbf{W}$  has the opposite sign compared to the electric dipole. This is the result of the near-field power being inductive in case of the magnetic dipole, while it is capacitive for the electric dipole. The complex power equals to

$$P_r = \eta \left( \frac{\pi}{12} \right) (ka)^4 |I_0|^2 \left[ 1 + j \frac{1}{(kr)^3} \right], \quad (2.20)$$

and its imaginary part is inductive [2, p. 238].

### 2.3 Crossed Dipoles

Section todo

Crossed dipoles can generate a wide variety of radiation patterns. Supposed two dipoles are placed perpendicular to each other and fed 90° out of phase, an omnidirectional radiation pattern is created [25]. If the equivalent dipoles of an EUT represents such two dipoles, any mode which can propagate in the TEM cell will do so, and therefore influence the measurement result. It is therefore not only important to know which dipoles there are representing the EUT, but also what phase and magnitude they have. Meaning that not only the dipoles aligned with the TEM mode alone influence the result.

Dipoles next to conducting planes (balanis, collin)

### 2.4 Radiated Field

### 2.5 Field regions

The field quantities  $\mathbf{E}$  and  $\mathbf{H}$  have been derived for an infinitesimal electric dipole in Equations (2.6a) to (2.6c) and Equations (2.7a) and (2.7b), and for an infinitesimal magnetic dipole in Equations (2.19a) to (2.19c) and Equations (2.18a) and (2.18b). They are valid everywhere except for the source region [2, p. 156].

Depending on the distance  $r$  to the dipole, the behavior of the fields changes. This becomes apparent when investigating the expressions  $1/(jkr)$  and  $1/(kr)^2$  in Equations (2.6a) to (2.6c) and Equations (2.7a) and (2.7b) of the infinitesimal electric dipole. These expressions are highlighted here in the case of  $E_\theta$ , although they partly also appear in  $E_r$  and  $H_\phi$ , and referred to as Expression 1 and Expression 2 in

$$E_\theta = j \eta \frac{k I_0 d \sin \theta}{4\pi r} \left[ 1 + \underbrace{\frac{1}{jkr}}_{\text{Expression 1}} - \underbrace{\frac{1}{(kr)^2}}_{\text{Expression 2}} \right] e^{-jkr}. \quad (2.21)$$

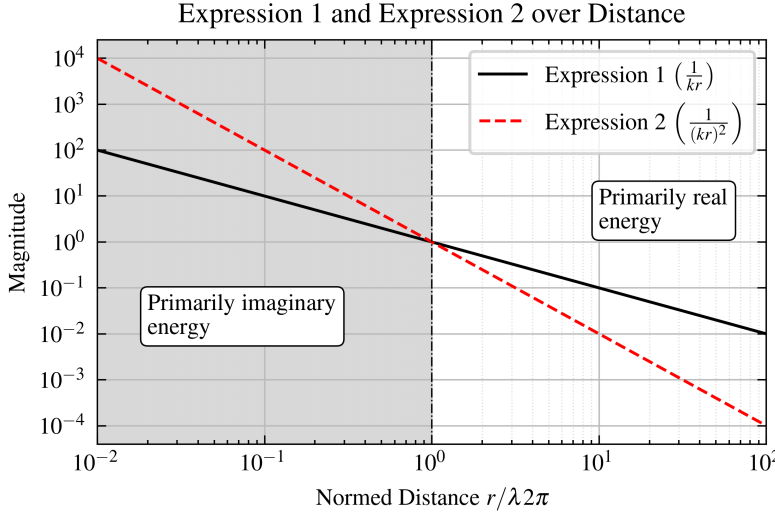


**Figure 2.5** Behavior of Expression 1 and Expression 2 in Equation 2.21 over distance  $r$ . The distance  $r$  is normalized to the radian distance  $\lambda/2\pi$ . The magnitude of both expressions is normed to 1 at radian distance for better comparison.

If the distance  $r < \lambda/2\pi$  ( $kr < 1$ ), then Expression 2 delivers the largest value in the brackets. Consequently, the energy stored in this region is mostly imaginary, especially if  $r \ll \lambda/\pi$  ( $kr \ll 1$ ). It is referred to as the near-field region.

At distances  $r > \lambda/2\pi$  ( $kr > 1$ ), Expression 1 exceeds Expression 2 in value. The real part of the energy is larger than the imaginary part. This region is referred to as the intermediate-field region. For  $r \gg \lambda/2\pi$  ( $kr \gg 1$ ) the energy is primarily real, indicating radiation. This region is called the far-field region.

At  $r = \lambda/2\pi$  ( $kr = 1$ ), Expression 1 and Expression 2 are of equal magnitude. This is marked as the radian distance [2, pp. 156-160]. The radian distance therefore represents an important transition point between field regions, where the behavior of the fields shifts. Figure 2.5 visualizes Expression 1 and Expression 2 over  $r$ . The same analysis of the field region is also valid for the infinitesimal magnetic dipole.

Antennas, which cannot be modeled as infinitesimal dipoles, such as the linear wire antenna, are surrounded by different field regions. They are shown in Figure 2.6. The far-field region contains mostly real energy, and the antenna may be most accurately approximated by an infinitesimal electric dipole. In the radiating near-field, the energy is largely real, but depends on the distance  $r$ . Lastly, in the reactive near-field the energy is mostly imaginary.

The far-field region starts at approximately  $r_2$  and the radiating near-field at  $r_1$ , which are defined as

$$r_1 = 0.62\sqrt{d^3/\lambda}, \quad (2.22a)$$

$$r_2 = 2d^2/\lambda. \quad (2.22b)$$

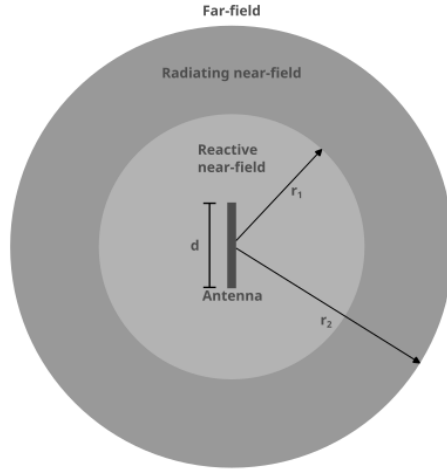


**Figure 2.6** Field regions of an antenna, here specifically a linear wire antenna. However, they are applicable for any antenna, as long as their largest dimension  $d$  is known.

Here,  $d$  is the largest dimension of the antenna. In the case of the linear wire antenna,  $d$  is the wire length [2, pp. 165-170].

### 3 Guided Waves

#### 3.1 Lorentz Reciprocity Theorem

The Lorentz reciprocity theorem proves to be very useful for further analysis. Let two source pairs  $\mathbf{J}_1, \mathbf{M}_1$  and  $\mathbf{J}_2, \mathbf{M}_2$  exist in a volume  $V$ , bounded by the closed surface  $S$ . The medium in  $V$  is linear and isotropic. The source pairs generate fields  $\mathbf{E}_1, \mathbf{H}_1$  and  $\mathbf{E}_2, \mathbf{H}_2$ , respectively, with the same frequency. The fields and source pairs can then be related with [2, p. 145], [6, p. 49]

$$-\nabla \cdot (\mathbf{E}_1 \times \mathbf{H}_2 - \mathbf{E}_2 \times \mathbf{H}_1) = \mathbf{E}_1 \cdot \mathbf{J}_2 + \mathbf{H}_2 \cdot \mathbf{M}_1 - \mathbf{E}_2 \cdot \mathbf{J}_1 - \mathbf{H}_1 \cdot \mathbf{M}_2. \quad (3.1)$$

Integrating Equation 3.1 over  $V$ , and converting the volume integral to a surface integral with the divergence theorem, leads to [2, p. 145], [6, p. 50]

$$\begin{aligned} & - \oint\int_S (\mathbf{E}_1 \times \mathbf{H}_2 - \mathbf{E}_2 \times \mathbf{H}_1) \cdot d\mathbf{s}' \\ &= \iiint_V (\mathbf{E}_1 \cdot \mathbf{J}_2 + \mathbf{H}_2 \cdot \mathbf{M}_1 - \mathbf{E}_2 \cdot \mathbf{J}_1 - \mathbf{H}_1 \cdot \mathbf{M}_2) \cdot d\mathbf{v}'. \end{aligned} \quad (3.2)$$

This is a very useful integral equation, which relates the coupling of different source points. If one of these sources is set to zero, they can serve as observation points. This can be done to investigate, for example, modes and their coupling in a waveguide. Suppose the volume  $V$  does not contain sources  $\mathbf{J}_1 = \mathbf{M}_1 = \mathbf{J}_2 = \mathbf{M}_2 = \mathbf{0}$ . Then, the Lorentz Reciprocity theorem in differential and integral form would be [2, pp. 145-146]

$$\nabla \cdot (\mathbf{E}_1 \times \mathbf{H}_2 - \mathbf{E}_2 \times \mathbf{H}_1), \quad (3.3a)$$

$$\oint_S (\mathbf{E}_1 \times \mathbf{H}_2 - \mathbf{E}_2 \times \mathbf{H}_1) \cdot d\mathbf{s}' = 0, \quad (3.3b)$$

which the modes in the waveguide must fulfill.

Another application arises when investigating a volume  $V$  confined by a perfectly conducting surface  $S$ , in which the linear current densities  $\mathbf{J}_1$  and  $\mathbf{J}_2$  flow. Because  $\mathbf{n} \times \mathbf{E}_1 = \mathbf{n} \times \mathbf{E}_2 = 0$  along the surface  $S$ , the surface integral in Equation 3.2 vanishes, and

$$\mathbf{E}_1 \cdot \mathbf{J}_2 = \mathbf{E}_2 \cdot \mathbf{J}_1, \quad (3.4)$$

arise. This is the Rayleigh-Carson form of the Lorentz reciprocity theorem. It states that  $\mathbf{J}_1$  generates  $\mathbf{E}_1$ , which has components along  $\mathbf{J}_2$ , that are equal to the same components of  $\mathbf{E}_2$  along  $\mathbf{J}_1$ , and vice versa [6, p. 50].

Concluding, the Lorentz Reciprocity theorem is useful to derive reciprocal aspects of waveguides, finding orthogonal properties of modes, investigating fields generated by currents and dipole moments in waveguides [6, p. 50], and much more. It will serve in the remainder of this thesis.

There could be a sketch made with such a waveguide and H1, E1, H2, E2

## 3.2 Green's Function

### 3.2.1 Scalar Green's Function

The Green's function describes the response of a linear differential operator  $L$  to a point source of unit strength. It is explained briefly in the following with an example of solving the Poisson's equation with boundary conditions, since this concept will be used in further analysis. The general form for a Green's function of a given problem is

$$LG(\mathbf{x}, \mathbf{x}') = -\delta(\mathbf{x} - \mathbf{x}'). \quad (3.5)$$

A point source of unit strength is generally modeled with a delta function  $\delta$  at a certain point in one-dimensional space. In multi-dimensional space, a product of delta-functions are used.

Once Equation 3.5 is solved for a point source of unit strength, and the Green's function  $G$  of this specific problem is known, it can be used to solve for any combination of point sources  $f$  to solve for an input function  $u$ ,

$$Lu(\mathbf{x}) = f(\mathbf{x}), \quad (3.6)$$

This is done through superposition through point sources of unit strength, as in

$$u(\mathbf{x}) = \iiint_V G(\mathbf{x}, \mathbf{x}') f(\mathbf{x}') dv'. \quad (3.7)$$

The integrands are the source point variables  $x', y', z'$ .

One application of the Green's function is solving the Poisson's equation. The scalar potential  $\phi$  can be calculated from a density of charge distribution  $\rho$  by using the Green's function of this specific problem. If there are no boundaries present, it takes the form

$$\nabla^2 \phi = -\frac{\rho}{\epsilon}, \quad (3.8a)$$

$$\phi(\mathbf{x}) = \frac{1}{4\pi\epsilon} \iiint_V \frac{\rho(\mathbf{x}')}{|\mathbf{x} - \mathbf{x}'|} dv', \quad (3.8b)$$

where  $\epsilon$  is the permittivity of the medium.

The Green's function for this problem equals  $G(\mathbf{x}, \mathbf{x}') = \frac{1}{4\pi|\mathbf{x}-\mathbf{x}'|}$ , and represents the potential at position  $\mathbf{x}$  created by an unit point charge at point  $\mathbf{x}'$ . In this case, the input function  $u = \phi$  and the source function  $f = -\rho/\epsilon_0$ .

Different volumes of interest  $V_1, V_2, \dots, V_n$  can be connected by applying boundary conditions on their surrounding surfaces  $S_1, S_2, \dots, S_n$ . Applying Green's second identity on the Poisson's equation enables enforcing such a boundary condition upon the surrounding surface  $S$  of a volume  $V$ ,

$$\iiint_V (\phi \nabla_{\mathbf{x}'}^2 G - G \nabla_{\mathbf{x}'}^2 \phi) dv' = \oint_S \left( G \frac{\partial \phi}{\partial \mathbf{n}} - \phi \frac{\partial G}{\partial \mathbf{n}} \right) d\mathbf{s}'. \quad (3.9)$$

The vector  $\mathbf{n}$  is normal to  $S$ . The operator  $\nabla_{\mathbf{x}'}^2$  differentiates with respect to the source vector  $\mathbf{x}'$  due to  $x', y', z'$  being the integrands. Inserting  $\nabla^2 \phi = -\rho/\epsilon$  from Equation 3.8a and  $\nabla^2 G = -\delta$  from Equation 3.5 leads to

$$\phi = \frac{1}{\epsilon} \iiint_V \rho(\mathbf{x}') G(\mathbf{x}, \mathbf{x}') \cdot d\mathbf{v}' + \oint_S \left( \phi \frac{\partial G}{\partial \mathbf{n}} - G \frac{\partial \phi}{\partial \mathbf{n}} \right) d\mathbf{s}' \quad (3.10)$$

$\phi$  or its normal derivative to the surface  $\partial\phi/\partial\mathbf{n}$  can be forced on the boundary. If only one of those two expressions is known on the boundary surface, the Green's function may be modified such that the unknown expression vanishes. If  $\phi$  is defined on the whole boundary, it satisfies Dirichlet boundary conditions. On the other hand, if  $\partial\phi/\partial\mathbf{n}$  is defined on the whole boundary, it satisfies Neumann boundary conditions [6, pp. 55-59].

This will become useful for the greens function in tem cell: Perturbed and un-perturbed term connecting the upper and lower chamber

### 3.2.2 Dyadic Green's Function

While the scalar Green's function is useful for solving one-dimensional differential equations, the dyadic Green's function  $\bar{\mathbf{G}}$  is more suitable for three-dimensional problems. It relates a vector source with a vector response, which is necessary when solving the vector Helmholtz equation in

$$\nabla^2 \mathbf{A} + k^2 \mathbf{A} = -\mu \mathbf{J}. \quad (3.11)$$

When replacing  $\mu\mathbf{J}$  by an unit vector source  $(\hat{\mathbf{a}}_x + \hat{\mathbf{a}}_y + \hat{\mathbf{a}}_z)\delta(\mathbf{x} - \mathbf{x}')$ , the solution for  $\mathbf{A}$  of Equation 3.11 in free-space is

$$(\hat{\mathbf{a}}_x + \hat{\mathbf{a}}_y + \hat{\mathbf{a}}_z) \frac{e^{-jk|\mathbf{x}-\mathbf{x}'|}}{4\pi|\mathbf{x}-\mathbf{x}'|}. \quad (3.12)$$

This is a vector Green's Function by definition [6, pp. 91-92].

Each component of the current distribution  $\mathbf{J}$  generates fields through a linear relation. This relationship can effectively be represented by dyadics, which are linear mappings between vectors. The dyadic Green's function is therefore introduced and defined as

$$\begin{aligned} \bar{\mathbf{G}} = & G_{xx} \hat{\mathbf{a}}_x \hat{\mathbf{a}}_x + G_{xy} \hat{\mathbf{a}}_x \hat{\mathbf{a}}_y + G_{xz} \hat{\mathbf{a}}_x \hat{\mathbf{a}}_z + \\ & G_{yx} \hat{\mathbf{a}}_y \hat{\mathbf{a}}_x + G_{yy} \hat{\mathbf{a}}_y \hat{\mathbf{a}}_y + G_{yz} \hat{\mathbf{a}}_y \hat{\mathbf{a}}_z + \\ & G_{zx} \hat{\mathbf{a}}_z \hat{\mathbf{a}}_x + G_{zy} \hat{\mathbf{a}}_z \hat{\mathbf{a}}_y + G_{zz} \hat{\mathbf{a}}_z \hat{\mathbf{a}}_z \end{aligned}$$

Each component of the current vector  $\mathbf{J}$  is associated with one unit vector of the Green's function, i.e.  $J_x$  with  $\hat{\mathbf{a}}_x$ ,  $J_y$  with  $\hat{\mathbf{a}}_y$  and  $J_z$  with  $\hat{\mathbf{a}}_z$  [6, p. 92]. Consequently, the field generated by a current component in a given direction is determined by the corresponding column of the dyadic Green's function. For example, if only a current component  $J_x$  is present, the field components  $A_x$ ,  $A_y$ , and  $A_z$  are obtained from the Green's functions elements  $G_{xx}$ ,  $G_{yx}$  and  $G_{zx}$ .

The dyadic Green's function is defined as the solution of

$$\nabla^2 \bar{\mathbf{G}}(\mathbf{x}, \mathbf{x}') + k^2 \bar{\mathbf{G}} = -\bar{\mathbf{I}}\delta(\mathbf{x} - \mathbf{x}'). \quad (3.13)$$

In free space, a commonly used form of the dyadic Green's function is given by [6, p.92]

$$\bar{\mathbf{G}}(\mathbf{x}, \mathbf{x}') = \bar{\mathbf{I}} \frac{e^{-jk|\mathbf{x}-\mathbf{x}'|}}{4\pi|\mathbf{x}-\mathbf{x}'|}, \quad (3.14)$$

where  $\bar{\mathbf{I}}$  is an unit dyadic. The free-space case is presented here to provide an overview. Dyadic Green's functions can also be derived for bounded geometries, such as waveguides, by implementing appropriate boundary conditions.

The fields  $\mathbf{A}$  generated by arbitrary  $\mathbf{J}$  can be expressed with the dyadic Green's function as

$$\mathbf{A}(\mathbf{x}) = \mu \iiint_V \bar{\mathbf{G}}(\mathbf{x}, \mathbf{x}') \mathbf{J}(\mathbf{x}') d\mathbf{v}'. \quad (3.15)$$

Each component of  $\mathbf{J}$  drives a combination of components in  $\mathbf{A}$ . Dyadics capture this component-wise coupling and simplify the notation [6, p. 92].

*The dyadic Green's Function is commonly applied to calculate field distributions in waveguides. In [28] it is used to derive the fields in a TEM cell caused by a vertical current conducting wire with help of the small-gap approximation.*

Chapter  
is called  
"Guided  
Waves",  
but this  
chapter  
presents  
free-space  
solutions

### 3.3 Modes in a TEM Cell

#### 3.3.1 Rectangular Waveguides as non-TEM structures

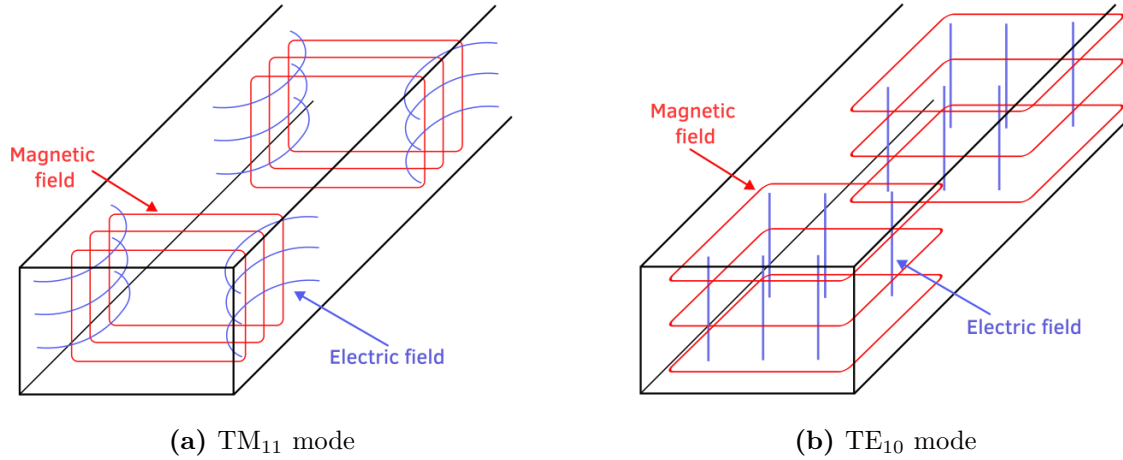


**Figure 3.1** Dominant modes in a rectangular waveguide.

A simple rectangular waveguide cannot support TEM modes. For a monochromatic wave propagating within the waveguide, undamped propagation occurs only at specific reflection angles on the perfectly conducting walls. A brief analysis using Maxwell's equations shows that the electric and magnetic field components along the direction of propagation cannot both be zero.

$$\mathbf{E} = (E_{0,x} \cdot \mathbf{e}_x + E_{0,y} \cdot \mathbf{e}_y + E_{0,z} \cdot \mathbf{e}_z)e^{i(\omega t - kz)} \quad (3.16)$$

$$\mathbf{H} = (H_{0,x} \cdot \mathbf{e}_x + H_{0,y} \cdot \mathbf{e}_y + H_{0,z} \cdot \mathbf{e}_z)e^{i(\omega t - kz)} \quad (3.17)$$

$$\nabla \times \mathbf{E} = \begin{pmatrix} \frac{d}{dy} E_z - ik E_y \\ ik E_x - \frac{d}{dx} E_z \\ \frac{d}{dx} E_y - \frac{d}{dy} E_x \end{pmatrix} = \begin{pmatrix} -i\omega B_x \\ -i\omega B_y \\ -i\omega B_z \end{pmatrix} \quad (3.18)$$

$$\nabla \times \mathbf{B} = \begin{pmatrix} \frac{d}{dy} B_z - ik B_y \\ ik B_x - \frac{d}{dx} B_z \\ \frac{d}{dx} B_y - \frac{d}{dy} B_x \end{pmatrix} = \begin{pmatrix} \frac{i\omega}{\mu\epsilon} E_x \\ \frac{i\omega}{\mu\epsilon} E_y \\ \frac{i\omega}{\mu\epsilon} E_z \end{pmatrix} \quad (3.19)$$

If  $E_z$  and  $B_z$ , the fields in direction of propagation, were both zero, then the change of the transverse fields would be constantly zero, and because of the boundary conditions, all transverse fields would be zero. Equation 3.20 shows Gauss' law and Equation 3.21 Faraday's law if  $E_z = B_z = 0$ , from which the unchanging transverse electric field can be derived.

$$\frac{d}{dx}E_x + \frac{d}{dy}E_y = 0 \quad \text{Derived out of Gauss' law} \quad (3.20)$$

$$\frac{d}{dy}E_x - \frac{d}{dx}E_y = 0 \quad \text{Derived out of Faraday's law} \quad (3.21)$$

### 3.3.2 TEM mode in the TEM cell

Unfinished section. Described radiation resistance of antenna, not yet TEM mode.

A TEM cell is used for EMC test specifications. It makes the conduction of TEM waves possible, which resemble planar free-space waves. Additionally, it shields the waves from radiating to the sides, for which it has a clear advantage to a stripline [9, 13].

A TEM cell solves this problem, by having a gap between the septum and the side walls. Essentially, it can be considered as two rectangular waveguides with apertures on the sides. Those apertures allow perturbations of the electromagnetic fields between them. The boundary conditions of the Laplace equation now changed due to the gaps. The Green's function may be calculated of the new construction, now considering the boundary conditions at the gaps, which must be the same for both waveguides (to prevent discontinuities). In the papers of Tippet, Chang and Wilson, this new Green's function lead to the excitation of TEM modes in both waveguides [26, 28]. However, the gap is assumed to be small, electrically ( $\xi g \ll 1$ ) and compared to the septum width ( $g/a \ll 1$ ) [29]. The variable  $\xi = \sqrt{k_0^2 - \beta^2}$  is the transverse (in y-direction) propagation constant, and consists of the free-space wave number  $k_0$  and longitudinal (in z-direction) propagation constant  $\beta$ . The variables  $g$  and  $a$  are geometry variables of the TEM cell annotated in Figure 3.2.

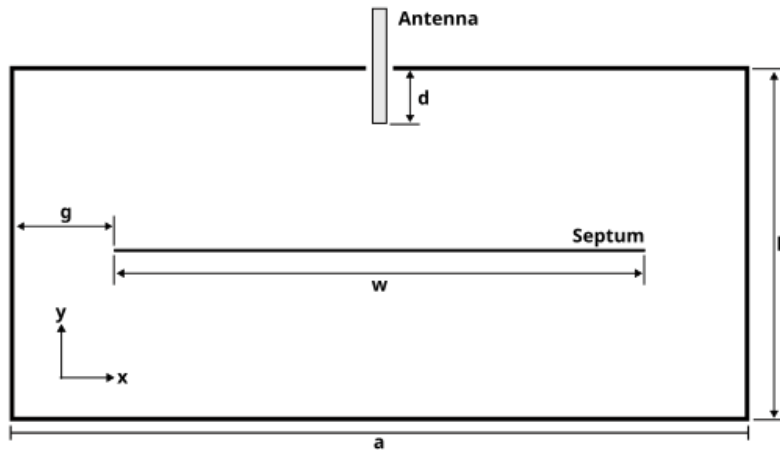


**Figure 3.2** TEM cell with vertical antenna inserted

To analyze the fields in a TEM cell, the dyadic Green's function discussed in subsubsection 3.2.2 proves itself to be useful. It is assumed, that a vertical, electrically short antenna is inserted in the top center of the TEM cell. This is modeled by a current distribution in y-direction  $\hat{\mathbf{J}}(\mathbf{x}) = \mathbf{a}_y J(\mathbf{x})$  [29]. Accordingly, the Green's function reduces to

$\hat{\mathbf{G}}(\mathbf{x}, \mathbf{x}') = \mathbf{a}_y G(\mathbf{x}, \mathbf{x}')$ . First, the Green's function for a rectangular waveguide  $G_O(\mathbf{x}, \mathbf{x}')$  is shown in Equation 3.22 [2]. There,  $\eta_0$  is the free-space impedance,  $M = m\pi/(2a)$ ,  $N = n\pi/b$  and  $K_m = (\xi^2 - M^2)^{1/2}$ . Furthermore,

$$\Delta_n = \begin{cases} \frac{1}{2}, & n = 0 \\ 1, & n > 0 \end{cases}$$

Check  
Vector notation. Is  
correct for  
Dyadics?

and,

$$g_{mn}(\mathbf{x}_t, \mathbf{x}'_t) = \left(\frac{2}{ab}\right) \sin M(x+a) \sin M(x'+a) \cdot \cos Ny \cos Ny'$$

are functions implemented in Equation 3.22. The components  $x, x'$  and  $y, y'$  are part of the vectors  $\mathbf{x}_t, \mathbf{x}'_t$ .

$$\tilde{G}_0(\mathbf{x}_t, \mathbf{x}'_t) = \frac{-j\eta_0}{k_0} \left\{ \sum_{m,n=0}^{\infty} \frac{\Delta_n[M^2 + \beta^2]}{M^2 + N^2 - \xi^2} g_{mn}(\mathbf{x}_t, \mathbf{x}'_t) \right\} \quad (3.22)$$

The TEM cells Green's function by adding a unperturbed term to it [29]. The derivation of those Green's Functions is demonstrated in [28], which uses the same methods described in [2], as mentioned above.

The perturbed term in Equation 3.23 describes the influence of the gaps on the field distribution. They are derived by forcing the tangential fields to be continuous across the gaps, then describing this boundary condition mathematically as a perturbing second Green's function. The rest of the boundary conditions on the are zero due to the geometry of the TEM cell. The functions used are,

$$L(\beta) = \left[ \ln \left( \frac{8a}{\pi g} \right) - \frac{\pi}{a} \sum_{m \in \{1,3,5,\dots\}}^{\infty} \left( \frac{\cot K_m b}{K_m} + \frac{2a}{m\pi} \right) \right]^{-1}$$

and,

$$f(\mathbf{x}_t) = \sum_{m \in \{1,3,5,\dots\}}^{\infty} M \frac{\cos K_m(b-y)}{K_m \sin K_m b} \sin Ma \cos Mx J_0(Mg).$$

To receive the final Green's Function, the unperturbed and perturbed term are added together  $G(\mathbf{x}_t, \mathbf{x}'_t) = G_O(\mathbf{x}_t, \mathbf{x}'_t) + G_g(\mathbf{x}_t, \mathbf{x}'_t)$ . Naturally, the observation point  $\mathbf{x}$  can only be on the upper half in the chamber, where the source is also located [29].

$$\tilde{G}_g(\mathbf{x}_t, \mathbf{x}'_t) = \frac{-j\pi k_0 \eta_0}{2a^2 s^2} L(\beta) f(\mathbf{x}_t) f(\mathbf{x}'_t) \quad (3.23)$$

Because waves propagating in the TEM cell are assumed to travel into infinity, they might have any longitudinal propagation constant  $\beta$ . They are not limited by boundary conditions in this direction. It therefore proofs useful to apply a Fourier Series over this

variable, as done in Equation 3.24. There, the subscript  $t$  indicates only the transverse (xy-plane).

$$G_O(\mathbf{x}, \mathbf{x}') = \frac{1}{2\pi} \int_{-\infty}^{\infty} \tilde{G}_0(\mathbf{x}_t, \mathbf{x}'_t) e^{j\beta z} d\beta \quad (3.24a)$$

$$G_g(\mathbf{x}, \mathbf{x}') = \frac{1}{2\pi} \int_{-\infty}^{\infty} \tilde{G}_g(\mathbf{x}_t, \mathbf{x}'_t) e^{j\beta z} d\beta \quad (3.24b)$$

This explanation is not directly cited but my interpretation. Make sure that this is correct info.

Now, the antenna impedance is calculated using the generic Equation 3.25. The Green's Function in this represents the electric field excited by an unit strength dipole [29]. Scaled by multiplication with the current density  $\mathbf{J}(\mathbf{x})$  and integrated over the length of the wire, results in the total electric field. Next, by multiplying it by the current distribution  $\mathbf{J}(\mathbf{x})$  and integrated over the length of the wire again, leads to the apparent power. In the end, dividing this term by the total current consumption squared  $I^2$  leads to the impedance.

$$Z = \frac{-1}{I^2} \int_S \int_{S'} \mathbf{J}(\mathbf{x}) \cdot \mathbf{G}(\mathbf{x}, \mathbf{x}') \cdot \mathbf{J}(\mathbf{x}') ds' ds \quad (3.25)$$

When evaluating the real part of the impedance for the case described here, the radiation resistance results from Equation 3.26. If the inserted antenna is electrically small, as it is in this case,  $d$  reduces the influence of other terms. The most dominant term then,  $k_0^2$ , results in a quadratic relation of the radiation resistance to the frequency. This agrees with the theoretical framework in the discussion about small dipoles in ??, as well as with the simulations results in section 4.

$$R = \frac{\pi \eta_0 k_0^2}{4a^2} \csc^2 k_0 d L(k_0) H(k_0) \quad (3.26)$$

Here,

$$H(\beta) = \sum_{m' \in \{1, 3, 5, \dots\}}^{\infty} h_{m'}(\beta) \sum_{m \in \{1, 3, 5, \dots\}}^{\infty} h_m(\beta) J_0(r(M^2 + \beta^2)^{1/2})$$

and,

$$h_m(\beta) = \frac{M \sin Ma J_0(Mg)}{K_m \sin K_m b} \cdot \frac{\cos k_0 d - \cos K_m d}{M^2 + \beta^2}.$$

propagates.

### 3.3.3 Higher-order modes

The TEM cell used in the simulation has a width of  $a = 40$  mm and a height of  $b = 24$  mm. A cross section of the TEM cell with the important dimensions is shown in Figure 3.3. The cutoff frequencies of the higher order TE and TM modes can be approximated by the same formula, shown in Equation 3.27 for rectangular waveguides. However, this is only

Insert Green's Functions calculations, which show that TEM mode

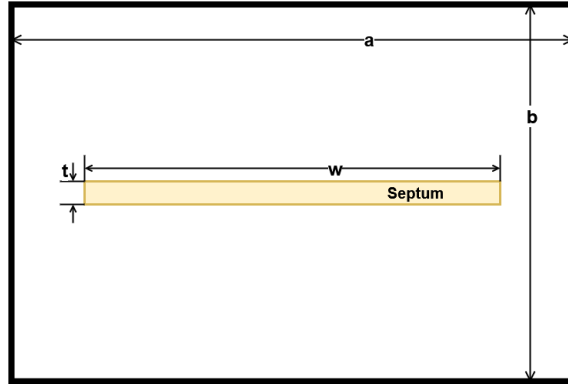


**Figure 3.3** Cross section of the TEM cell

true, if the septum is very thin ( $t/b \ll 0.1$ ), and for modes with n-even subscripts, i.e.  $\text{TE}_{m,2n}$  and  $\text{TM}_{m,2n}$  modes.

$$f_c = \frac{c}{2} \sqrt{\left(\frac{m}{a}\right)^2 + \left(\frac{n}{b}\right)^2} \quad (3.27)$$

- $f_c$ : cutoff frequency of the mode  $\text{T}_{mn}$
- $c$ : speed of light in the medium (approximately  $3 \times 10^8$  m/s in air)
- $a$ : wider dimension (broad wall) of the rectangular waveguide (meters)
- $b$ : narrower dimension (narrow wall) of the rectangular waveguide (meters)
- $m$ : mode index in the  $a$ -direction (integer,  $m \geq 0$ )
- $n$ : mode index in the  $b$ -direction (integer,  $n \geq 0$ )

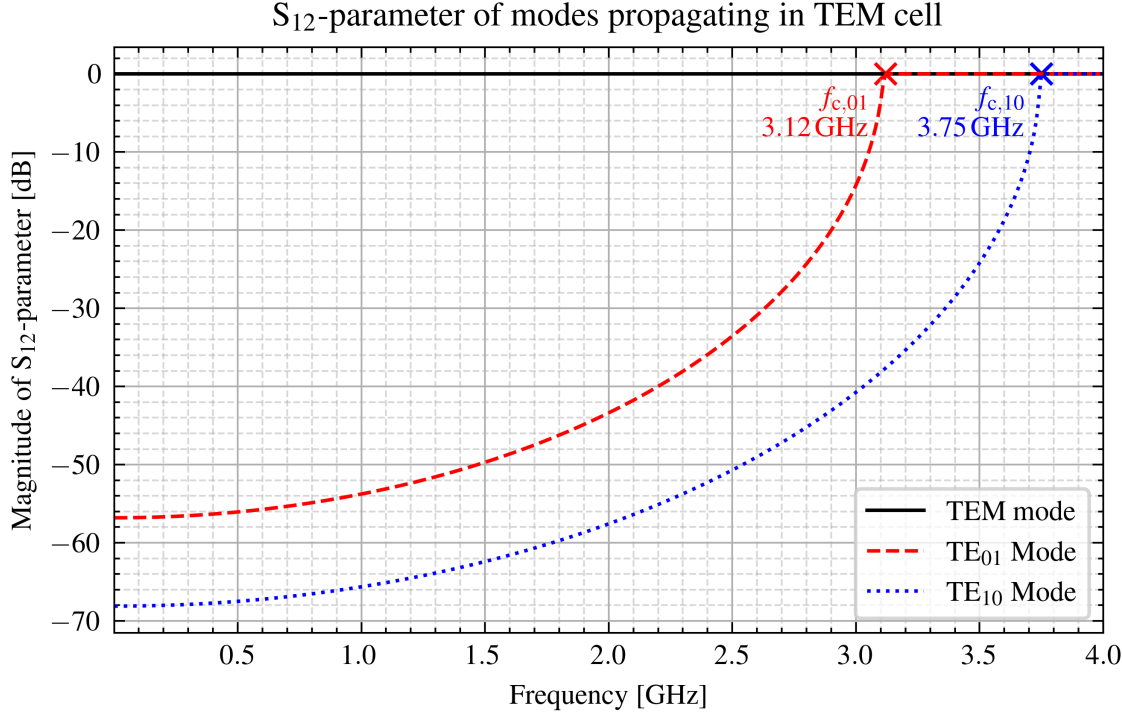
The cutoff frequency of the  $\text{TE}_{10}$  mode is around 3.75 GHz, according to Equation 3.27. To verify this, a modal analysis was performed in Ansys HFSS, where an empty TEM cell was modeled with two waveports defined at its output. The resulting  $S_{12}$ -parameters are presented in Figure 3.4. The black line shows the  $S_{12}$ -parameter over the frequency of the TEM mode, while the blue line demonstrates  $S_{12}$ -parameter of the  $\text{TE}_{10}$  mode. At a frequency of 3.75 GHz, the mode propagates without attenuation, where the cutoff frequency  $f_{c,10}$  is defined. The simulated result comes very close to the analytically determined one.

The red trace shows a cutoff frequency of  $f_{c,10} = 3.12$  GHz for the  $\text{TE}_{01}$  mode. Equation 3.27 would predict a cutoff frequency of 6.25 GHz, however, the septum influences n-odd modes like this one. Their cutoff frequencies are shifted to a lower value [27].

The frequency in simulations with the TEM cell will range from 1 MHz to 3 GHz. This guarantees that the higher order modes will not influence the simulation results.

In a real TEM cell, a tapered section transform the TEM waveguide to a coaxial transmission line. This section does not cause reflections of waves in TEM mode. However, higher order TE and TM modes get reflected, and because the TEM cell is a high-Q cav-

ity, resonances occur at  $\frac{\lambda}{4}$  or  $\frac{\lambda}{2}$  [13]. This is not considered in these simulations, since the simulation model does not contain this tapered section.



Maybe do simulations with such a tapered section. See [13]

**Figure 3.4** Propagation of TEM, TE<sub>01</sub> and TE<sub>10</sub> modes in TEM cell

plot title:  
|S<sub>12</sub>|

The TEM cell does not only support TEM modes, above their cut-off frequency TE and TM modes begin to propagate. Because the TEM cell is a high-Q cavity, those cut-off frequencies are sharply defined frequencies. Due to imperfections, change in materials or finite conductivity of the conducting plates, wave propagating in the TEM mode may excite higher order TE and TM modes, too [14]. A change in material, for example, demands the electric and magnetic field to have a component in the direction of propagation at the discontinuity. A paper by Wilson and Ma present analytical approximations to determine these frequencies [31]. There is a long list for the several first few corner frequencies of the first modes. Additionally, a paper by Koch, Groh and Garbe determines the resonance frequencies of the first TE modes analytically [14]. The TEM mode is necessarily excited by the geometry of the TEM cell, hence this mode is called essential. The higher order TE and TM modes, which are only excited due to non-uniformity of the TEM cell, are called non-essential modes [13].

The first modes propagating after the TEM mode is the TE<sub>10</sub> and TE<sub>01</sub> modes. Their transversal electric fields are depicted in Figure 3.5.

The cut-off frequencies are dependent on the dimensions of the TEM cell, as previously shown. Table 1 shows some cut-off frequencies of these modes for different TEM cell dimensions. The TE<sub>10</sub>-mode is independent of the height  $b$  of the TEM cell, as would be the case in a rectangular waveguide. Both the TE<sub>10</sub>-mode and the TE<sub>01</sub>-mode are

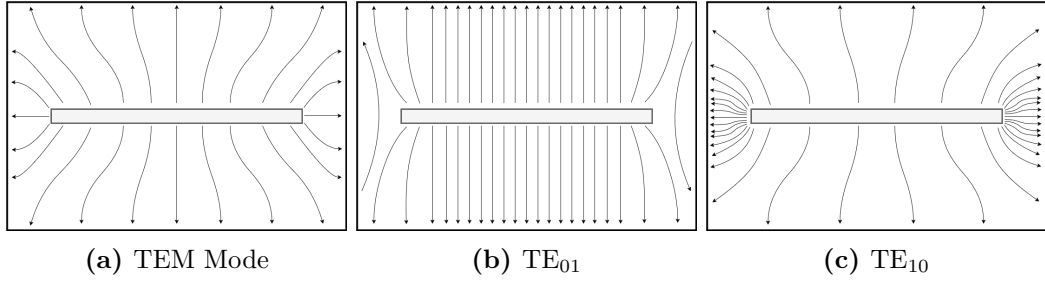


**Figure 3.5** Transversal electric fields in cross section of TEM cell

dependent on the width  $a$ . Note that a port impedance of  $50\Omega$  is only kept in the case  $a = 40\text{ mm}$  and  $b = 24\text{ mm}$ . This information is important when varying the TEM cell dimension, as is done when investigating near-field ( $k \cdot r < 1$ ) and intermediate-field ( $k \cdot r = 1$ ) coupling.

**Table 1** Cut-off frequencies of higher order modes depending on TEM cell dimensions

a [mm]	b [mm]	TE <sub>01</sub> f <sub>c</sub> [GHz]	TE <sub>10</sub> f <sub>c</sub> [GHz]
80	24	1.89	2.05
40	24	3.17	3.76
40	48	2.10	3.76

### 3.3.4 Field distributions

## section todo

However, in a TEM cell, the normalized electric field strength is not necessarily symmetrical. Therefore, it must be found out, depending on the position of the dipole moment. In dead center, the normalized electric field only has a z-component. However, with an offset towards z- or y-direction, it will have a y-component, too. Then, the normalized electric field  $\mathbf{e}_0$  can be found with through Equation 3.28a for and Equation 3.28b. For these equations, a known electric dipole moment  $m_{se}$  is used for both the x- and z-direction.  $P_x$  and  $P_z$  describe the output powers at one port, depending on the electric dipole's orientation [23]. When knowing the normalized electric field  $\mathbf{e}_0$  at this point, any magnitude of electric dipole moments may be derived by scaling the coefficients  $a$  and  $b$ . When only considering dipole moments in z-direction, then only Equation 3.28b is needed.

$$e_{0x} = \frac{2\sqrt{P_x}}{m_{se}} \quad (3.28a)$$

$$e_{0z} = \frac{2\sqrt{P_z}}{m_{se}} \quad (3.28b)$$

The normalized electric field of the TEM mode is then given by Equation 3.29a in x-direction and by Equation 3.29b in z-direction [31]. The equations follow from the singular integral-equation approach in [28]. The formula is not valid for the gap regions. However,

since there won't be any dipole moment placed there, this approximation will suffice. These equations are to understand the influence of electrically small structures, which do not align with the TEM modes, but still couple with the TEM cell and influence the results.

$$e_{ox} = \frac{2}{a} Z_c^{1/2} \sum_{m_0=1}^{\infty} \frac{\sinh M(b - pz)}{\sinh Mb} \cdot \sin Mx \sin Ma J_0(Mg) \quad (3.29a)$$

$$e_{oz} = p \frac{2}{a} Z_c^{1/2} \sum_{m_0=1}^{\infty} \frac{\cosh M(b - pz)}{\sinh Mb} \cdot \cos Mx \sin Ma J_0(Mg) \quad (3.29b)$$

$Z_c$  is the characteristic wave impedance,  $a$  is half the width of the TEM cell,  $b$  is half its height. The sign-function  $p = 1$  above the septum, and  $p = -1$  below it.  $M = m\pi/2a$  and  $g$  is the length of the gap between the septum and the conducting wall. The index  $m = 1, 3, 5, \dots$  is iterated over odd integers.

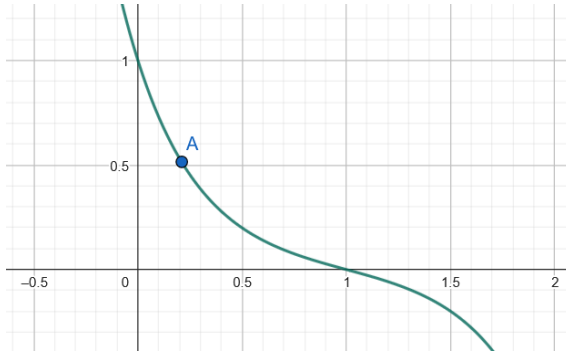


**Figure 3.6** Normalized e-field distribution along z-axis at center of septum for visualization, where the y-axis is the magnitude and the x-axis is the point in the height position in the TEM cell.

$$E_{ox} = \frac{2}{a} Z_c^{1/2} \sum_{m_0=1}^{\infty} \frac{\sinh M(b - py)}{\sinh Mb}$$

$$\cdot \sin Mx \sin Ma J_0(Mg)$$

$$E_{oy} = p \frac{2}{a} Z_c^{1/2} \sum_{m_0=1}^{\infty} \frac{\cosh M(b - py)}{\sinh Mb}$$

$$\cdot \cos Mx \sin Ma J_0(Mg)$$

**Figure 3.7** TODO: This is how the dimensions in these formulas are defined in [28]

The normalized electric field intensity may be derived by the numerically resulting output power when placing dipole moments in the TEM cell. For example, Figure 3.8 demonstrates the output power of an electric dipole moment in the y-direction. It is shifted

Is the series for several sine-waves fitting into the TEM cell, derived due to the nature of the Green's Function? If yes, then only the first-order must be used, since only the TEM mode is propagating. Now higher-order modes here.

Normalized E field: Excited by the dipole at this position. Derived through the Green's function, using said dipole as source. Check this assumption.

in the  $y$ -direction at center height between septum and upper TEM cell wall. Applying Equation 3.28a to the output power leads to the normalized magnitude of the field intensity in  $y$ -direction  $e_y$ . The distribution follows that of the magnitude of a sine wave, according to Equation 3.29a. There, at  $y = 0$  mm, the normalized electric field strength equals zero, and approaches a maximum at  $y = \pm 20$  mm. However, since this equation is valid outside the gap region, and the gap region is not relevant for further research, the is limited at an offset of  $y = \pm 15$  mm.

Furthermore, ?? demonstrates the output power and the normalized  $e_y$ -field across the height from the septum to the upper TEM cell wall. The dipole moment is subject to an offset of  $y = 7.5$  mm from the center. That is because the output power and normalized electric field strength is constantly zero at  $y = 0$  mm, independent of the height.

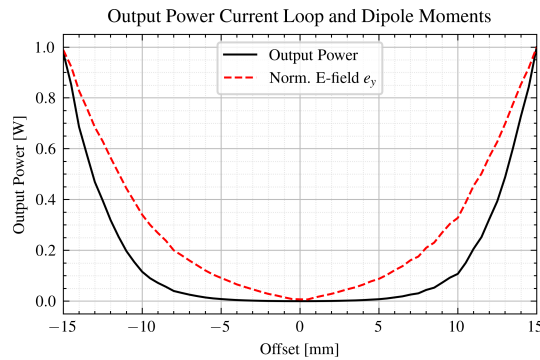


**Figure 3.8** Output power and norm. E-field over offset

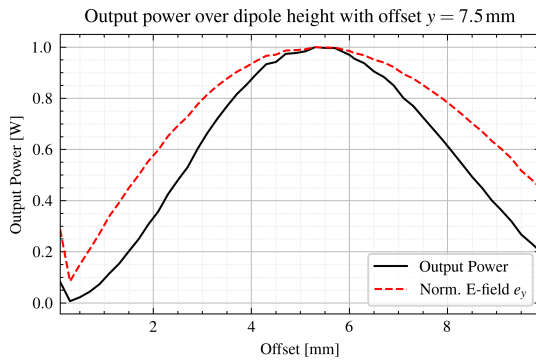


**Figure 3.9** Output power and norm. E-field over height

Any electromagnetic field distribution in a waveguide can be represented by an infinite series of normal modes. Equation 3.30a shows that each mode is orthogonal to each other, with  $\mathbf{e}_n^\pm$  and  $\mathbf{h}_n^\pm$  being the function vectors of the electric and magnetic field in transverse direction [6].  $\mathbf{e}_n^\pm$  and  $\mathbf{h}_n^\pm$  are normalized to  $\sqrt{W}$ . A coupling between the modes only occurs due to geometric changes of the waveguide. Additionally, each mode is normalized to  $\sqrt{W}$ , shown by Equation 3.30b. Only the transverse fields are investigated in these Equations, because they carry power along the waveguide, opposed to the fields in the propagation direction.

$$\iint \mathbf{e}_n^\pm \times \mathbf{h}_m^\pm d\mathbf{s}' = 0 \quad \text{if } n \neq m \quad (3.30a)$$

$$\iint \mathbf{e}_n^\pm \times \mathbf{h}_n^\pm d\mathbf{s}' = 1 \quad (3.30b)$$

The radiated fields can be described by a summation of normal modes, as in ?? and ???. The coefficients of these modes are straightforward to calculate, due to Lorentz Reciprocity Theorem, if the waveguide's walls are perfectly conducting. Ideally, any higher order mode than the first TEM mode will be suppressed, and the calculation simplifies to  $n = 0$ . Additionally, it is assumed that the source is electrically small, which makes it possible to

The electric field / magnetic field distribution of the TEM mode must be known ( $e_0$ ). Other mode distributions are neither available, nor necessary. Calculations to find these field distributions can be found in [30]. This

represent it with dipoles, further simplifying the equations [15]. The fields radiated in the positive z-direction are

$$\mathbf{E}^+ = \sum_n a_n \mathbf{e}_n^+ \quad (3.31a)$$

$$\mathbf{H}^+ = \sum_n a_n \mathbf{h}_n^+. \quad (3.31b)$$

And the fields radiated in the negative z-direction are [6, p. 360]

$$\mathbf{E}^- = \sum_n a_n \mathbf{e}_n^- \quad (3.32a)$$

$$\mathbf{H}^- = \sum_n a_n \mathbf{h}_n^- \quad (3.32b)$$

$a_n$  and  $b_n$  are coefficients with unit  $\sqrt{W}$ , which scale the normalized electric fields of each mode  $\mathbf{e}_n^\pm$ . The fields at the outputs  $\mathbf{E}^\pm$  are decomposed therefore of several propagating modes, each weighted with the coefficients.

### 3.4 Electrically Small Radiating Sources in TEM Cells

#### 3.4.1 Arbitrary source

Suppose a current source  $\mathbf{J}_1$  excites a waveguide (as is the case with the dipoles in the TEM cell). Normally, such a current source requires external fields to drive it, but for they are neglect for now. Only  $\mathbf{E}$  and  $\mathbf{H}$  are considered, which are the fields radiated by  $\mathbf{J}_1$ .  $\mathbf{E}$  and  $\mathbf{H}$  are solved according to  $\nabla \times \mathbf{E} = -j\omega\mu_0\mathbf{H}$  and  $\nabla \times \mathbf{H} = j\omega\epsilon_0\mathbf{E} + \mathbf{J}$  [6, p. 360]. Additionally,  $\mathbf{e}_n^\pm$  and  $\mathbf{h}_n^\pm$  are the resulting waveguide fields, with the signs indicating the direction of propagation. Take Equation 3.2 and set  $\mathbf{J}_2 = \mathbf{M}_1 = \mathbf{M}_2 = 0$ . Now, only the current source  $\mathbf{J}_1$  remains, and the Equation 3.33 emerges.

$$\oint\int_S (\mathbf{e}_n^\pm \times \mathbf{H} - \mathbf{E} \times \mathbf{h}_n^\pm) \cdot d\mathbf{s}' = \iiint \mathbf{J}_1 \cdot \mathbf{e}_n^\pm dv' \quad (3.33)$$

The fields  $\mathbf{E}$  and  $\mathbf{H}$  radiated by  $\mathbf{J}_1$  equal a combination of normal modes. Using the expansions Equations (3.31a) and (3.31b), Equations (3.32a) and (3.32b) lead to

$$\begin{aligned} \oint\int_S (\mathbf{e}_n^+ \times \mathbf{H} - \mathbf{E} \times \mathbf{h}_n^+) \cdot d\mathbf{s}' &= \\ &= \oint\int_S (\mathbf{e}_n^+ \times \sum_m a_m \mathbf{h}_m^+ - \sum_m a_m \mathbf{e}_m^+ \times \mathbf{h}_n^+) \cdot d\mathbf{s}' \\ &= \sum_m a_m \oint\int_S (\mathbf{e}_n^+ \times \mathbf{h}_m^+ - \mathbf{e}_m^+ \times \mathbf{h}_n^+) \cdot d\mathbf{s}'. \end{aligned} \quad (3.34)$$

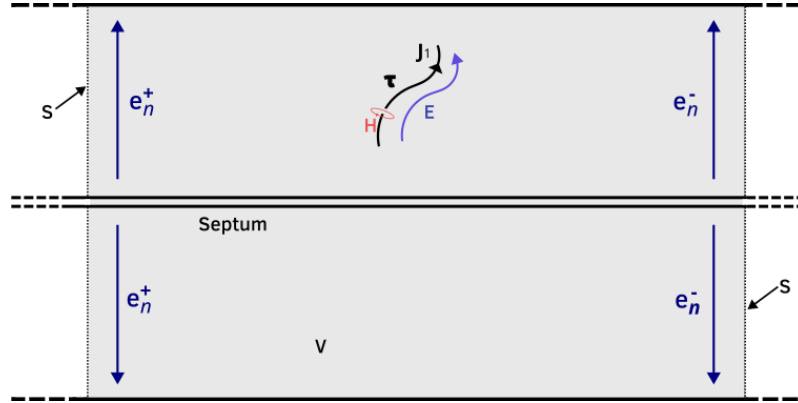


**Figure 3.10** TEM cell with an arbitrary current source  $\mathbf{J}_1$  along the curve  $\tau$ .  $\mathbf{E}$  and  $\mathbf{H}$  are the field intensities induced by the current.  $\mathbf{e}_n^+$  and  $\mathbf{e}_n^-$  are outgoing fields towards both output ports of the TEM cell of arbitrary form.  $\mathbf{S}$  indicates the surface, and  $V$  the volume of the domain in question.

Due to the orthogonal property of Equation 3.30a and the normalization in Equation 3.30b, the coefficients of each mode can be evaluated separately through

$$\begin{aligned} \iint_S (\mathbf{e}_n^+ \times \mathbf{H} - \mathbf{E} \times \mathbf{h}_n^+) \cdot d\mathbf{s}' &= \\ = a_n \iint_S (\mathbf{e}_n^+ \times \mathbf{h}_n^+ - \mathbf{e}_n^+ \times \mathbf{h}_n^+) \cdot d\mathbf{s}' &= -2a_n. \end{aligned} \quad (3.35)$$

The coefficient  $b_n$  of the fields  $\mathbf{e}_n^-$  and  $\mathbf{h}_n^-$  are evaluated in the same manner.

In this equation, the wave amplitudes  $a$  and  $b$  are given through the surface integral in the Lorentz Reciprocity theorem, with  $a$  being the wave going to the left side, and  $b$  to the other.

### 3.4.2 Equivalent dipole moments

The electric dipole moment  $\mathbf{m}_e$  is given by the current  $\mathbf{J}_1$  flowing through the infinitesimal wire. Note that only the electric field of TEM wave propagation is considered. In reality, more modes may propagate, for which the electric field must be replaced by the superposition of normal modes as in Equations (3.31a) to (3.32a).

$$\begin{pmatrix} a_n \\ b_n \end{pmatrix} = -\frac{1}{2} \mathbf{m}_e \cdot \mathbf{e}_n^\pm \quad (3.36)$$

If this arbitrary current distribution forms an infinitesimal loop, the source can be represented by a magnetic dipole moment  $\mathbf{m}_m$ . It is defined by the product  $\mathbf{m}_m = \mathbf{A} \cdot I$ , an infinitesimal current loop with area  $A$  carrying a current  $I$ . This leads to Equation 3.37. This formulation assumes, that the magnetic field strength  $\mathbf{h}^\pm$  does not change over the

loop area, i.e. the loop is electrically small. Otherwise, the magnetic field strength  $\mathbf{h}^\pm$  must be considered in the integration [6, 23].

$$\begin{aligned} \begin{pmatrix} a_n \\ b_n \end{pmatrix} &= - \oint_C \mathbf{e}_n^\pm dl \\ &= - \iint_{S_0} \nabla \times \mathbf{e}_n^\pm d\mathbf{S} \\ &= i\omega\mu_0 \iint_{S_0} \mathbf{h}_n^\pm \cdot d\mathbf{S} \\ &= i\omega\mu_0 \mathbf{m}_m \mathbf{h}_n^\pm \end{aligned} \quad (3.37)$$

If there are several modes propagating, it is useful to find the coefficients of the modes  $a_n$  and  $b_n$  in ?? and ???. In this case, the orthogonality property in Equation 3.30a is used to derive Equation 3.38a and Equation 3.38b [6]. The wire is described by a curve  $C$ , and the tangential vector  $\boldsymbol{\tau}$  is used to integrate along this curve.

$$2a_n = - \int_C \boldsymbol{\tau} \cdot \mathbf{e}_n^- dl \quad (3.38a)$$

$$2b_n = \int_C \boldsymbol{\tau} \cdot \mathbf{e}_n^+ dl \quad (3.38b)$$

An electrically small radiating source may be represented by six dipoles. This number includes three magnetic dipoles pointing in every direction of the Cartesian coordinate system (x, y, and z-direction), and three electric dipoles in the same orientation. Consequently, an equipment under test (EUT) could be modeled with these dipoles, leading to much less computational effort in simulation. The excited EM waves by point sources is discussed in [6] and in subsection 3.3. An analytical procedure to determine these dipole moments is presented by Sreenivasiah [23], and some experimental results based on it can be found in the research of Kreindl, where bond wires were modeled with magnetic dipoles[16], and, again, Sreenivasiah [23].

The idea is to place the EUT in the TEM cell and measure the power of both output ports. The amplitudes of the TEM fields are expressed by Equation 3.39 [23].

$$\begin{pmatrix} a_n \\ b_n \end{pmatrix} = \frac{1}{2} (-\mathbf{m}_e \cdot \mathbf{e}_n^\pm + i\omega\mu_0 \mathbf{m}_m \cdot \mathbf{h}_n^\pm) \quad (3.39)$$

The magnetic field  $\mathbf{h}_n$  and electric field  $\mathbf{e}_n$  are both normalized to  $1\sqrt{\text{Hz}}$  [16] and correspond to the TEM mode in free space [23]. The electric dipole moment  $\mathbf{m}_e$  and the magnetic dipole moment  $\mathbf{m}_m$  are complex vectors, containing an amplitude and phase for every one of the three directions in the coordinate system (x, y, z), and have the units  $\text{A} \cdot \text{m}$  and  $\text{V} \cdot \text{m}$ . The variables  $a$  and  $b$  correspond to the amplitudes of the waves in both possible directions in the TEM cell with the unit  $\sqrt{\text{W}}$ . This leads to the final form in Equation 3.40 [23].

$$\begin{pmatrix} a_n \\ b_n \end{pmatrix} = -\frac{1}{2}(\mathbf{m}_e \pm \mathbf{j}\mathbf{k}\mathbf{m}_m \times \mathbf{z}) \cdot \mathbf{e}_n^\pm. \quad (3.40)$$

$\mathbf{m}_e$  and  $\mathbf{m}_m$  are separately derived by

$$\mathbf{m}_e = \frac{a_n + b_n}{\mathbf{e}_n^\pm}, \quad (3.41)$$

$$\mathbf{m}_m = j \frac{a_n - b_n}{k_0 \mathbf{e}_n^\pm}. \quad (3.42)$$

The unity vector  $\hat{\mathbf{a}}_z$  points in direction of propagation. The function vector  $\mathbf{e}_n^\pm$  describes the normalized electric field amplitude in traverse direction, i.e. x and y-directions, of the excited fundamental mode. Due to the normalization of the electric and magnetic fields to  $1/\sqrt{W}$ , the total power at one port is  $1/2 W$ . This defines  $\mathbf{e}_n^\pm$  as the electric field of the TEM cell, excited with a peak unit power (1 W).

Note, that an electric dipole in the TEM cell leads to a increase in power with the same phase in both ports, and a magnetic dipole leads to the same increase, but with a phase shift of  $180^\circ$ . This also explains why the EUT shall be place halfway on the septum in x-direction. Any shift from this position changes this phase shift from  $180^\circ$ . It is therefore required to measure the power of the ports with phase information, like using a complex Poynting vector, which is easy to implement in a simulation software. When measuring a device with a real TEM cell, the phase information may be found by summing and subtracting the output powers of the ports, as is shown in [23].

### 3.4.3 Electrically small antennas

The electric field coupling with an electrically small antenna can be simply put as [6, p. 361]

$$2a_n = - \int_C \boldsymbol{\tau} I(l) \cdot \mathbf{e}_n^+ dl. \quad (3.43a)$$

$$2b_n = - \int_C \boldsymbol{\tau} I(l) \cdot \mathbf{e}_n^- dl. \quad (3.43b)$$

Since the antenna is electrically small, the electric field  $\mathbf{e}_n^\pm$  is assumed to be constant in  $C$ . Furthermore, if the current  $I$  is constant along  $C$ , it does not have to be considered in the integration. Integrating over the closed loop simplifies to [6, p. 361]

$$2a_n = - \oint_C \mathbf{e}_n^+ \cdot \boldsymbol{\tau} dl = j\omega\mu_0 \iint_S \mathbf{h}_n^+ d\mathbf{s}' = V_n^+, \quad (3.44a)$$

$$2b_n = - \oint_C \mathbf{e}_n^- \cdot \boldsymbol{\tau} dl = j\omega\mu_0 \iint_S \mathbf{h}_n^- d\mathbf{s}' = V_n^-. \quad (3.44b)$$

The induced voltage  $V_n^+$  causes or is caused by the fields at one port  $\mathbf{e}_n^+$ ,  $\mathbf{h}_n^+$ , and the induced voltage  $V_n^-$  by the fields at the other port  $\mathbf{e}_n^-$ ,  $\mathbf{h}_n^-$ . The induced voltages  $V_n^+$  and  $V_n^-$  relate to the magnetic dipole moment  $\mathbf{m}_m$  and the coefficients  $a$  and  $b$ . Defining a total induced voltage as  $V_n = V_n^- - V_n^+$  leads to

$$\mathbf{m}_m = \frac{a_n - b_n}{\mathbf{e}_n^\pm \cdot k_0} = \frac{V_n}{\mathbf{e}_n^\pm \cdot k_0}. \quad (3.45)$$

In a similar manner to Equations (3.43a) and (3.43b), a constant magnetic field  $\mathbf{h}_n^\pm$  along  $C$ , where a magnetic current is present, leads to

$$2a_n = - \int_C \boldsymbol{\tau} I_m(l) \cdot \mathbf{h}_n^+ dl, \quad (3.46a)$$

$$2b_n = - \int_C \boldsymbol{\tau} I_m(l) \cdot \mathbf{h}_n^- dl. \quad (3.46b)$$

Analogous to Equations (3.44a) and (3.44b),  $I_m$  is assumed to be constant and  $C$  to form a closed loop, leading to

$$2a_n = - \oint_C \mathbf{h}_n^- \cdot \boldsymbol{\tau} dl = -j\omega\epsilon_0 \iint_{S_0} \mathbf{e}_n^+ d\mathbf{s}', \quad (3.47a)$$

$$2b_n = - \oint_C \mathbf{h}_n^+ \cdot \boldsymbol{\tau} dl = -j\omega\epsilon_0 \iint_{S_0} \mathbf{e}_n^- d\mathbf{s}'. \quad (3.47b)$$

Now, further surfaces  $S_1$  and  $S_2$  are defined. Surface  $S_1$  leads, starting from  $S_0$ , parallel to the electric field  $\mathbf{e}_n^\pm$  to infinity. Of course, this step only works for the TEM and TE modes, as  $\mathbf{e}_n^\pm$  of TM modes contain components normal to  $S_1$ . A total surface is defined  $S = S_0 + S_1 + S_2$ , where  $S_2$  closes the total surface around  $S_1$  in infinity. Therefore, the total surface covered is closed, and Equations (3.47a) and (3.47b) can be written as

$$j\omega\epsilon_0 \iint_S \mathbf{e}_n^\pm \cdot d\mathbf{S} = j\omega\epsilon_0 \iint_{S_0} \mathbf{e}_n^\pm \cdot d\mathbf{S} + \underbrace{j\omega\epsilon_0 \iint_{S_1} \mathbf{e}_n^\pm \cdot d\mathbf{S}}_{=0} + \underbrace{j\omega\epsilon_0 \iint_{S_2} \mathbf{e}_n^\pm \cdot d\mathbf{S}}_{=0}. \quad (3.48)$$

Inserting Gauss' law  $\nabla \cdot \mathbf{E} = \frac{\rho}{\epsilon_0}$  leads to

$$-j\omega\epsilon_0 \iint_S \mathbf{e}_n^\pm \cdot d\mathbf{s}' = -j\omega\epsilon_0 \iiint_V \nabla \cdot \mathbf{e}_n^\pm \cdot dv' = -j\omega \iiint_V \rho_n^\pm \cdot dv'. \quad (3.49)$$

With the continuity equation  $j\omega\rho = -\nabla \cdot \mathbf{J}$  this leads to

$$2a_n = -j\omega \iiint_V \rho_n^+ \cdot dv' = \iiint_V \nabla \cdot \mathbf{J}_n^+ \cdot dv' = \iint_S \mathbf{J}_n^+ \cdot d\mathbf{s}' = I_n^+, \quad (3.50a)$$

Is this true?  
Maybe field components cancel, since they are assumed to be constant.

sketch

$$2b_n = -j\omega \iiint_V \rho_n^- \cdot dv' = \iiint_V \nabla \cdot \mathbf{J}_n^- \cdot dv' = \iint_S \mathbf{J}_n^- \cdot d\mathbf{s}' = I_n^- . \quad (3.50b)$$

Relating the obtained expression to the electric dipole moment from Equation 3.41 with a total current  $I_n = I_n^+ + I_n^-$  delivers

$$\mathbf{m}_e = \frac{a_n + b_n}{\mathbf{e}_n^\pm} = \frac{I_n}{\mathbf{e}_n^\pm} . \quad (3.51)$$

The physical meaning of  $I_n$  is electrical current passing between the septum and the dipole through capacitive coupling with a certain mode, i.e. displacement current. Concluding, the magnetic dipole moment occurs due to induced voltage, while the electric dipole moment due to coupling electric current.

### 3.5 Shielding

Effective shielding is of great interest to reduce EMI of electronic systems. A figure of merit for shielding capabilities of a material is the electromagnetic shielding effectiveness (SE), given in Equation 3.52 [7].  $E_i$  is the incident electric field, while  $E_t$  is the transmitted electric field, also depicted in Figure 3.11. It depends on the thickness and shape of the material, and its electric and magnetic properties. Additionally, the TEM cell contributes to the SE values.

$$SE_{dB} = 20 \log \left( \frac{E_i}{E_t} \right) \quad (3.52)$$

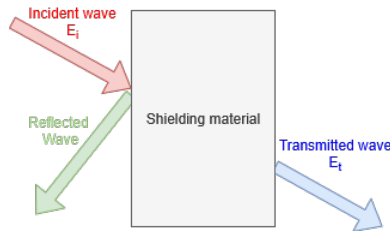


**Figure 3.11** Incident, reflected and transmitted electric fields due to interaction with shielding material

An electromagnetic wave may undergo several reflections inside the shielding material, with each reflection adding up to the total reflected, absorbed and transmitted waves. The total shielding effectiveness is therefore determined by Equation 3.53, according to Schelkunoff.  $A_{dB}$  represents the absorption losses traveling through the shield,  $R_{dB}$  the reflection losses, and  $B_{dB}$  is the correction factor for the multiple reflections inside the shield [7].

$$SE_{dB} = R_{dB} + A_{dB} + B_{dB} \quad (3.53)$$

Calculate with S-params  $S_{11}$  and  $S_{21}$ : A, R and T.

This approach to shielding with internal re-reflections in the shielding material was derived by Schelkunoff. [https://www.ieee.li/pdf/viewgraphs/fundamentals\\_electromagnetic\\_shield.pdf](https://www.ieee.li/pdf/viewgraphs/fundamentals_electromagnetic_shield.pdf)

The reflections occur due to the change in wave impedance. They are described through a reflection coefficient  $R$ . Additionally, it is common to normalize the wave impedance  $Z$  to the free-space wave impedance  $Z_0$ . At the interface from free-space to a shielding material, this leads to Equation 3.54 [6].

$$R = \frac{Z - 1}{Z + 1} \quad (3.54)$$

$$Z = \frac{1}{Z_0} \sqrt{\frac{i\omega\mu}{\sigma + i\omega\epsilon}} \quad (3.55)$$

The reflection coefficient can be converted into dB, leading to  $R_{\text{dB}}$ . Any additional reflection happen due to re-reflections inside the shielding material, described by  $B_{\text{dB}}$ . The rest of the energy must either be absorbed, described by  $A_{\text{dB}}$  or transmitted, shown by  $T_{\text{dB}}$ .

The wave number  $k$  in lossy media is described in a real and imaginary parts as in Equation 3.56. The imaginary part  $\alpha$  is the attenuation or absorption coefficient. It describes the reduction of the intensity of the wave, which occurs with  $e^{-\alpha x}$ , where  $x$  is the coordinate direction of propagation. The real part  $\beta = \frac{2\pi}{\lambda}$  is the phase constant [12].

$$k = \beta + i\frac{\alpha}{2} \quad (3.56)$$

$$\mathbf{E} = \mathbf{e} \cdot e^{-jkx} \quad (3.57)$$

When the molecules in a material are exposed to electric fields, they will polarize, described by their permittivity  $\epsilon$ . When exposed to a magnetic field, the spinning of their electrons in the atoms align with the magnetic field, described by the permeability  $\mu$  of the material. When the fields alternate over time, the molecules will always move and align according to them. This is essentially a movement of charges, and therefore described by a conductivity  $\sigma$ . The energy lost in this process is dissipated as heat [1].

The electric field will push charges in polarizable molecules apart. This separation of charges may be described as an electric dipole, depending on the separation distance and the charge. Under alternating electric fields, the moving of charges will contribute to  $\sigma$ . This phenomenon is called dielectric hysteresis. Equation 3.58 quantifies it by a loss tangent  $\tan \delta_e$  [1]. There,  $\sigma_s$  is the static conductivity, meaning the conductivity of the material for static fields. The complex part of the permittivity  $\epsilon''$  describes the lossy part of the dielectric material, specifically relevant for the alternating fields case. The real part of the permittivity is lossless and is noted by  $\epsilon'$ . The overall complex permittivity is therefore  $\epsilon = \epsilon' + i\epsilon''$ .

$$\tan \delta_e = \frac{\sigma_s}{\omega\epsilon'} + \frac{\epsilon''}{\epsilon'} \quad (3.58)$$

p. 309  
Classical  
Electrodynamics  
(John  
David  
Jackson)  
describe  
shielding  
material  
by dipole  
moments

Formula  
 $\alpha$ ?  
Needed?

S-  
parameters  
should  
enable  
derivation  
of  $\alpha$ . Due  
to normal  
incident  
wave of  
TEM,  
no angle  
needed to  
consider.

Basics:  
Balanis  
2012 page  
68?

The loss tangent therefore  $\tan \delta_e$  relates the conductivity of a material to the real permittivity. A dielectric with low losses has a much larger displacement current than conduction current density ( $\tan \delta_e \ll 1$ ). The opposite is true for a good conductor ( $\tan \delta_e \gg 1$ ) [1].

The loss tangent  $\tan \delta_e$  is a function of frequency, however, it is often not stated as such. Therefore, the loss tangent of FR4, for example, is given as  $\tan \delta_e = 0.02$  for frequencies up to 1 GHz. For higher frequencies, the molecules may have resonance frequencies, where they influence more strongly the overall conductance and consequently increase the imaginary part of the permittivity  $\epsilon''$ .

There are also magnetically lossy materials, which is introduced by a complex permeability  $\mu = \mu' + i\mu''$ . Analog to the dielectric case, the permeability can also be described by a loss tangent  $\tan \delta_m$  as shown in Equation 3.59. However, the loss tangent is very low for the majority of materials and will be neglected. Ferrites are an exception, which are commonly used to dampen high frequency signals [1].

$$\tan \delta_m = \frac{\mu''}{\mu'} \quad (3.59)$$

Electric fields dominate in the near-field region of electric dipoles. To shield them, high permittivity and high conductivity materials, ideally with a high loss tangent  $\tan \delta_e$  shall be used. On the other hand, magnetic fields dominate in the near-field region of magnetic dipoles. For shielding them, high permittivity and high conductivity materials, again with a high loss tangent  $\tan \delta_m$  shall be used.

describe  
 $\alpha$  and  $\delta$   
for ab-  
sorption.  
Then re-  
flections  
with  $\epsilon$   
and  $\mu$   
source

### 3.5.1 ASTM ES7-83 Method

The ASTM ES7-83 method is used to determine the shielding effectiveness of shielding materials. The shielding material is inserted into a coaxial TEM cell around the septum. Ideally, they form a continuous connection [21].

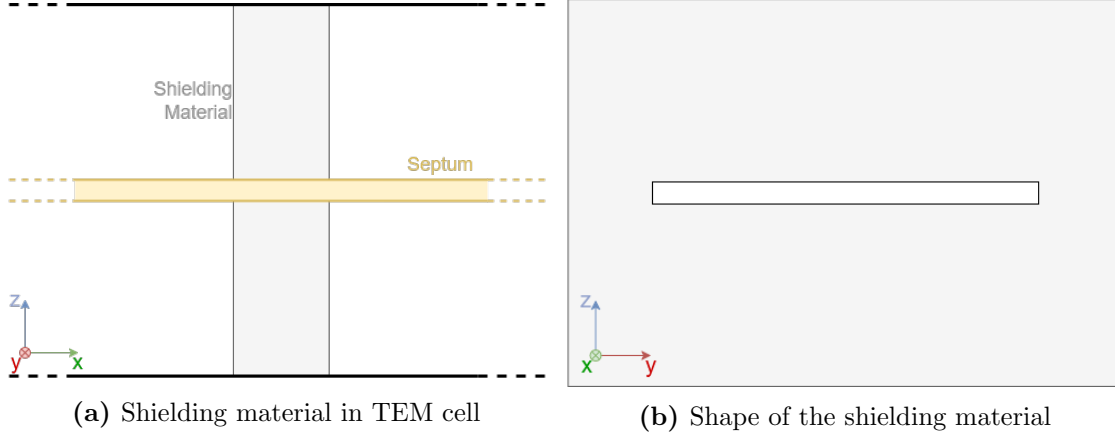
In this method, two measurements are performed with an oscilloscope attached to the output of the TEM cell. In the first, an empty TEM cell is excited and a reference output voltage  $U_{\text{ref}}$  is measured. In the second, the TEM cell is loaded with the shielding material, and the output voltage  $U_{\text{load}}$  is again noted. The measurement values are then used in Equation 3.60 to derive the shielding effectiveness  $SE_{\text{dB}}$  [21].

$$SE_{\text{dB}} = 20 \cdot \log \left( \frac{U_{\text{ref}}}{U_{\text{load}}} \right) \quad (3.60)$$

In the case of simulating the problem, such a procedure may be used, too. It is more convenient, then, to define a reference output power  $P_{\text{ref}}$  for an unloaded TEM cell, and a output power for the loaded case  $P_{\text{load}}$ . This leads to the similar Equation 3.61.

$$SE_{\text{dB}} = 10 \cdot \log \left( \frac{P_{\text{ref}}}{P_{\text{load}}} \right) \quad (3.61)$$

Additionally, a rectangular TEM cell is used for this method, instead of the commonly used cylindrical version. Figure 3.12b shows the cross section of this shielding material, which is inserted into the TEM cell. In Figure 3.12a the shielding material can be seen wrapped around the septum.



Then, the S-parameters derived in the simulations are used to get to the output powers  $P_{\text{ref}}$  and  $P_{\text{load}}$ . By exciting the TEM cell with a power of 1 W, the reference power  $P_{\text{ref}} = 1 \text{ W}$ . The measured power is then derived through Equation 3.62.

$$P_{\text{load}} = P_{\text{ref}} \cdot 10^{|S_{12}|/10} \quad (3.62)$$

### 3.5.2 Dual TEM cell

The shielding effectiveness of a material may also be determined using two TEM cells, which are stacked upon each other, as shown in Figure 3.13. They are connected through an aperture, which can be filled with the shielding material. One TEM cell is excited, and therefore acts as a driving cell. It transmits power through the aperture. It is measured at the second TEM cell, which acts as a receiver. The dual TEM cell simulates near-field conditions, opposed to the far-field conditions simulated by the simple TEM cell [21]. This is important when using the shielding material to shield an antenna's radiation by placing the material directly next to it.

The electrically small aperture may be described by an electric and a magnetic dipole moment. Their magnitude is related to the electric and magnetic coupling between the TEM cells over the aperture. Therefore, the electric and magnetic coupling can be determined separately by adding or subtracting the output powers of the receiving TEM cell [21, 30]. Consequently, an electric shielding effectiveness  $SE_{\text{dB}}^{\text{e}}$  can be calculated with Equation 3.63a, and a magnetic shielding effectiveness  $SE_{\text{dB}}^{\text{m}}$  with Equation 3.63b. If a material, for example, permits energy transfer because of magnetic dipoles in it, then a measurement with lower  $SE_{\text{dB}}^{\text{m}}$  than  $SE_{\text{dB}}^{\text{e}}$  is to be expected [30].

Describe Method.  
Then follows dual TEM cells

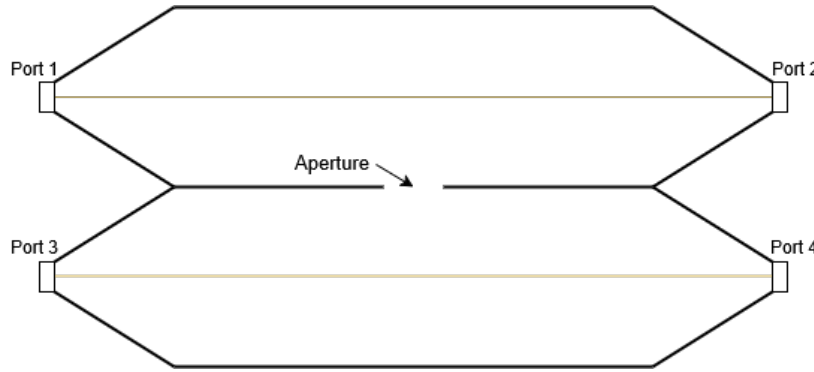
must it be electrically small?

$$SE_{\text{dB}}^{\text{e}} = 10 \log \left( \frac{P_{\text{ref,sum}}}{P_{\text{load,sum}}} \right) \quad (3.63a)$$

$$SE_{\text{dB}}^{\text{m}} = 10 \log \left( \frac{P_{\text{ref,diff}}}{P_{\text{load,diff}}} \right) \quad (3.63\text{b})$$

Because the normalized electric field at the aperture will be of TEM mode, only the component normal to the aperture in z-direction has to be considered. Just as in the case of dipole representation, the Lorentz Reciprocity theorem may be applied to find the fields in the TEM cell. Because both the fields at the output and in the aperture are of TEM mode, only the E-field at the output may be considered.

Since the aperture is electrically small, the field quantities may be assumed to be constant over it. This makes it possible to represent the energy transfer by dipole moments.



Polarization  
of the  
material.  
Small  
aperture  
theory.

**Figure 3.13** Dual TEM cell with aperture

## 4 Numerical Investigations

### 4.1 Finite Element Method

#### 4.1.1 General Idea

Problems involving the calculations of electromagnetic fields are often cumbersome and difficult to solve. This is due to the need of solving differential equations describing these fields over a computational domain, which is not possible with a computer in this sense. The simulation software Ansys HFSS (High Frequency Simulation Software) aims to provide a solution. This software is used for the simulations in section 4, hence it is described in this following, dedicated section.

HFSS uses a numerical technique, namely the Finite Element Method (FEM). The general idea of FEM after Rayleigh-Ritz-Galerkin is to choose a number of basis functions. The goal is to find a linear combination of these basis functions, so that the differential equation is satisfied as closely as possible. This turns the problem of solving a differential equation into a system of algebraic equations, which the computer can process. There is always a set of basis functions which enable the calculation to converge to the real solution. However, the number of basis functions used in the domain is limited, due to reasons of computability [24].

FEM therefore divides the domain into finite elements, i.e. smaller pieces. Then, within each piece, such a basis function is assigned. A linear combination of these basis functions

are found, which satisfy the differential equations. In region where the approximating solution has a high degree of error, the accuracy may be increased by further subdividing the finite elements. This is repeated, until the error falls below a certain threshold, and a precise solution is derived.

#### 4.1.2 Dividing a computational domain into finite elements

The differential equation to be solved is shown in Equation 4.1, where  $\epsilon_r$  is the relative permeability and  $\mu_r$  is the relative permeability of the material. The variable  $k_0$  is the wave number of free space and equals  $k_0 = \omega\sqrt{\epsilon_0\mu_0}$ . [5, 18, 4].

$$\nabla \times \left( \frac{1}{\mu_r} \nabla \times \mathbf{E} \right) - k_0^2 \epsilon_r \mathbf{E} = 0 \quad \text{in } \Omega \quad (4.1)$$

This equation is solved in a computational domain  $\Omega$ . This computational domain is divided into finite elements, called a mesh. Each node in this mesh has polynomial functions assigned, which are weighted to approximate the real solution. It has been proven that tetrahedral finite elements are best suited for this task, as they are geometrically flexible and make the definition of complete polynomial approximation functions possible [22]. Ansys HFSS uses a adaptive finite element mesh generator, which automatically provides a mesh for a given 3-dimensional construction. The Delaunay tessellation for three-dimensions is used for generating a mesh. It efficiently creates a mesh from objects of arbitrary shapes. Any boundary condition can be added recursively to the mesh. At the heart of this algorithm lies the property, that the circumsphere of an tetrahedra's vertices may not contain other tetrahedra's vertices.

Figure 4.1 shows one of such tetrahedrons. At the edge points, the components of the field which are normal to the respective edge and tangential to the face of the element is stored. At the vertex points, the component of a field which are tangential to the edges are stored. The value of the field at any midpoint is derived through interpolation from the node values. The basis function is used for interpolation.

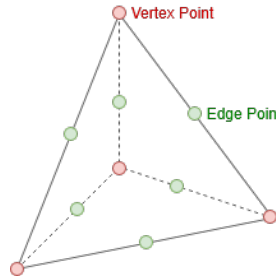


**Figure 4.1** Tetrahedron with points on the edge and vertices.

Because of the way how the fields are stored in the tetrahedra, they are called tangential vector finite elements. Their advantage is that tangential components of fields can be forced to be equal among adjacent tetrahedra at the boundary. For example, an electric field stored at a vertex point must point in the direction along one of the edges, therefore it

is tangential to the element. An adjacent element then has the same tangential electric field imposed at this node, leading to a continuous tangential electric field, therefore satisfying the boundary conditions implied by the Maxwell equation automatically. Furthermore, any Dirichlet boundary conditions can easily be set along the edges. [18].

The finite element is described as Equation 4.2, where  $L_2(\Omega)$  is a set of square integrable functions and  $P_1$  a set of piecewise linear functions in the discretized domain  $\Omega$  [19]. The vector fields at the vertices are given as  $u$ .  $D(\Omega)$  is a set of divergence free functions. The vectors  $u$  used in the finite element therefore

- are continuous in the normal direction.
- are square integrable.
- have a curl describable by piecewise linear functions.

$$H_1^{(\text{dim}=3)}(\text{curl}) = \left\{ \mathbf{u} \mid \mathbf{u} \in [L_2(\Omega)]^3, \nabla \times \mathbf{u} \in [P_1(\Omega)]^3 \cap D(\Omega) \right\} \quad (4.2)$$

Figure 4.2 shows the finite element with the unknowns marked at each point. For reasons of simplicity, only the face is shown. The variables  $u_i^j$  and  $u_j^i$  are imposed across element boundaries, therefore guaranteeing tangential continuity at boundaries. Additionally, they inherently defined a linear polynomial, meaning that they describe a gradient of the field along this edge. Equation 4.3 describes this relation mathematically, where  $\mathbf{t}_{ij}$  is the unit vector tangentially to the edge from node i to node j and  $l_{ij}$  is the length of this edge.

$$\mathbf{u} \cdot \mathbf{t}_{ij} = \frac{1}{l_{ij}} (u_i^j - u_j^i) \quad (4.3)$$

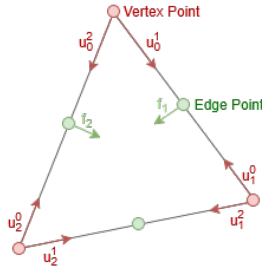


**Figure 4.2** Face of the finite element with unknowns

Two facial unknowns  $f_1$  and  $f_2$  are added to two of the three edge points at one face. Contrary to the variables  $u_i^j$ , the facial unknowns  $f_i$  are only assigned locally at each element and do not cross boundaries. The purpose of the facial unknowns  $f$  is to provide a quadratic polynomial for the field component normal to the edges. This will lead to a linear approximation for the curl of the unknown vector field  $\nabla \times \mathbf{u}$ , providing sufficient accuracy. The overall vector field of this element is then calculated by a superposition of all nodes' vector attributions.

### 4.1.3 Solving the differential equation

A testing function  $\mathbf{W}_n$  is defined, which is multiplied to Equation 4.1. Integrating over the whole test volume then leads to Equation 4.4. This yields  $N$  equations, with  $n = 1, 2, \dots, N$ , for each finite element in the domain  $\Omega$ . This is a common procedure in FEM, and it works through orthogonalization of the residual of Equation 4.1 with respect to the function  $\mathbf{W}_n$ . This means the new goal of the solution is to minimize the residual by making  $\mathbf{W}_n$  as orthogonal as possible [20].

$$\int_{\Omega} \left( \mathbf{W}_n \cdot \nabla \times \left( \frac{1}{\mu_r} \nabla \times \mathbf{E} \right) - k_0^2 \epsilon_r \mathbf{W}_n \cdot \mathbf{E} \right) dV = 0 \quad (4.4)$$

Using the vector identity  $\nabla \cdot (\mathbf{a} \times \mathbf{b}) = (\nabla \times \mathbf{a}) \cdot \mathbf{b} - \mathbf{a} \cdot (\nabla \times \mathbf{b})$  on Equation 4.4 provides a weak form of the equation, meaning a form of the original partial differential equation, which does not contain all original derivatives [5, 4]. Additionally, boundary terms come into play, as seen in the right hand side of the resulting Equation 4.5. The usefulness in this step has been described as lowering the highest-order derivative, therefore the approximating functions need to guarantee continuity of value, not of slope [11]. Another explanation is the possibility of incorporation of Neumann boundary conditions [20].

$$\int_{\Omega} \left[ (\nabla \times \mathbf{W}_n) \cdot \frac{1}{\mu_r} \nabla \times \mathbf{E} - k_0^2 \epsilon_r \mathbf{W}_n \cdot \mathbf{E} \right] dV = \underbrace{\oint_{\partial\Omega} \left( \mathbf{W}_n \times \frac{1}{\mu_r} \nabla \times \mathbf{E} \right) \cdot d\mathbf{S}}_{\text{Boundary term}} \quad (4.5)$$

Next, the electric field  $\mathbf{E}$  is represented by a superposition of basis functions. When applying Galerkin's method, the basis functions are equal to the test functions  $W_n$ . Equation 4.6 demonstrates the sum of the basis functions, which are weighted with the variable  $x_m$ . These variables  $x$  for all elements have to be solved, to find the electric field  $\mathbf{E}$  over the whole domain. The FEM has therefore reduced the initial wave equation in Equation 4.1 to a simple linear matrix equation  $Ax = b$ , where  $A$  is a known  $N \times N$  matrix,  $b$  contains port excitations and  $x$  is the unknown. Ideally, the basis functions are defined to be zero outside of their adjacent elements. This will result to zero for all entries in the matrix, where the test and basis function do not overlap. Therefore, the matrix is sparse, and will be solved much faster. In the end, other electromagnetic quantities can all be derived through the electric field.

$$\mathbf{E} = \sum_m^N x_m \mathbf{W}_n \quad (4.6)$$

Equation 4.7 shows what the matrix then looks like. Some manipulation on the boundary term have been made, so that it contains the surface impedance  $Z_s$ . The surface impedance defines the ratio of the electric field to the magnetic field on the boundary region. Furthermore, it contains the free space, which equals  $\eta_0 \approx 377 \Omega$ .

$$A_{ij} = \int_{\Omega} \nabla \times \mathbf{W}_i \frac{1}{\mu_r} \nabla \times \mathbf{W}_j dV - k_0^2 \int_{\Omega} \mathbf{W}_i \epsilon_r \mathbf{W}_j dV + ik_0 \left( \frac{\eta_0}{Z_s} \right) \oint_{\partial\Omega} \mathbf{n} \times \mathbf{W}_i \cdot \mathbf{n} \times \mathbf{W}_j dS \quad (4.7)$$

#### 4.1.4 Adaptive solution process

Each finite element therefore has a solved electric field assigned, which should approximate the real solution as closely as possible. To determine the error for each element, Equation 4.1 is evaluated. The elements with the highest residuals contain the largest deviation from the real result, meaning they have a large degree of error. Region in the mesh with large degrees of errors are refined, i.e. the tetrahedral finite elements are split into smaller ones. This allows the FEM solver to recalculate the fields in this region with higher precision, leading to a smaller residual. Consequently, the finite elements represent the fields more accurately, due to a smaller element size and higher resolution [3]. An additional method is increasing the order of the polynomial basis functions of elements with low degree of accuracy.

$$\nabla \times \left( \frac{1}{\mu_r} \nabla \times \mathbf{E}_{\text{solved}} \right) - k_0^2 \epsilon_r \mathbf{E}_{\text{solved}} = \text{residual} \quad (4.8)$$

To determine when the iterative refinement process is done and the solution good enough, some kind of threshold must be defined. One possibility is the Max  $\Delta S$  parameter. It is compared to the difference of S-parameters of the defined excitation ports over two iterations. If, after a mesh refinement, the S-parameters of the ports do not significantly change anymore, meaning change less than Max  $\Delta S$ , then the iterative process can be considered done. This described iterative process is shown in Figure 4.3.

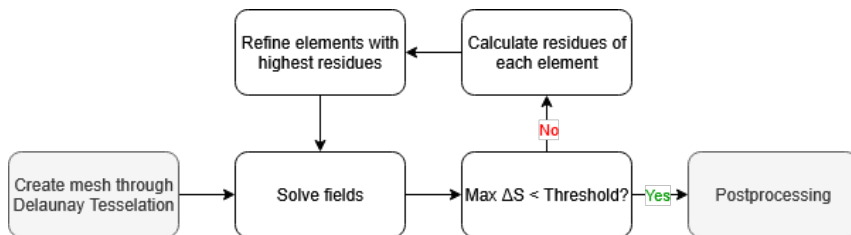


Figure 4.3 Adaptive solution process

## 4.2 Conceptual framework and modeling of antennas

This section is TODO

?? shows the total power maintained in the system, meaning  $S_{11}^2 + S_{12}^2 + S_{13}^2$ . It does not add up to one, meaning that some energy is lost due to finite conductivity of the septum and antenna. This energy dispersion increases with frequency, most likely due to a decrease of the conductivity due to high-frequency effects like the Skin-effect. Consequently, the power consumption in ?? shows a square root relation to the frequency, because the power

Short HFSS introduction with boundary conditions, ports and modal and terminal solutions?

dispersion is so high. When changing the material of the antenna and septum to a perfect electric conductor, the total power in a system remains one (no power is dispersed) and the power consumption over frequency of the antenna shows a quadratic relation to the frequency, due to the quadratic increase of the radiation resistance.

The Skin-effect reduces the area in which the current flows, therefore increasing resistance. This appears due to the reduction of the depth, in which the electromagnetic waves enter. It is also called Skin depth and mathematically described by Equation 4.9b. It depends on the imaginary part of the wave number  $\kappa$ , which is described in Equation 4.9a. For high conducting materials ( $\sigma \gg \epsilon\omega$ ), the dependency of the skin depth  $d$  on the frequency can be described therefore as  $d \propto 1/\sqrt{\omega}$ . Since the power dispersion is linearly proportional to the area of the conductor and therefore Skin-depth, it shows the same dependency on the frequency  $P_{\text{disp}} \propto 1/\sqrt{\omega}$  [8].

$$\kappa = \omega \sqrt{\frac{\epsilon\mu}{2}} \left[ \sqrt{1 + \left( \frac{\sigma}{\epsilon\omega} \right)^2} - 1 \right]^{1/2} \quad (4.9a)$$

$$d = 1/\kappa \quad (4.9b)$$

Own little chapter for skin effect?  
Loop antennas are known for higher conductor losses than radiation  
Balanis page 231

explain better.

Show plots?

At 1 GHz, the dispersed power already equals to 0.46 %, which is much higher than the power transfer of the antenna to one waveport of 1.26e-5 at that frequency. Because this dispersed power is proportional to the square-root of the frequency  $P_{\text{disp}} \propto 1/\sqrt{\omega}$ , the overall transferred power to the antenna shows the same characteristic. However, the power transfer to the waveports has a quadratic dependency on the frequency.

This dispersed power may be ignored in the simulations by changing the antenna's material (main source of power dissipation) and the septum from copper to a perfect electric conductor. The overall power in the system then remains at a constant one over the whole frequency range. Additionally, the transferred power to the antenna now has a quadratic relationship with the frequency, indicating increased radiation efficiency, previously described by ??.

Einige Themen hier sollten zum Theorieteil voriger Kapitel verschoben werden.

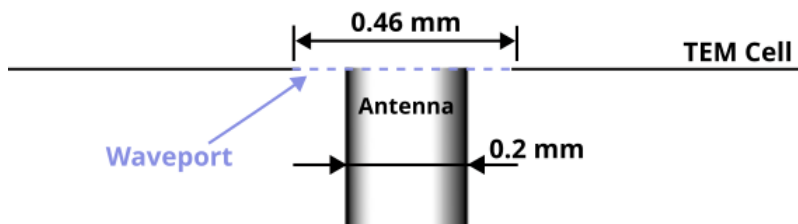


**Figure 4.4** Geometry of an antenna's feedpoint used in simulation. The antenna is fed through a waveport. This geometry leads to a port impedance of  $50 \Omega$ .

The coupling of various electrically small antennas placed in a TEM cell is investigated. Their electric and magnetic coupling is investigated through dipole moments. All antennas

are fed with a power of 1 W. Their material are made of a perfect electric conductor. Different positions and offsets are investigated and the results discussed. They are fed through a round wave port with a diameter of 0.46 mm, and their wire has a diameter of 0.2 mm and free-space permittivity. This results in a reference impedance of  $Z_0 \approx 50 \Omega$ . The TEM cell used has a width of  $a = 40$  mm, a height of  $b = 24$  mm and a length of  $l = 100$  mm, and its cells walls and septum consist of a perfect electric conductor, too. The TEM cell model does not contain the tapered sections at the ports. The ports have an impedance of  $50 \Omega$  due to the TEM cell's geometry.

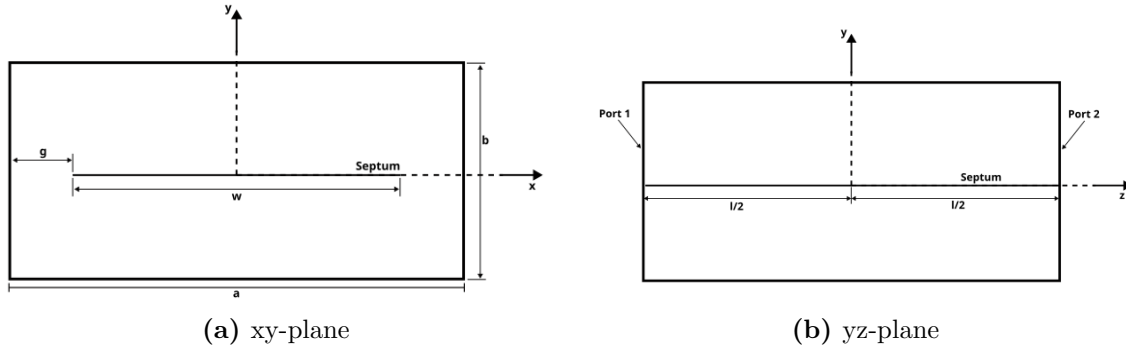


**Figure 4.5** Geometrical arrangement of the TEM cell used in simulations. The front shows the xy-plane, and the side the yz-plane of the TEM cell.

The capacitance and inductance of the TEM cell is derived by calculating the feed current and voltage out of the S-parameters. The capacitance and inductance are then derived through the electric and magnetic peak energy. The values fluctuate slightly over frequency by  $\pm 1\%$ , which is likely due to numerical inaccuracies. The average capacitance and inductance values over the frequency range are chosen. It is therefore assumed that the TEM cell has a constant capacitance and inductance.  $C_T = 6.74 \text{ pF}$ ,  $L_T = 16.25 \text{ nH}$ .

The coupling between the antenna and the two ports of the TEM cell are described by S-parameters, specifically the forward transmission coefficients  $S_{A1}$  and  $S_{A2}$ . The magnitude of this coefficient is the same for the antenna to both ports ( $|S_{A1}| = |S_{A2}|$ ). The power transferred from the antenna  $P_{\text{Antenna}}$  to the output ports  $P_{\text{Out}1}$  and  $P_{\text{Out}2}$  is then derived through

$$P_{\text{Antenna}} = \frac{P_{\text{Out}1}}{10^{|S_{A1}|/10}} = \frac{P_{\text{Out}2}}{10^{|S_{A2}|/10}}. \quad (4.10)$$

The fields are normalized such that

$$\iint_S \mathbf{E}^\pm \times \mathbf{H}_0^\pm \cdot d\mathbf{s}' = 1, \quad (4.11)$$

where the surface  $S$  spans over one of the output ports. The fields are linearly scaled by the complex coefficients  $a$  and  $b$ . If only the TEM mode is considered, only one such pair of coefficients is needed to describe the fields at the output ports. Some investigations

explicitly include the propagation of higher order modes. In this case, each mode is assigned a separate pair of coefficients  $a_n$ ,  $b_n$ . The coefficients  $a$  and  $b$  have the unit  $\sqrt{W}$ .

The coefficients  $a$  and  $b$  have the unit  $\sqrt{W}$ . The fields  $\mathbf{e}_0$  and  $\mathbf{h}_0$  for a TEM cell is known .The normalization condition leads to an output power equal to  $P_{\text{out},1} = |a|^2/2$  and  $P_{\text{out},2} = |b|^2/2$ , which is also found in [30]. This is derived by

$$P_{\text{out}1} = \iint_S \langle \mathbf{S} \rangle \cdot d\mathbf{s}' = \iint_S \frac{1}{2} \Re\{(a \cdot \mathbf{E}^\pm) \times (a \cdot \mathbf{H}^\pm)^*\} \cdot d\mathbf{s}' = \frac{|a|^2}{2}, \quad (4.12a)$$

$$P_{\text{out}2} = \iint_S \langle \mathbf{S} \rangle \cdot d\mathbf{s}' = \iint_S \frac{1}{2} \Re\{(b \cdot \mathbf{E}^\pm) \times (b \cdot \mathbf{H}^\pm)^*\} \cdot d\mathbf{s}' = \frac{|b|^2}{2}. \quad (4.12b)$$

Some plot or table for explanation

Because ideal TEM fields are assumed at the output ports, the Poynting vector has no imaginary component,

$$\mathbf{E}^\pm \times \mathbf{H}^\pm = \Re\{\mathbf{E}^\pm \times (\mathbf{H}^\pm)^*\} \quad \text{for TEM mode.} \quad (4.13)$$

Consequently, if the normalized electric field distribution of the TEM mode  $\mathbf{E}^\pm$  is unknown, it may be derived by setting the output power of a waveport to  $P_{\text{out}} = 1/2 W$ , where  $|a| = |b| = 1/\sqrt{W}$ . For example, the uniformly distributed, normalized electric field along the y-axis in the center of the TEM cell ( $z = 0$ ,  $x = 0$ ) is derived by

$$|a| \cdot \mathbf{E}^\pm(0, y, 0) = 1/\sqrt{W} \cdot \mathbf{E}^\pm = \frac{\sqrt{P_{\text{out}} R_{\text{waveport}}}}{b/2} \quad (4.14)$$

The difference in phase of  $S_{A1}$  and  $S_{A2}$  influence the quantity of magnetic dipole moments and electric dipole moments. If the dipole moments are placed in the center of the TEM cell half-way between both output ports, they will contain the same power, therefore  $|a| = |b|$ . In this case, a phase shift of  $\pi$  indicates the presence of a magnetic dipole moment and the absence of electric dipole moments. This is shown by

$$\mathbf{m}_e = \frac{a + b}{\mathbf{E}^\pm} = \frac{a + a \cdot e^{j\pi}}{\mathbf{E}^\pm} = 0, \quad (4.15a)$$

$$\mathbf{m}_m = j \frac{a - b}{\mathbf{E}^\pm \cdot k_0} = j \frac{a - a \cdot e^{j\pi}}{\mathbf{E}^\pm \cdot k_0} = j \frac{2a}{\mathbf{E}^\pm \cdot k_0}. \quad (4.15b)$$

A phase shift of zero indicates the opposite case. The influence of the electric and magnetic dipole moment is equal, if the phase shift equals  $\pi/2$ .

If only the TEM mode propagates, only the y-component of an electric dipole moment and the x-component of a magnetic dipole moment generates output power, assuming they are centrally located ( $x = 0$ ,  $y = b/4$ ,  $z = 0$ ). This is due to the magnetic field containing only an x-component  $\mathbf{H}^\pm = H_x^\pm e^{\pm k_0 z}$ , and the electric field only an y-component  $\mathbf{E}^\pm = E_y^\pm e^{\pm k_0 z}$  at the center of the TEM cell. An offset of dipole moments or propagation of higher order

Sketch this situation.  
Also,  
 $e^{\pm k_0 z}$  indicated  
that at

modes lead to different field components of  $\mathbf{H}^\pm$  and  $\mathbf{E}^\pm$ , and therefore to a change in coupling. These effects are investigated numerically in subsection 4.8.

A magnetic dipole moment can be expressed equivalently as either an electric current loop or a magnetic line current, as described in Equation 2.17. For infinitesimal magnetic dipoles, this duality simplifies to

$$m_m = j\omega\mu_0 m_0, \quad (4.16)$$

where  $m_m$  (in V·m) denotes the magnetic dipole moment in the magnetic current representation, and  $m_0$  (in A·m<sup>2</sup>) denotes the moment in the electric current representation.

If the output power and phase shifts of the waveports are known, any antenna in the TEM cell may be replaced by an electric and a magnetic dipole moment. Using numeric simulation, the phase shift is determined by measuring the phase shifts of the electric fields at both output ports. When applying this described method in a measurement with a real TEM cell, the phase shift is found by adding and subtracting the output powers of both ports, as is shown in [23].

The energy density is given by [8, p. 330]

$$w_{EM} = \frac{1}{2} \left( \underbrace{\epsilon E^2}_{\text{Electric energy } w_E} + \underbrace{\frac{1}{\mu} B^2}_{\text{Magnetic energy } w_M} \right). \quad (4.17)$$

Integrating  $w_{EM}$  over a volume yields the total electromagnetic energy in this volume. Similarly, integrating  $w_E$  gives the electric energy in said volume, and  $w_M$  the magnetic energy.

If all of the energy is provided by an electrically short antenna, its equivalent reactances can be derived through [8, pp 107, 328]

$$L = 2 \frac{W_m}{I^2} \quad (4.18a)$$

$$C = 2 \frac{W_e}{V^2} \quad (4.18b)$$

All simulations are counterchecked by inserting frequency-dependent dipole moments and checking the power and phase of the output ports.

In the measurement configuration, the TEM cell with an inserted antenna can be modeled as a three-port network. The two output ports of the TEM cell are denoted as ports 1 and 2, while the antenna feed point is represented as port A. The behavior of this system is fully characterized by its scattering matrix, given as

$$[S] = \begin{bmatrix} S_{11} & S_{12} & S_{1A} \\ S_{21} & S_{22} & S_{2A} \\ S_{A1} & S_{A2} & S_A \end{bmatrix}. \quad (4.19)$$

The RMS-value of the current through the feedpoint of the antennas are calculated with those S-parameters,

$$I_{RMS,in} = \sqrt{P_{in}} \frac{(1 - S_{AA})}{\sqrt{Z_0}}, \quad (4.20)$$

$P_{in}$  is the power applied to the port, not considering reflections. The voltage at the feedpoint is calculated in a similar fashion as

$$V_{RMS,in} = \sqrt{P_{in}}(1 - S_{AA})\sqrt{Z_0}. \quad (4.21)$$

Another method to derive voltages and currents is by integration of field intensities. Special care has to be taken at mesh refinement in the area of integration to reduce numerical errors. The impedance seen from the feedpoint is

$$Z_{in} = Z_0 \frac{1 + S_{AA}}{1 - S_{AA}}. \quad (4.22)$$

All values are peak values, unless otherwise stated. The septum of the TEM cell and the material of the antennas are perfectly conducting, to investigating results for coupling effects without distorting them with losses.

### 4.3 Monopole Antenna

#### 4.3.1 Setup

The monopole antenna, shown in Figure 4.6b, is installed at the center of the TEM cell and connected to the feedpoint located on the top wall. It has a length of 5 mm, which makes it electrically short at frequencies up to 6 GHz. It may be approximated as an infinitesimal electric dipole for frequencies up to 1.25 GHz. The equivalent dipole moments  $\mathbf{m}_e$  and  $\mathbf{m}_m$  are derived through Equations (3.41) to (3.42).

The frequency range investigated reaches from 1 MHz to 3 GHz. Figure 3.4 demonstrates the cut-off frequencies of higher-order modes of the TEM cell in use for the simulation, where the cut-off frequency of TE<sub>01</sub> equals  $f_{c,01} = 3.12$  GHz. The output power is influenced by the propagation of this evanescent mode, which must be considered in the simulation results in the upper frequency range.

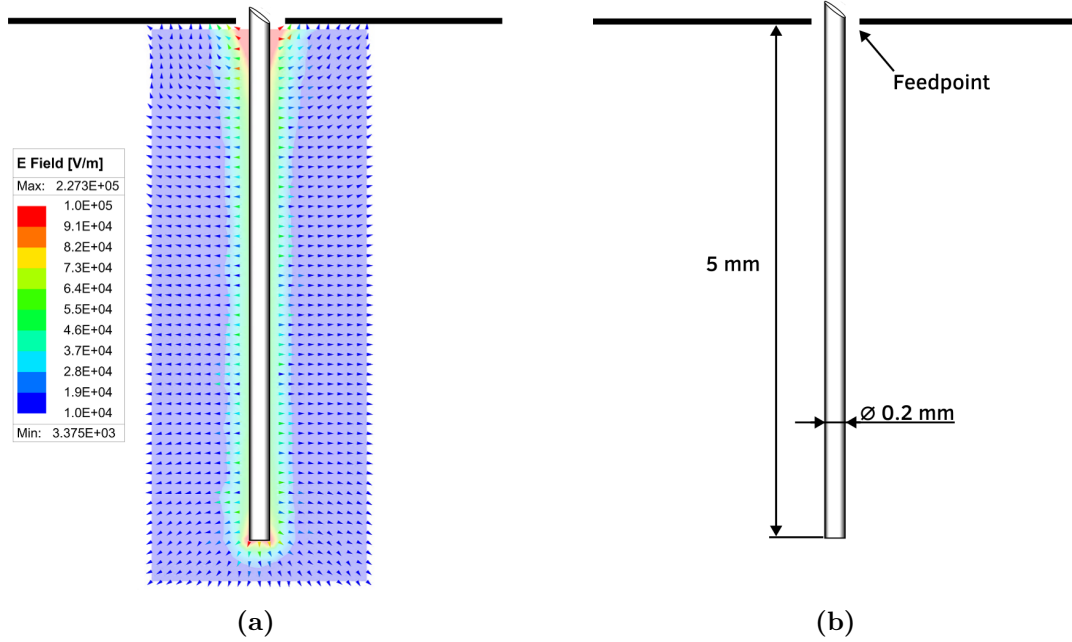


**Figure 4.6** Geometry of monopole antenna inserted into TEM cell with its electric near-field.

#### 4.3.2 Equivalent dipole moments

The electric dipole moment is normalized to the free-space wave impedance to enable comparison with the magnetic dipole moment [16]. The electric dipole moment shown in Figure 4.7a increases approximately linearly over frequency, while the magnetic dipole moment is negligible over the whole frequency range. Consequently, the phase difference between the powers  $\Delta = \varphi_2 - \varphi_1 = 0$  over the whole frequency range.

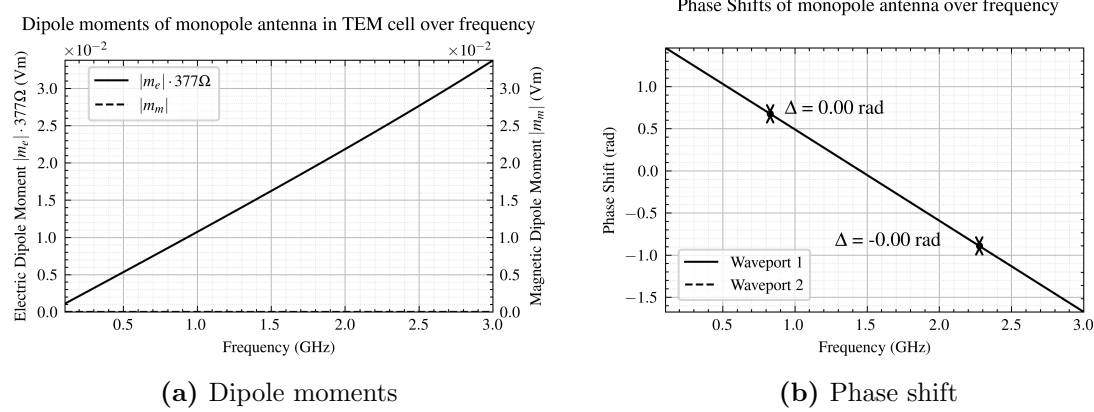


**Figure 4.7** The equivalent dipole moments of the monopole antenna and the corresponding induced phase shift between the wave ports are presented in separate figures.

#### 4.3.3 Electrical characteristics

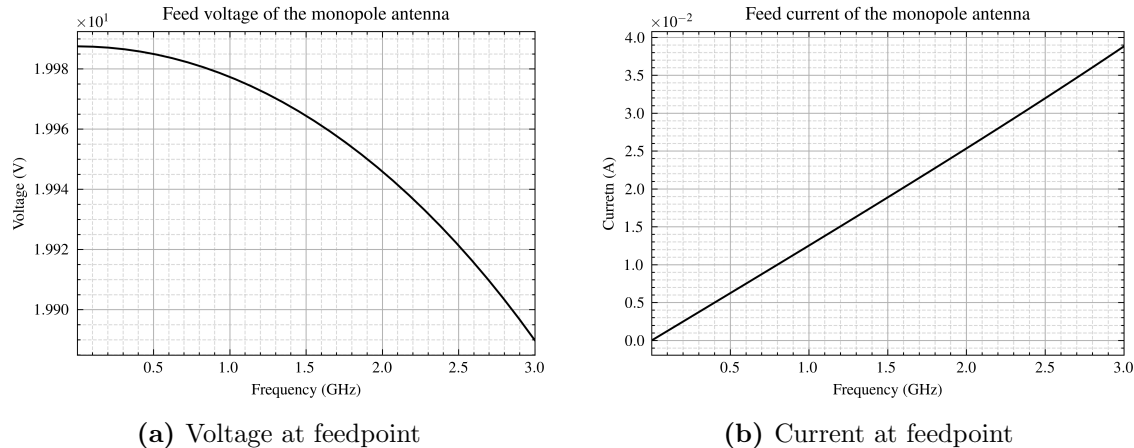


**Figure 4.8** Effective electric current and effective voltage at feedpoint of monopole antenna over frequency.

The electric current present in the monopole antenna is aligned with the electric field  $\mathbf{e}_{\text{TEM}}^{\pm}$  of the dominant TEM mode present in the investigated frequency range. Only the electric dipole moment in y-direction and the magnetic dipole moment in x-direction are needed to model the antenna, because they align with the fields of the TEM mode.

axis typ.  
Maybe  
show peak  
values?

According to Equation 3.33, this will lead to a coupling with the output ports. Equation 3.33 also requires  $\mathbf{e}_{\text{TEM}}^{\pm}$  and the part of  $I$  contributing to the output power to be in phase at the position of the monopole antenna, due to  $\mathbf{e}_{\text{TEM}}^{\pm}$  and  $\mathbf{h}_{\text{TEM}}^{\pm}$  being in-phase at the output ports. Using Equation (3.43a) and ?? and integrating the current  $I$  in Figure 4.8b yields

$$\mathbf{m}_e = \int_C \boldsymbol{\tau} I(l) dl = 82.00 \mu\text{Am} \cdot \hat{\mathbf{a}}_z, \quad (4.23)$$

which is equivalent to  $\mathbf{m}_e = 3.09 \cdot 10^{-2} \cdot \hat{\mathbf{a}}_z \text{Vm}$ , if normalized to the free-space wave impedance  $Z_0 \approx 376.73 \Omega$ . Since the monopole antenna is located in the center,  $\mathbf{e}_{\text{TEM}}^{\pm}$  remains constant over  $y$ .

The voltage  $V$  at the feedpoint in Figure 4.8a remains largely constant over the frequency range. This agrees with the absence of magnetic dipole moment  $\mathbf{m}_m$ , which is directly related to induced voltage according to Equation 3.45. The current  $I$  at the feedpoint in Figure 4.8b rises linearly. According to Equation 3.51, the frequency behavior of  $\mathbf{m}_e$  is proportional to  $I$ . Equation 3.51 cannot directly be applied using  $I$ , because some of this current returns as displacement current to the feedpoint (see Figure 4.6a), not contributing to the electric coupling. Furthermore, this agrees with the quadratically increasing output power in Figure 4.9a and the quadratically increasing radiation resistance determined.

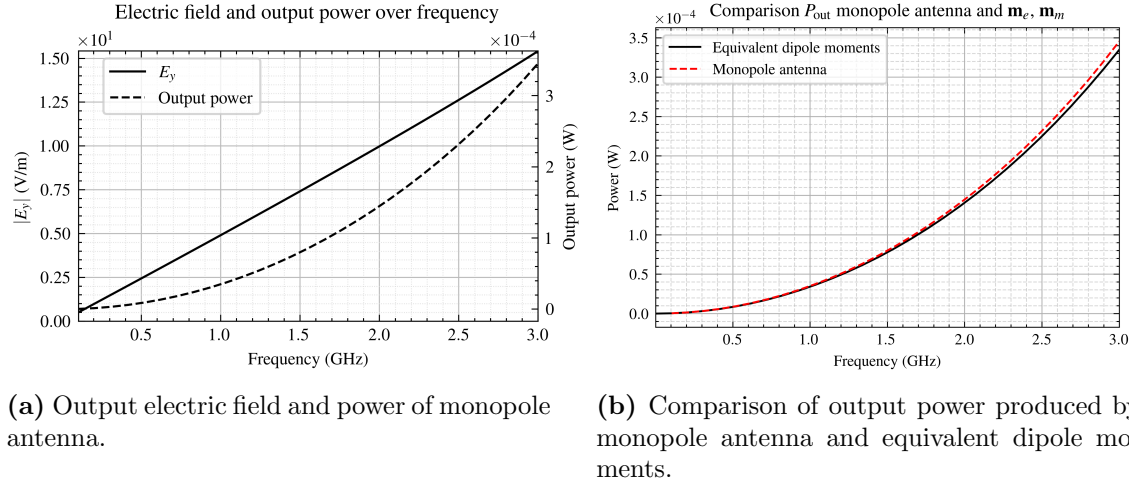


**Figure 4.9** Output power and electric field data of antenna and equivalent dipole moments

The derived equivalent dipole moments  $\mathbf{m}_e$ ,  $\mathbf{m}_m$  positioned in the center of the TEM cell produce output power shown in Figure 4.9b, where they are compared with the monopole antenna. The approximation with the dipole moments worsens, when approaching the cut-off frequency of the first higher-order mode. The coefficients  $a_{01}$  and  $b_{01}$  of the  $\text{TE}_{01}$  have to be considered, which would provide the difference in power to increase accuracy.

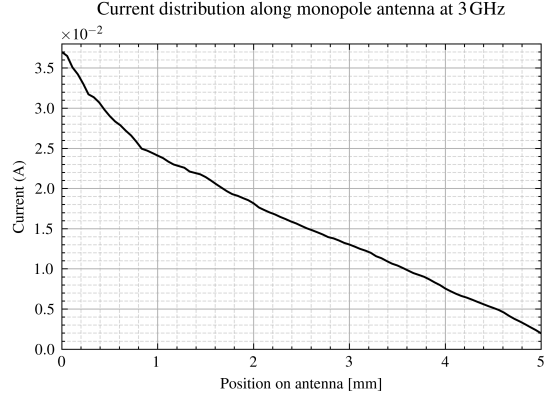
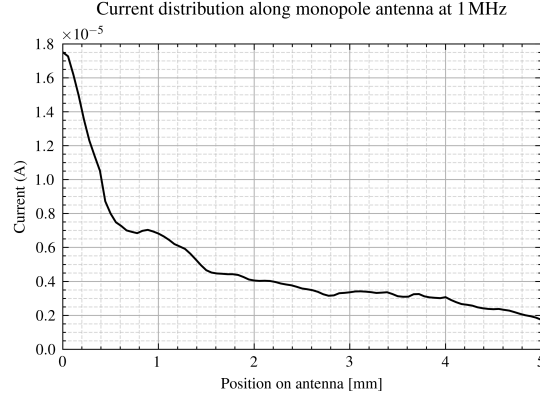
The output power rises quadratically over the frequency, which fits the linearly rising electric dipole moment and the quadratically rising radiation resistance determined in section .

The distribution of the current along the monopole antenna shown in Figure 4.12 is numerically derived by integrating the magnetic field intensity in a closed loop around the antenna at each position.

Near the feedpoint at 0 mm non-linearities become apparent, due to significant displacement current in this region, as Figure 4.6a makes clear. This causes the current in the antenna to rapidly decrease in this section.

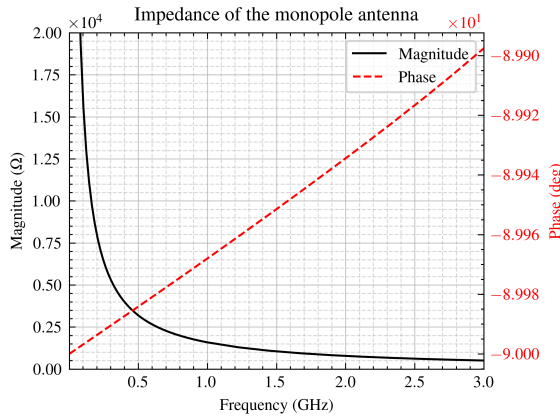
Fill in

can plot quality be improved?  
Max delta S parameter reduction

**Figure 4.10** At 3 GHz**Figure 4.11** At 1 MHz**Figure 4.12** Effective electric current distribution along the monopole antenna at frequencies 1 MHz and 3 GHz

The current distribution at 3 GHz (see Figure 4.10) approximates that of a small electric dipole as described in subsubsection 2.1.2. It shows an approximately linear decrease. Any current observed beyond the antenna length of 5 mm is attributed to displacement current to the septum, as is visible by the increased electric field there in Figure 4.6a.

The current distribution at 1 MHz demonstrated in Figure 4.11 approximately follows the behavior of an infinitesimal electric dipole discussed in subsubsection 2.1.1. There, the current remains nearly constant over some sections of antenna length, decreasing towards the end. Additionally, the magnitude of the current is significantly lower at this frequency.

**Figure 4.13** Magnitude and phase of monopole antenna's impedance.

This frequency-dependent behavior is explained by the impedance of the monopole antenna shown in Figure 4.13. At low frequencies, the antenna impedance demonstrates a high magnitude, which rapidly decreases as frequency increases. Over the whole frequency range, it exhibits highly capacitive behavior, which is consistent with Equation 2.10.

An equivalent circuit is derived in Figure 4.14, which is known as Chu equivalent circuit for a short dipole [10].

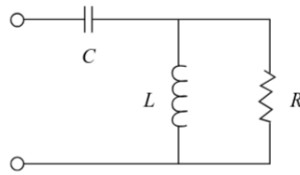


**Figure 4.14** Chu equivalent circuit of short dipole

What is the purpose of this circuit here? Explain more. And should other chapters have circuits, too?

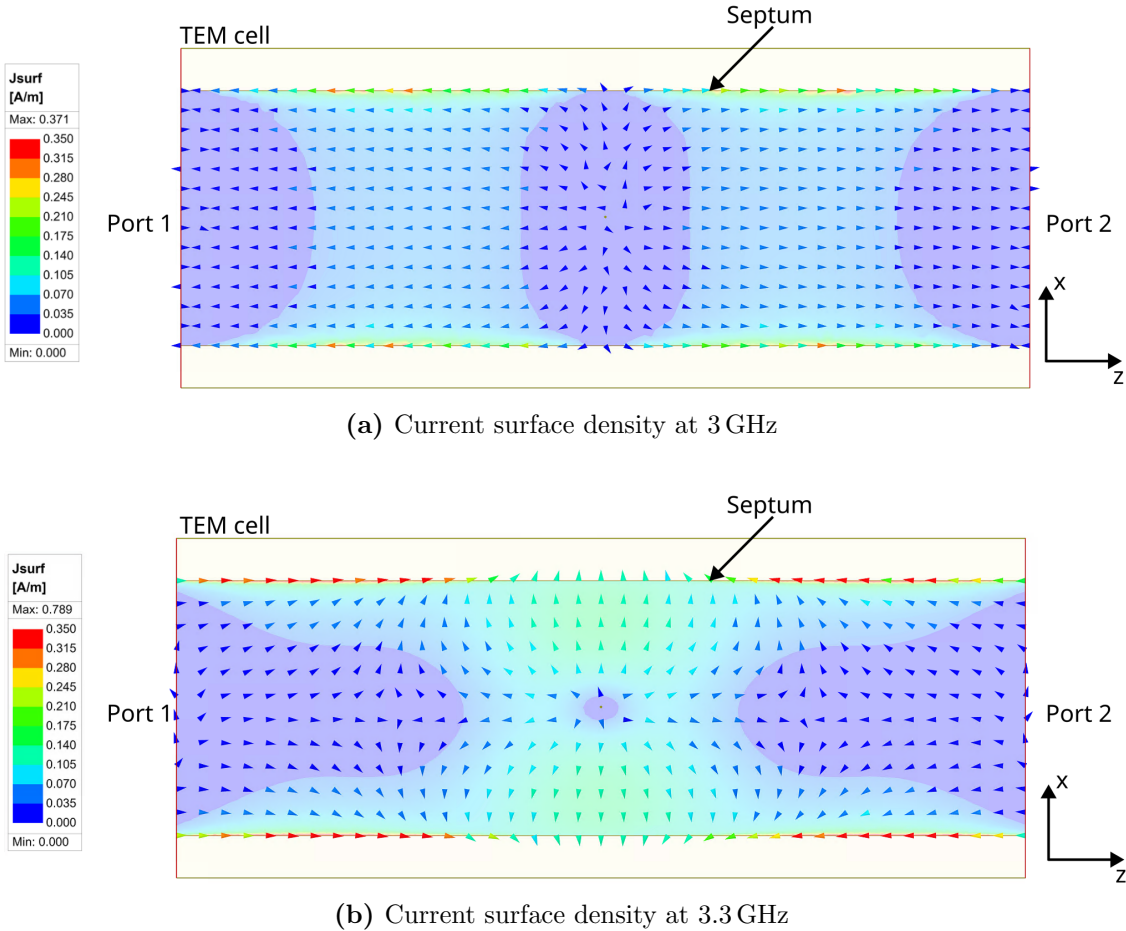
#### 4.3.4 Current distribution on septum and antenna offset

Figure 4.15a shows the surface current density on the septum caused by the monopole antenna. The current heads towards output ports in-phase, which causes the output power to be in-phase, too. This is a characteristic of the dominant electric dipole moment, predicted by .

Figure 4.15b shows the current density of the septum at 3.3 GHz. Due to the magnetic fields propagating in the z-direction, the current on the septum creates a pattern of swirls. Current, which reach an output ports by following this pattern, contributes to the total power transferred by the TE<sub>01</sub> mode.

idea: offset in z-direction, show surface current how it gets a phase shift at waveports, and a magnetic dipole moment appears to be induced

idea: offset in x-direction, showing surface current and explaining the decrease in power transfer (normal E-field distribution)



**Figure 4.15** Current surface densities at different frequencies, below and above the cut-off frequency of the  $TE_{01}$  mode.

#### 4.3.5 Electromagnetic energy in the TEM cell

The antenna produces electromagnetic energy in the TEM cell, which is derived by Equation 4.17. This gives information about the real and imaginary power consumed by the antenna. Furthermore, it is possible to derive the inductance and capacitance of the monopole antenna in the TEM cell through Equation (4.18a) and ???. With help of the peak electrical energy shown in Figure 4.16, the reactances turn out to be

$$L = \text{todo} \quad (4.24a)$$

$$C = \text{todo} \quad (4.24b)$$

As discussed previously, the monopole antenna demonstrates capacitive behavior and has a lot of voltage. This leads to the electromagnetic energy to be predominantly electric.

Problem:  
eqc has  
series cir-  
cuit, for  
which  
must be  
accounted

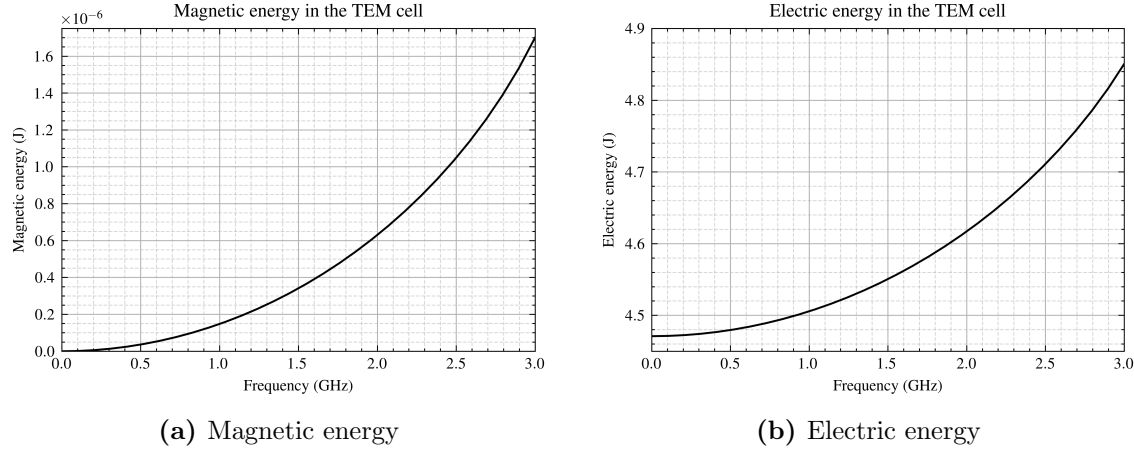


**Figure 4.16** Peak electromagnetic energy in the TEM cell generated by the monopole antenna

## 4.4 Loop antenna

### 4.4.1 Setup

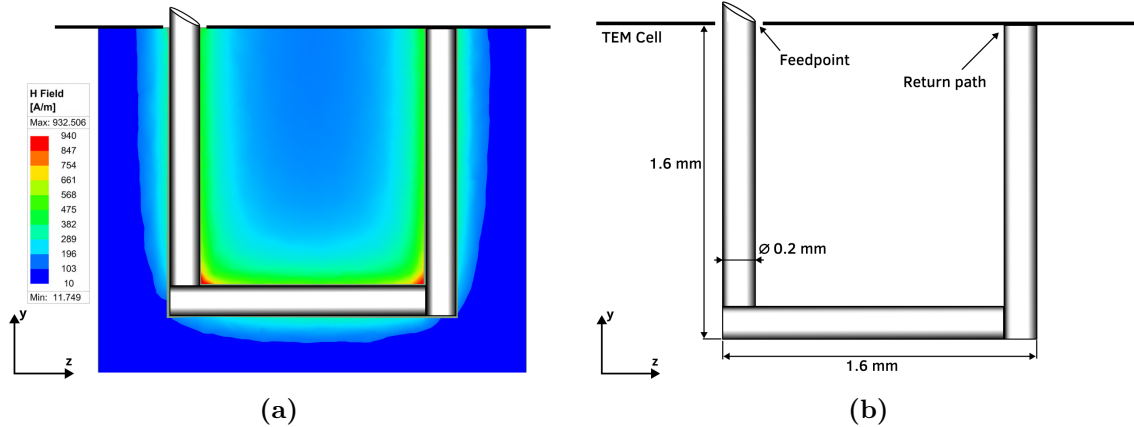
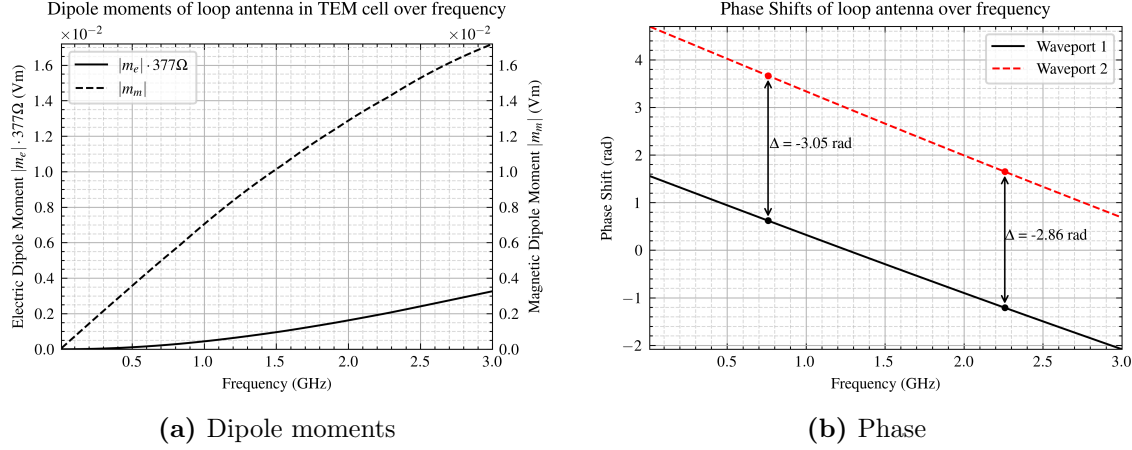


**Figure 4.17** Geometry of loop antenna inserted into the TEM cell with its magnetic near-field. The return path leads into the conducting surface of the cell.

A square loop antenna is placed in the center of the TEM cell. Each side has a length of 1.6 mm, hence it is electrically short for frequencies up to 4.69 GHz. The square form is preferable to a round antenna in the following numerical simulations, due to more accurate mesh modeling and clearer investigation of the resulting dipole moments. The normal vector of the loop surface points in x-direction. The frequency investigated ranges from 1 MHz to 3 GHz, unless otherwise stated, and the input power of the antenna remains at 1 W.



(a) Dipole moments

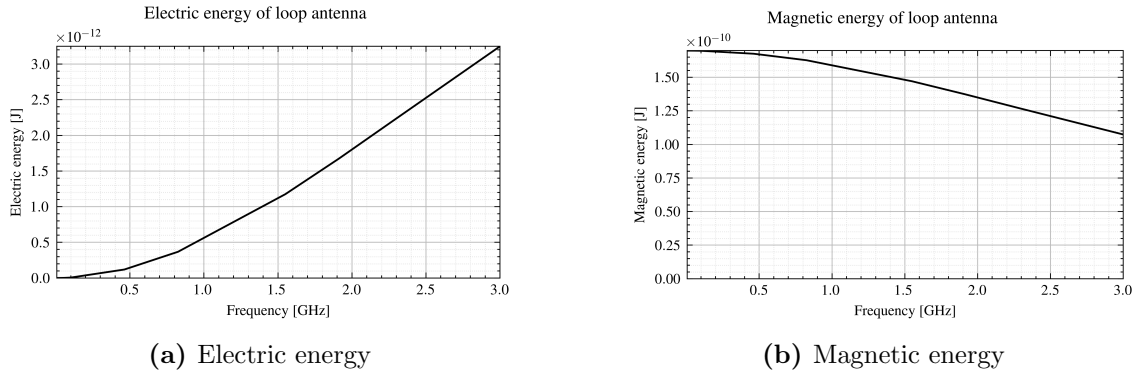
(b) Phase

**Figure 4.18** Dipole moments and phase shift of loop antenna.

#### 4.4.2 Equivalent dipole moments

The dipole moments are plotted in Figure 4.18a. The amount of magnetic flux passing through the area of the loop antenna lead to the large magnitude of  $\mathbf{m}_m$ , as described by Equation (3.44a) and ?? and Equation 3.45.  $\mathbf{m}_e$  is created by the current in the loop antenna according to Equation (3.43a) and ??, which partially points in direction of  $\mathbf{e}_{\text{TEM}}^{\pm}$ . Opposed to the case of a monopole antenna,  $\mathbf{m}_e$  and  $\mathbf{m}_m$  demonstrate non-linear behavior over frequency, which is investigated further in subsubsection 4.4.3.

#### 4.4.3 Electrical characteristics



(a) Electric energy

(b) Magnetic energy

**Figure 4.19**

The current  $I$  in the loop antenna changes along the antenna wire as shown in Figure 4.21, indicating displacement current coupling back to the septum and back to the feedpoint, also seen in the slightly changing magnetic field intensity in Figure 4.17a. Consequently,  $\mathbf{m}_e$  gains a significant magnitude according to Equation 3.51, influencing the electric coupling behavior of the antenna. The feedpoint current is derived through integration of  $\mathbf{H}$  in a closed loop of radius 0.11 mm, measured 0.17 mm above the feedpoint. The return path current is measured at the same height above the PEC surface. The results vary

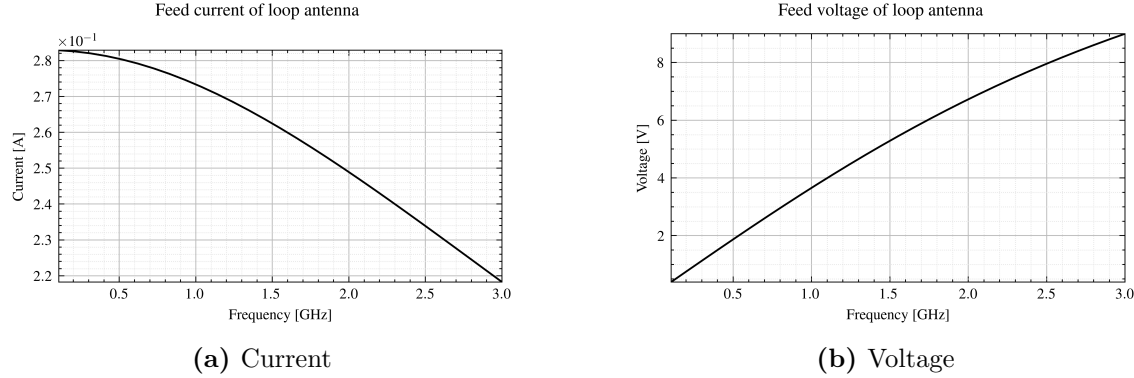


**Figure 4.20** Voltage and current at feedpoint of the loop antenna.

with position due of the displacement currents in the antenna's near-field.

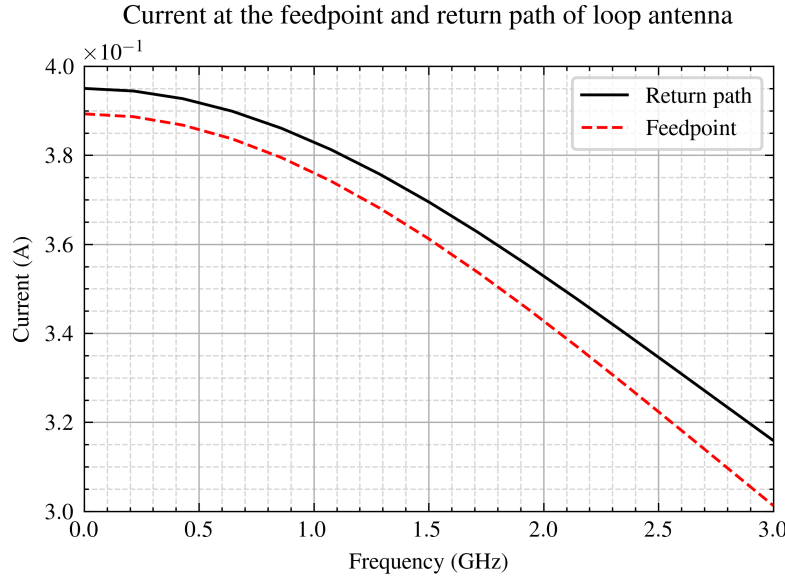


**Figure 4.21** Peak currents of loop antenna at feedpoint and return path.

Insert free-space PEC loop simulations.

Figure 4.20b demonstrates the voltage at the feedpoint of the antenna, which significantly rises over the frequency. Because the increase in voltage leads to larger displacement current according to Equation 3.51,  $\mathbf{m}_e$  follows its frequency-behavior. Similarly, the reduction in current over frequency, shown in Figure 4.20a, leads a lower induced voltage, and according to Equation 3.45 a smaller magnitude of  $\mathbf{m}_m$ . The current and the voltage are determined with Equations (4.20) and (4.21).

The increases in voltage and decrease in current follows from the impedance, depicted in Figure 4.22. The strongly inductive impedance increases linearly over frequency, keeping the input power constant leads to the observed behavior.

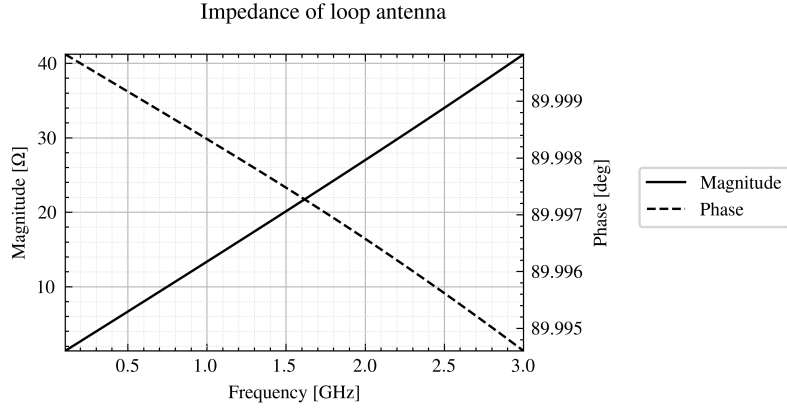


**Figure 4.22** Magnitude and phase of the impedance of the current loop antenna.

#### 4.4.4 Equivalent circuit model

A better understanding and an useful model for calculations is an equivalent circuit model. Figure 4.23a demonstrates an equivalent circuit for the electrically small loop antenna, where  $C$  models stray capacitances,  $R_L$  the losses,  $R_r$  the radiation,  $L_i$  the internal inductance and  $L_A$  the external inductance [2, p. 244]. The model used in the simulation consists of a perfect conductor, therefore  $R_L$  and  $L_A$  are neglected. Instead, the simplified schematic in Figure 4.23b is used, where  $R_A$ ,  $L_A$  and  $C_A$  model the impedance behavior of the antenna.

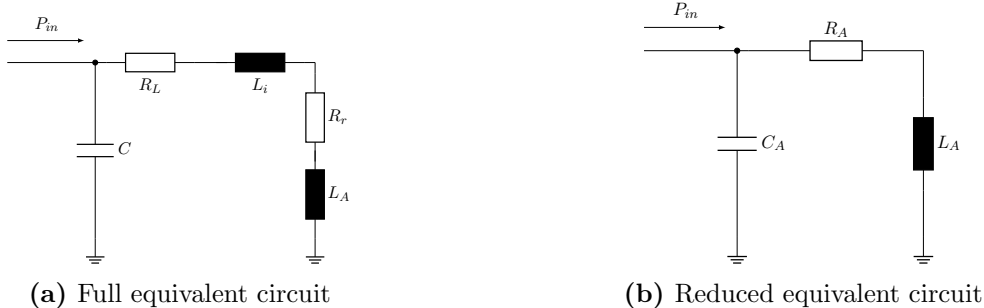


**Figure 4.23** Equivalent circuits of the small loop antenna.

The antenna is placed on a PEC surface in an open space. The inductance and capacitance are derived according to Equation 4.18a, in the case of the circuit in Figure 4.23b this leads to

$$L = 2 \frac{W_m}{I_{in}^2} = \frac{V_{in}^2}{2\omega^2 W_m}, \quad (4.25a)$$

$$C = \frac{2W_c}{V_{in}^2}. \quad (4.25b)$$

Plot inductance and capacitance

In the investigated frequency range, the inductive impedance is significantly smaller than the capacitive impedance, resulting in a predominantly inductive antenna behavior. The model further demonstrates, that the input voltage increases over frequency, therefore increasing the voltage drop across the capacitor. Physically, this corresponds to increased displacement current and electric coupling.

The result cross-checked with

$$L_A = \frac{2\mu_0 l}{\pi} \left[ \ln\left(\frac{l}{w_r}\right) - 0.774 \right], \quad (4.26)$$

which is an approximation of the inductance of a square current loop in free-space [2, p. 245]. There,  $l$  is the length of one side of the antenna, and  $w_r$  is the wire radius. Equation 4.26 yields  $L = 2.32 \text{ nH}$  for the loop antenna in investigation.

The model is extended in Figure 4.24 with an equivalent circuit of the TEM cell, which consists of an equivalent inductance  $L_T = L_{T1} + L_{T2}$  and capacitance  $C_T = C_{T1} + C_{T2}$ . After checking the frequency range in which the equivalent circuit of the TEM cell is valid, it is connected with the circuit of the antenna with  $C_k$ , which models the coupling through displacement current, and the mutual inductances  $M_{A,T1}$  and  $M_{A,T2}$ , which correspond to coupling through induced voltages. The mutual inductances are given as

$$\mathbf{V} = j\omega \begin{bmatrix} L_A & M_{A,T1} & M_{A,T2} \\ M_{T1,A} & L_{T1} & 0 \\ M_{T2,A} & 0 & L_{T2} \end{bmatrix} \mathbf{I}. \quad (4.27)$$

Due to the modeling of the power transfer with  $C_k$ ,  $M_{A,T1}$  and  $M_{A,T2}$ , the radiation resistance of the antenna shown in Figure 4.23b is neglected.

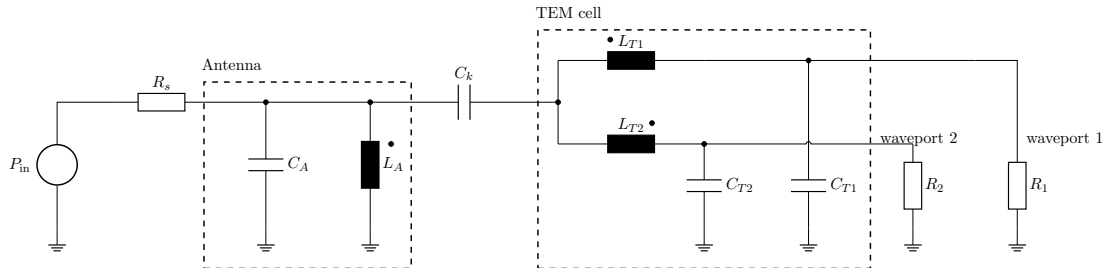


**Figure 4.24** Circuit representing the TEM cell, small loop antenna and their coupling.

The magnetic dipole moment  $\mathbf{m}_m$  is derived by the induced voltage in  $L_{T1}$  and  $L_{T2}$  according to Equation 3.45, and the electric dipole moment  $\mathbf{m}_e$  by the displacement current in  $C_k$  through Equation 3.51. This leads to  $\mathbf{m}_e$  and  $\mathbf{m}_m$  depicted in Figure 4.25, which qualitatively agree with the dipole moments of the loop antenna, but deviate in value by up to 15 %.

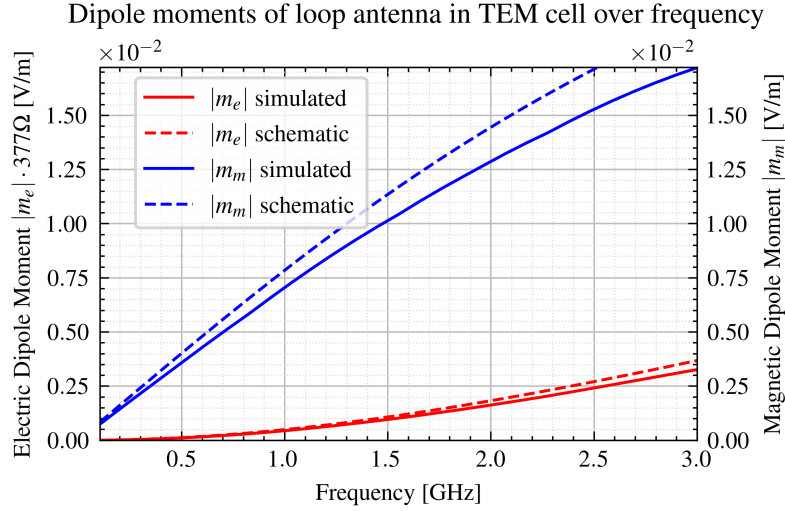


**Figure 4.25** Equivalent dipole moments derived by the equivalent circuit compared to the dipole moments of the loop antenna in Figure 4.18a.

#### 4.4.5 Current distribution on septum and higher order modes

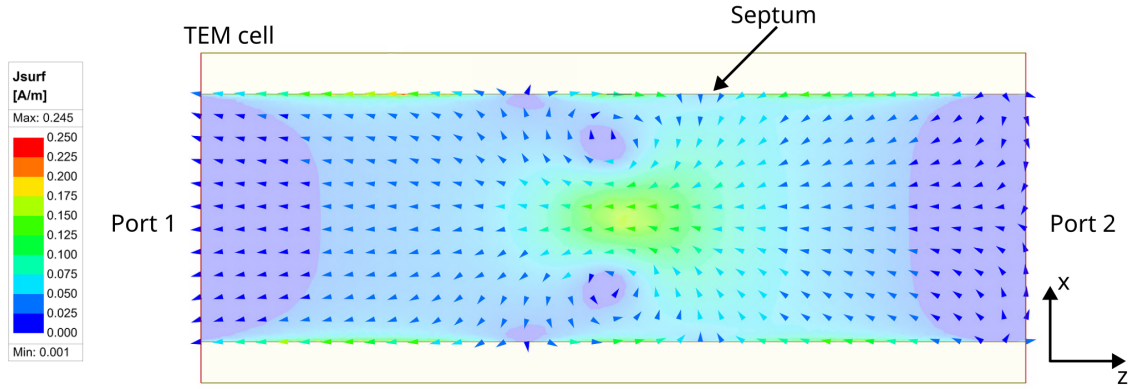
The loop antenna generates a current on the septum of the TEM cell, as shown in Figure 4.26. At a frequency of 3 GHz, the current arrives at the output ports out of phase, as visible in Figure 4.26a. This agrees with Equation 4.15b, which predicts a 180°phase shift in case of a pure magnetic dipole moment.

When the position of the current loop antenna is rotated by 90°and contains an offset of  $x = 7$  mm, the transmission of power is not possible. As visible in the current distribution Figure 4.26b, there is no wave propagation and the surface current remains reactive, forming circles around magnetic fields.

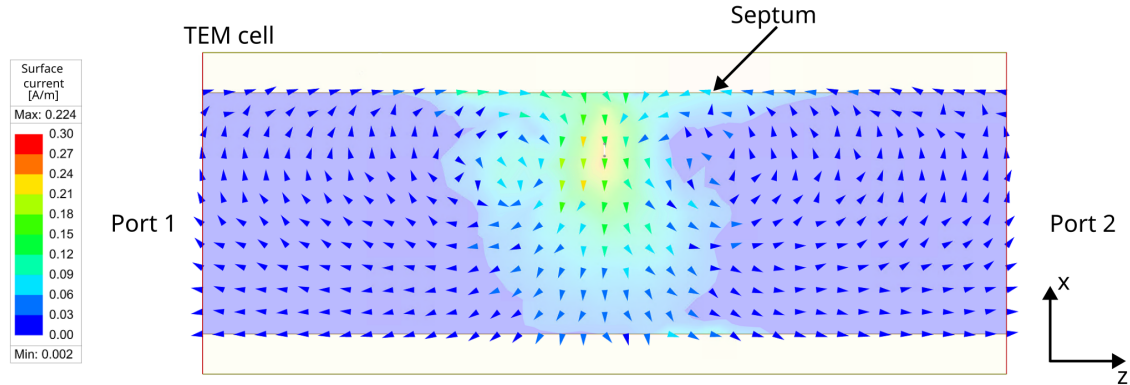
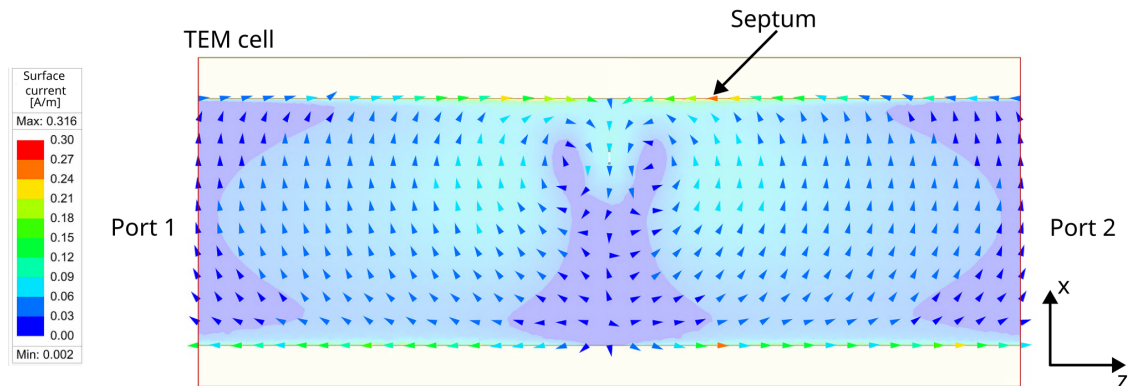
At a frequency of 3.3 GHz, the TE<sub>01</sub> mode start to propagate, visible in Figure 4.26c. A large proportion of the current now reaches the output ports, providing output power, which is in-phase as opposed to the previous case. The propagation occurs due to the alignment of the current loop with the magnetic field lines in longitudinal direction, which leads to power transfer according to Equations (3.44a) and (3.44b). The output power increases sharply, as demonstrated in Figure 4.27.

change jsurf name in legend to surface current

Possible reasons for the deviation in power are numerical inaccuracies or the coupling of the TE<sub>01</sub> mode, which changes the field distribution in a disadvantageous way.



(a) Surface current density of septum induced by loop antenna at 3 GHz

(b) Surface current density of loop antenna with offset of  $x = 7$  mm and a 90 rotation angle at 100 MHz(c) Surface current density of loop antenna with offset of  $x = 7$  mm and a 90 rotation angle at 3.3 GHz**Figure 4.26** Current surface densities at different frequencies, below and above the cut-off frequency of the  $TE_{01}$  mode.

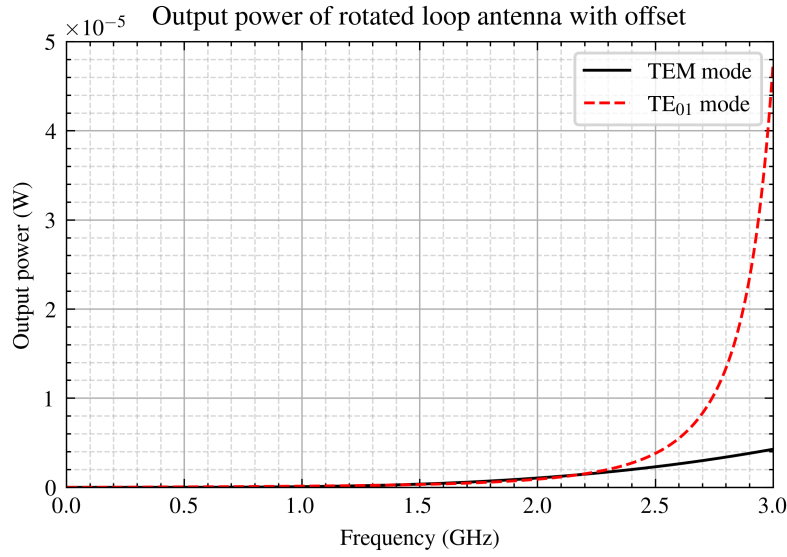


**Figure 4.27** Output power transmitted by the antenna to an output ports through the TEM and TE<sub>01</sub> separately over frequency. TODO: log scale, bigger frequency range

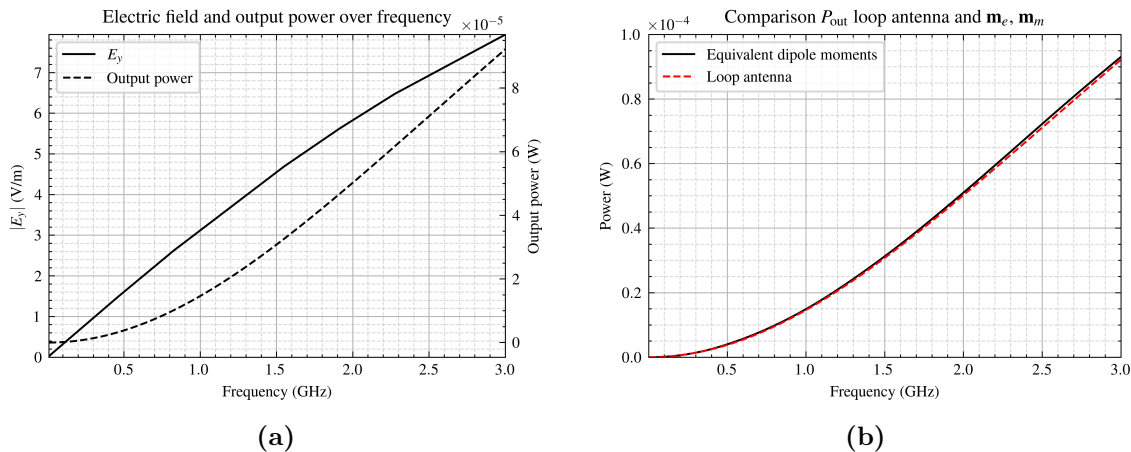


**Figure 4.28** Output power of the loop antenna compared with the output power produced by the dipole moments

## 4.5 Loop antenna with gap

### 4.5.1 Setup and geometrical analysis

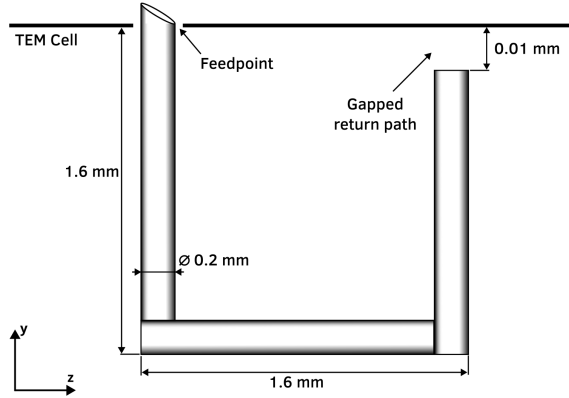


**Figure 4.29** Geometry of loop antenna with a gap in the return path inserted in the TEM cell.

The geometry of the loop antenna with a gap is similar to that of the loop antenna discussed in subsection 4.4. A gap is present with  $10\text{ }\mu\text{m}$  height in the return path, as shown in Figure 4.29. The magnetic coupling is determined with Equations (3.44a) to (3.44b), leading to

$$-\oint_C \boldsymbol{\tau} I(l) \cdot \mathbf{e}_n^\pm dl = - \int_{\text{wire}} \boldsymbol{\tau} I_{\text{wire}}(l) \cdot \mathbf{e}_n^\pm dl - \int_{\text{gap}} \boldsymbol{\tau} I_{\text{gap}}(l) \cdot \mathbf{e}_n^\pm dl. \quad (4.28)$$

The electric current in the gap is  $I_{\text{gap}} = 0\text{ A}$ , while the current in the antenna wire  $I_{\text{wire}}$  is significantly reduced due to the interrupted current path. Consequently, the magnetic coupling between the loop antenna with a gap and the TEM cell is expected to be lower than that of the loop antenna without a gap.

The conductors around the gap act as capacitors, accumulating charges on both sides. This leads to a higher potential in the wire of the antenna. The electric coupling increases significantly, according to Equations (3.50a) to (3.50b). Concluding, the structure of the loop antenna with the gap suggests capacitive behavior with a dominating electric dipole moment.

TODO: Some sources state that electrically small antennas must be either strongly capacitive or inductive. This would mean, that small antennas can always be represented by the same model: Either dominating electric dipole moment in the capacitive antenna case, with a non-linear behavior of the high frequencies, or a magnetic dipole moment with the same property in the inductive antenna case. The frequency, at which the non-linearities occur, depend on the amount of capacitance or inductance, i.e. the Q-factor. A high Q-factor leads to non-linearities in lower cut-off frequencies, and a low Q-factor increases the cut-off frequency. A capacitive antenna with low impedance has a high Q-factor. A inductive antenna with high impedance has a high Q-factor. This can practically be read from the impedance graphs. Can a relation between the impedance/Q-factor and a “cut-off frequency” of the dipole moments be established?

TODO: A little thought experiment on the gapped loop antenna demonstrates why this is the case: If the magnetic dipole moment shall be increased in this antenna, the height of the gap can be decreased to increase the current flow and therefore the magnetic coupling. Ironically, this also increases the amount of charges accumulating on the boundaries of the gap, therefore increasing the electric coupling and capacitive behavior. The capacitive behavior can therefore not change, unless the gap is completely removed. Also, the decrease in gap leads to larger total energy transfer and a higher Q-factor. I suspect, that a high Q-factor of an antenna leads to high energy transfer. This would make sense, because a high Q-factor indicates increased near-field intensities, that would naturally couple with the tem cell. A simulation showing the dipole moments for different gap heights over the frequency would support this claim.

#### 4.5.2 Equivalent dipole moments

The electric dipole moment shown in Figure 4.30a clearly dominates over the magnetic dipole moment. The dipole moments behave non-linearly over the frequency.

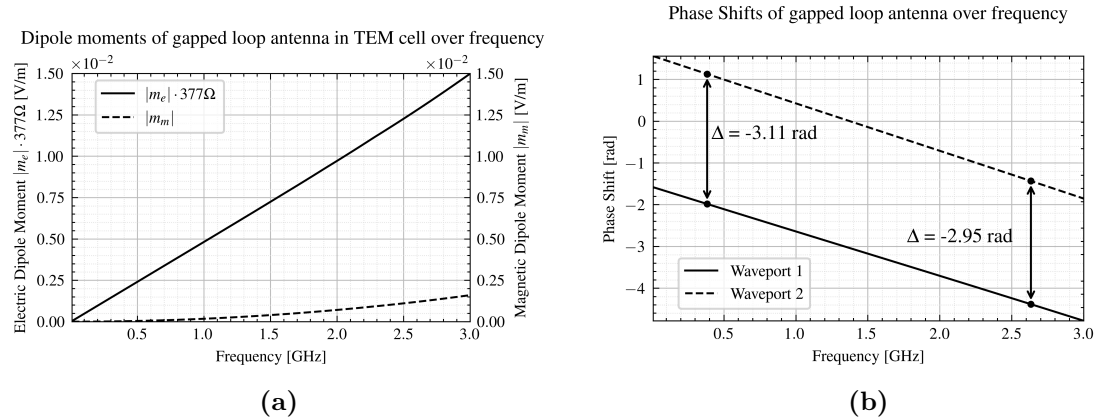


**Figure 4.30** Dipole moments and phase shift of loop antenna

Figure 4.31a demonstrates the effect of the gap height on the dipole moments’ behavior. A larger gap height leads to an decreased charge charge concentration in the gap region,

consequently a smaller magnitude of the electric dipole moment  $\mathbf{m}_e$ . Additionally, it also leads to a decrease in electric current  $\mathbf{J}$  in the antenna, reducing the magnetic dipole moment  $\mathbf{m}_m$ . The reduction in the magnitude of  $\mathbf{m}_e$  and  $\mathbf{m}_m$  with increasing gap height is reflected in the decreasing output power shown in Figure 4.31b.

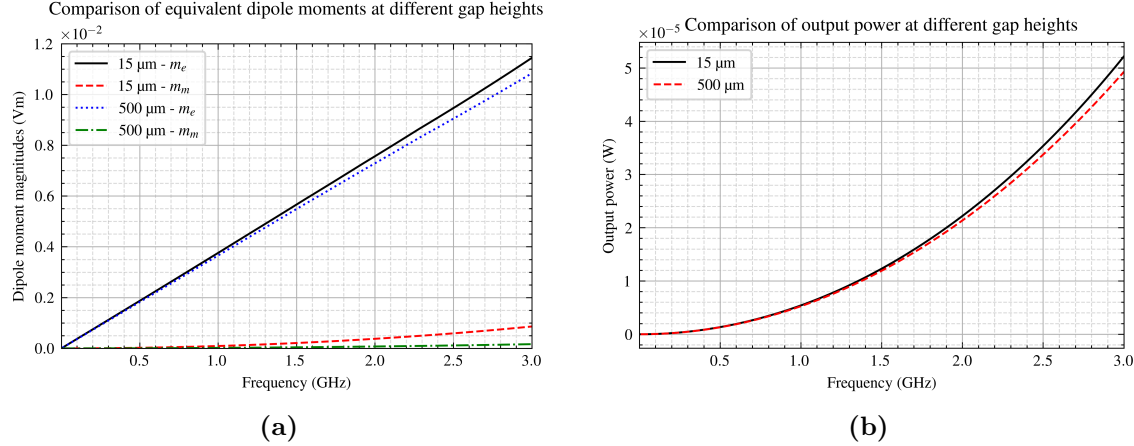


**Figure 4.31** Comparison of dipole moments and output power at different gap heights.

#### 4.5.3 Electrical characteristics

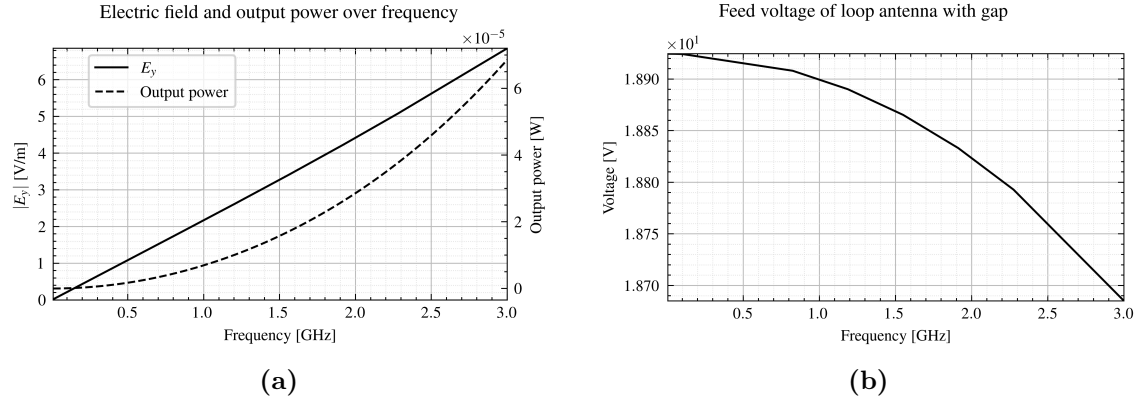
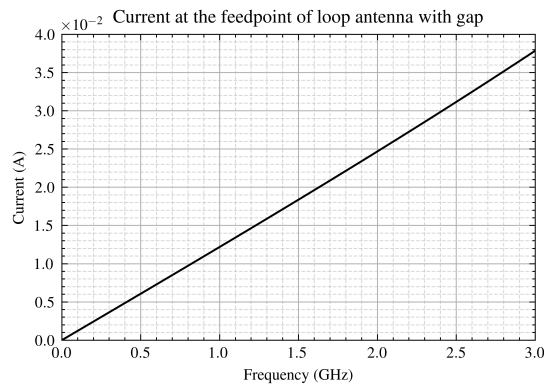
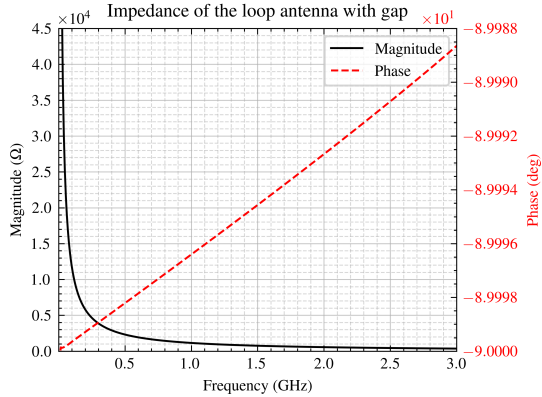


**Figure 4.32** Dipole moments and phase shift of loop antenna

The gap leads to a significant reduction of electric current. Consequently, the impedance of the antenna shows capacitive behavior, as indicated in ???. The energy transfer to the TEM cell occurs primarily by displacement current, explaining the dominating electric dipole moment due to Equation 3.51.



(a) RMS feed current.



(b) Magnitude and phase of impedance

## 4.6 Inverted F-antenna

TODO

The inverted F-antenna (IFA) is modeled in Ansys HFSS as shown in Figure 4.34. It is positioned at the center of the TEM cell, mounted at the top surface. The 5 mm long wire points towards waveport 2. The excitation is a modal wave port. With a maximum dimension of 5 mm, the antenna is electrically small for a frequency of up to 6 GHz, at which it will be a tenth of the wavelength. In this simulation, the antenna is investigated for the frequency of 100 MHz to 1 GHz. The TEM cell has a width of 40 mm and a height of 24 mm and an impedance of  $\sim 50 \Omega$ . The goal is to find equivalent dipole moments of the antenna.

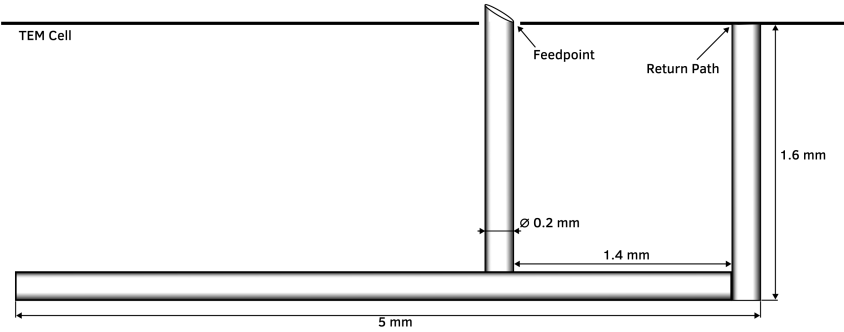
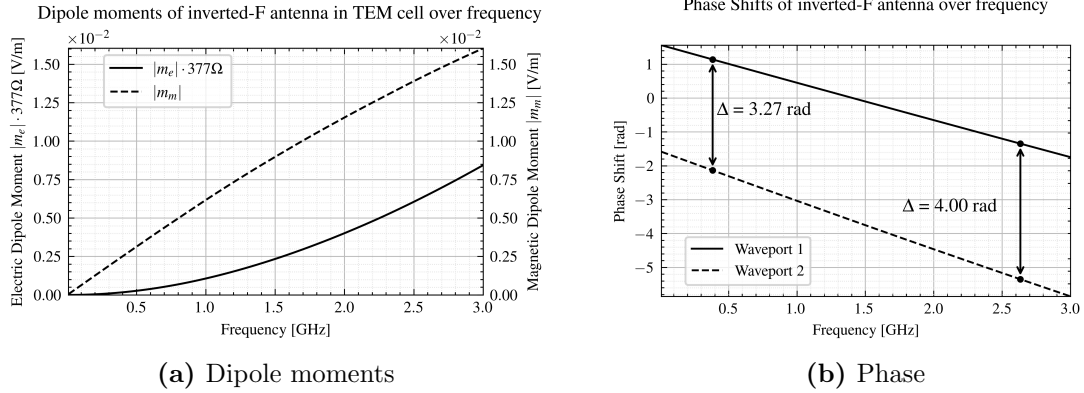


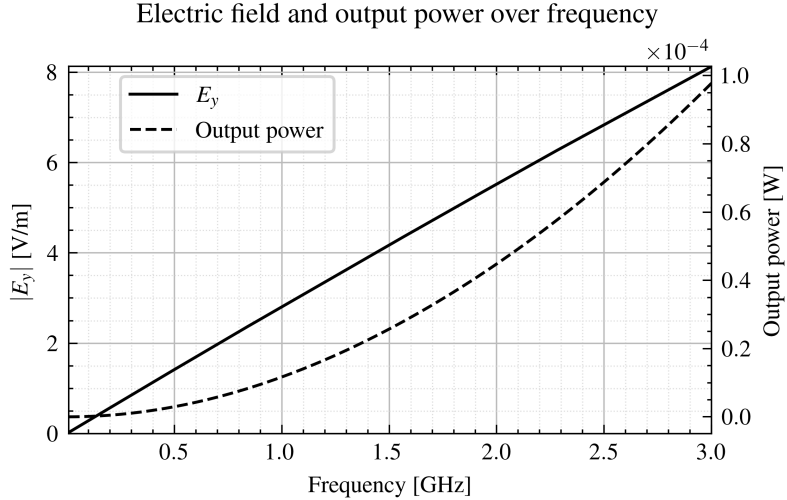
Figure 4.34 Inverted F-antenna used in the simulation

?? shows the dipole moments over frequency. The electric dipole moment  $m_e$  has been normalized to the free-space wave impedance of  $377 \Omega$  to make the dipole moments comparable. This is possible because the dipole moments are interchangeable through the wave impedance [12, p. 414]. The antenna input power has been set to 142588.47 W, because this leads to an output power of 1 W at a frequency of 1 GHz. The magnetic dipole moment is much larger than the electric dipole moment, because the current loop of the antenna is aligned with the TEM cell's magnetic fields, but the line current is not with the TEM electric fields. The magnetic dipole moments rises linearly with the frequency,



(a) Dipole moments

(b) Phase

**Figure 4.35** Dipole moments and phase shift of loop antenna**Figure 4.36** Output power and electric field at output.

which is equal to a quadratic increase of power. Only the TEM modes has been considered in the simulation, as other modes disturb the calculations.

The magnetic coupling with the septum happens due to the alignment of the current loop with the magnetic field of the dominant TEM mode. The antenna is now rotated by 90° around the z-axis, such that the magnetic current loop stands perpendicular to the magnetic TEM fields. ?? demonstrates the phase of the S-parameters, describing the coupling of antenna to waveport 1 and 2. Since the magnetic dipole moment is responsible for a phase between the ports, ?? strongly hints to an absence of it.

?? shows that the electric dipole moment  $m_e$  has stayed the same, while the magnetic dipole moment became zero. Consequently, the overall power transfer between the antenna and the waveports is also much lower.

Repeat for different orientations?  
Change variable name:  
TEM cell height.

The same procedure was repeated with different dipole moments

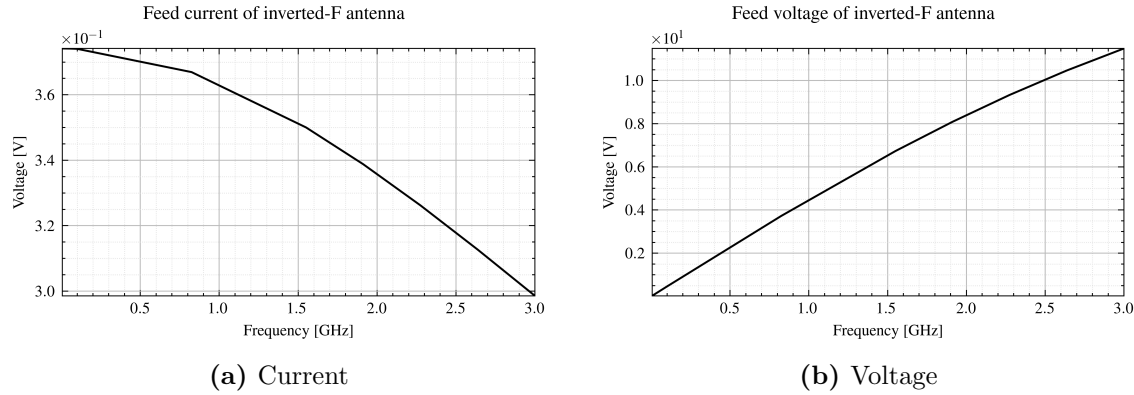


**Figure 4.37** Voltage and current at feedpoint of inverted-F antenna.

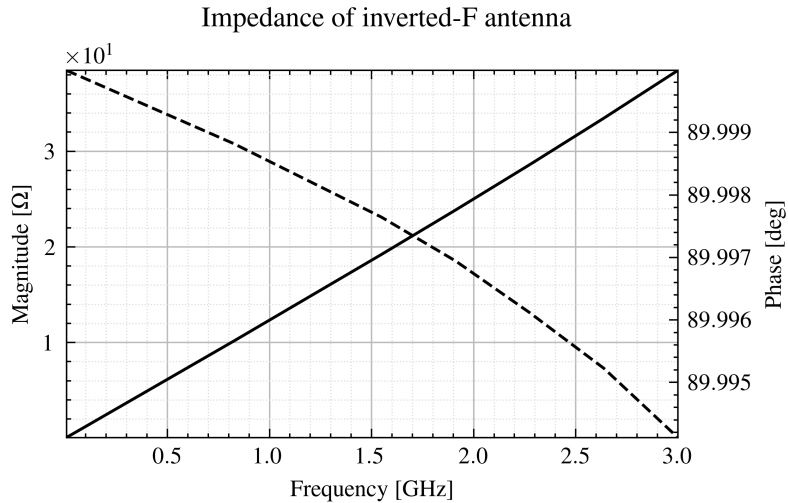


**Figure 4.38** Phase and magnitude of the inverted-F antenna's impedance over frequency.

#### 4.7 Center Fed Monopole Antenna

TODO

The center fed monopole antenna is shown in Figure 4.39. The conducting plane in Figure 4.39 is on the top side of the TEM cell, thus the image is rotated counter-clockwise by 90 degrees. The electric wire with the length of 5 mm points towards the septum. The  $1.1 \times 1.6$  mm loop is again aligned with the magnetic field lines of the TEM mode. The antenna is fed with a power of  $P_{\text{Antenna}} = 127770.39$  W, which once more leads to an output power of  $P_{\text{Out}} = 1$  W at 1 GHz at both output ports.

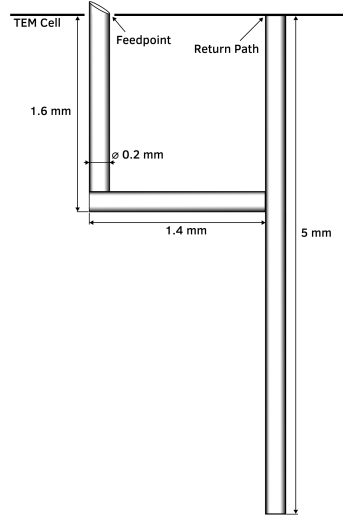


**Figure 4.39** Center fed monopole antenna used in simulation

A question on my mind since the beginning of this thesis: Can how is the magnetic dipole moment influenced by rotating this geometry by 90 degrees? Is the magnetic dipole moment higher or lower than in the rotated loop antenna? With my current knowledge, I suspect that the electric dipole moment leads to current coupling with the TEM cell over displacement current, therefore leading to a smaller magnetic dipole moment than in the case of the loop antenna

The magnitude of  $|S_{A1}| = |S_{A2}|$  in ?? shows stronger coupling. As will be seen below, this is because of an increased electric dipole moment, while the magnetic dipole moment remained the same. Therefore, the center fed monopole antenna couples well electrically with the TEM cell.

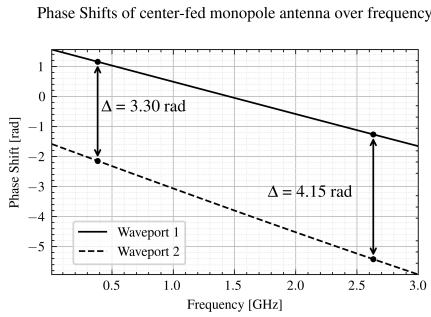


**Figure 4.40** Phase shift

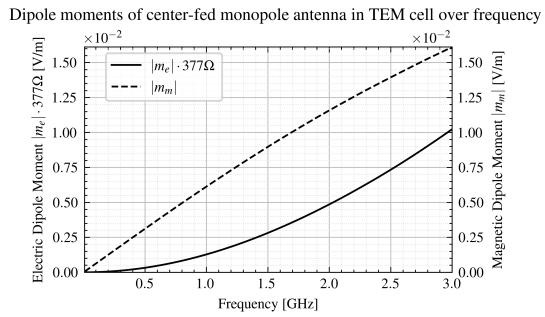


**Figure 4.41** Dipole moments

Figure 4.41 shows that the magnetic dipole moments of the inverted F and center fed monopole antennas are equal. This is due to the same size of the current loops. However, the electric dipole moments increased for the center fed monopole antenna. The alignment of the line current with the TEM cell's electric field causes this. (antenna power = 126549.7191667088 W)

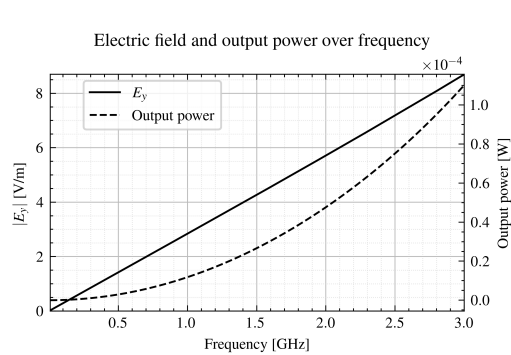
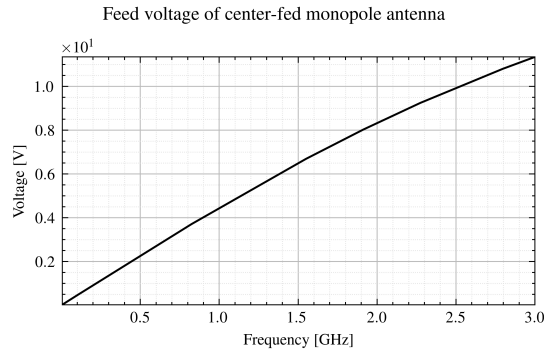
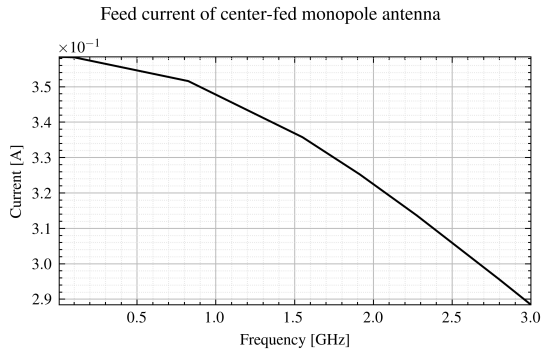


**Figure 4.42** Output power and electric field of center-fed monopole antenna



(a) Voltage



(b) Current

**Figure 4.44** Voltage and current at feedpoint of center-fed monopole antenna.

The output power has been scaled as in the simulation before. This leads to the same electric field magnitude. Therefore, the electric field and output power over frequency plot are the same as in the case for the inverted F antenna, visible in ??.

When rotating this antenna by  $79^\circ$ , the electric and magnetic dipole moment influence the output power by roughly the same amount, as visible in ?? . This makes itself manifest by a phase shift of around  $45^\circ$  between the output powers of the waveports. Interestingly, both the electric and the magnetic dipole moment demonstrate a non-linear behavior.

## 4.8 Dipole Moments

### 4.8.1 Orientation and position in TEM Cell

Figure 4.45 demonstrates the normalized output power of an electric dipole moment pointing in y-direction, and one in z-direction. This simulation only demonstrates the coupling behavior of the dipole moments over frequency, to explain the non-linear coupling of certain antennas. If dipole moments in certain positions and orientations couple with a different proportionality than the standard two dipole moments ( $e_z$  and  $m_y$ ), then the non-linear coupling may be explained that way.

Why does the magnetic moment sink?

CFM at  $90^\circ$  rotation still demonstrates magnetic dipole moment, opposed to current.

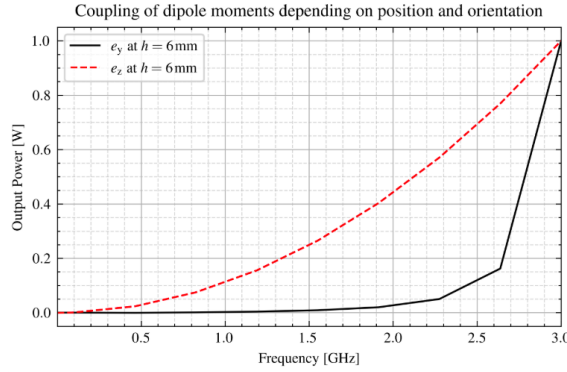


**Figure 4.45** Comparison of normalized output power of electric dipole moments

The electric dipole moment in z-direction  $e_z$  demonstrates the expected behavior: As the frequency rises, this dipole moment rises linearly and thus increases the output power quadratically. The electric dipole moment in y-direction  $e_y$  also increases linearly with frequency, but does not significantly change the output power for the low frequencies. However, as the frequency approaches the cut-off frequency of the next-higher order mode, the coupling rises significantly.

This simulation is repeated where the dipole moments are located at a height of  $h = 6\text{ mm}$ , which is the dead center of the TEM cell, and  $h = 9\text{ mm}$ , which is near the top wall of the TEM cell. The simulation results are similar for both cases.

Most importantly, this simulation shows that the dipole moments have a relation to the frequency independent on their position. While their magnitude themselves do depend on the position, the relation to the frequency does not.

An electric dipole in direction of propagation lead to no power transfer, even in higher order modes. That's because these fields do not overlap with the dipole, for which TM modes would be necessary.

#### 4.8.2 Combining dipole moments with antennas

#### 4.8.3 Application of dipole moments

As show in the previous simulations, antennas may be represented by dipole moments. This can be done in simulation models, which would otherwise be computationally too effortful. The dipole moments may be put into a shielded enclosure around a larger electronic system, as has been done in [17].

Repeat  
Simula-  
tion  
for sev-  
eral other  
dipole  
moment  
positions  
and orienta-  
tions?

### 4.9 Investigation of field regions

In this section, the influence of the field region described in subsection 2.4 on the dipole moments are investigated. Making the TEM cell larger, such that  $k \cdot r > 1$ , is hardly possible without enabling higher-order modes to propagate. On the other hand, making the TEM cell smaller such that  $k \cdot r \ll 1$ , proves to be feasible. The following simulations

are conducted with a TEM cell of dimensions  $a = 10\text{ mm}$  and  $b = 6\text{ mm}$ , visible in Figure 4.46.

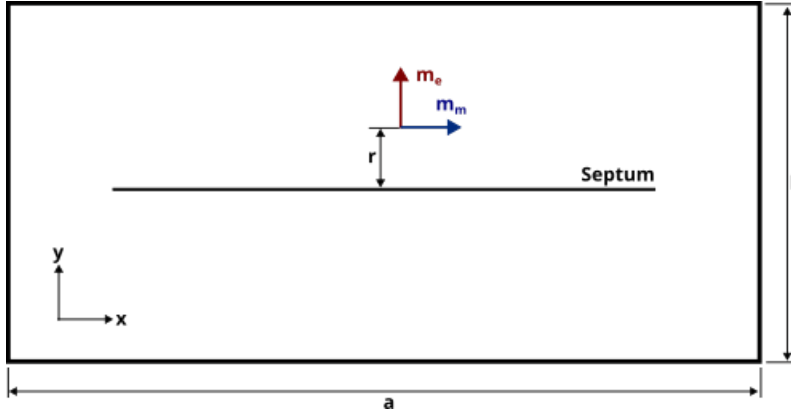


**Figure 4.46** TEM cell containing dipole moments

First, the current loop antenna used in subsection 4.4 is placed in the dead center of the TEM cell. The equivalent dipole moments are shown in Figure 4.47. In the Figure 4.48 next to it, the dipole moments of the same antenna in the larger TEM cell used before ( $a = 40\text{ mm}$  and  $b = 24\text{ mm}$ ) are presented.

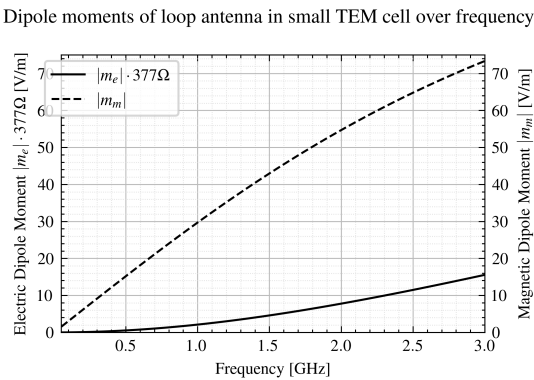


**Figure 4.47** Moments in small TEM cell

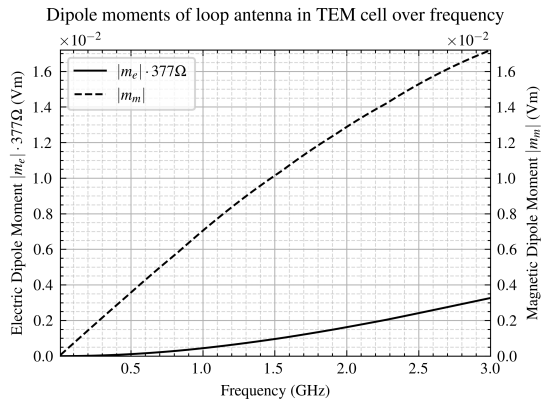


**Figure 4.48** Moments in normal TEM cell

This is done to compare the dipole moments in both cases. While they clearly increased by magnitude in case of the small TEM cell due to better coupling, their non-linear frequency relation still remains. This means that the change of field regions is not the reason for this behavior.

The  $k \cdot r$  factor is determined in Figure 4.49 in the frequency range from 1 MHz to 3 GHz for the small TEM cell. This factor does not surpass 0.1, thus fulfilling the requirement  $k \cdot r \ll 1$  for this investigation. For comparison, the  $k \cdot r$  factor over a wider frequency range are shown in Figure 4.49 for the normal sized TEM cell ( $a = 40\text{ mm}$  and  $b = 24\text{ mm}$ ) and a degenerately high TEM cell ( $a = 10\text{ mm}$  and  $b = 44\text{ mm}$ ). The high TEM does not have

The electric field approximation in the python code is based on the large TEM cell. Therefore, the magnitude of the dipole moments of the small TEM cell are probably off.

Insert kr, describe where r is measured, describe why the suspicion was that kr could influence this and

a port impedance of  $50 \Omega$ , and is an attempt to achieve a large  $k \cdot r$  factor without higher-order modes propagating. The markers in Figure 4.50 indicate the cut-off frequency, in which the next higher-order mode propagates. They demonstrate, that even in the high TEM cell a  $k \cdot r = 1$  is not achieved.

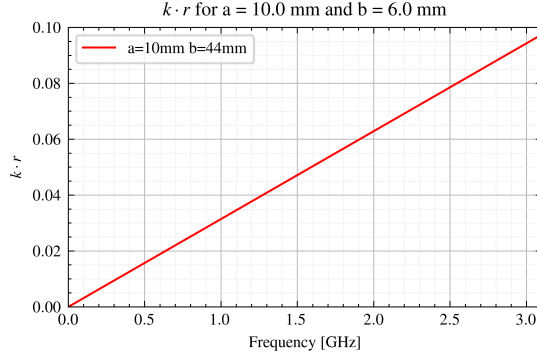


**Figure 4.49**  $k \cdot r$  in small TEM cell

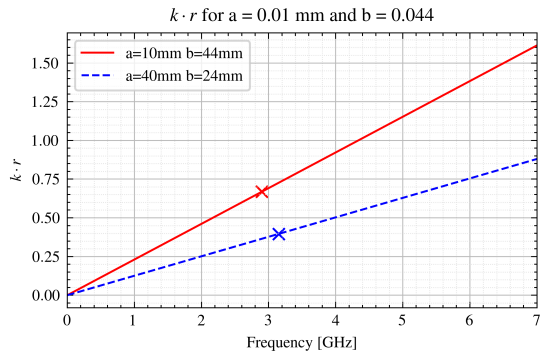


**Figure 4.50**  $k \cdot r$  for other TEM cells

Now, three simulations are conducted with different excitation sources in the small TEM cell:

Fix figures: Titles and Legends

- The current loop
- The equivalent dipole sources  $e_z$  and  $m_m$  of the current loop
- The equivalent magnetic dipole source  $m_m$ , neglecting  $e_z$

Figure 4.51 shows the output power over frequency normalized to 1 W for all three constellations. The normalization is done to qualitatively discuss the frequency-dependent coupling behavior. Figure 4.52 demonstrates the phase shift between the powers at the two waveports over frequency.

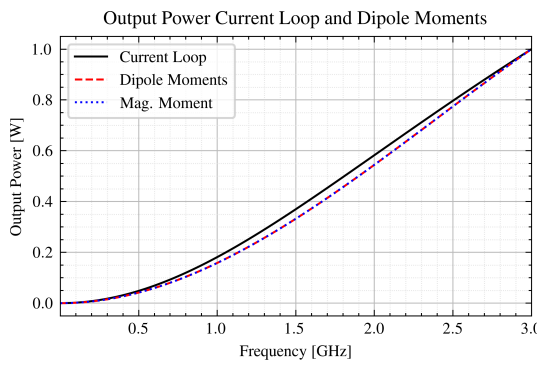


**Figure 4.51** Output powers

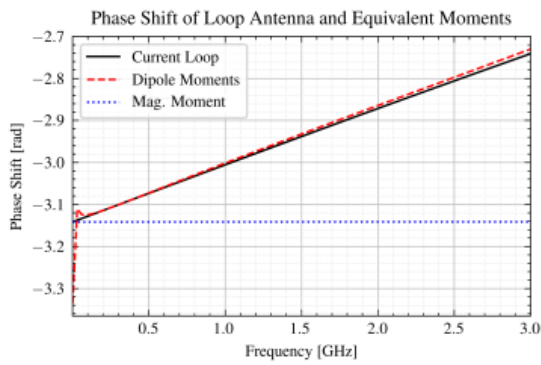


**Figure 4.52** Phase shifts

The frequency dependent behavior of the output power does not change depending on the type of dipole moment used. This is significant, because this shows that the dipole moments do not exhibit different coupling behaviors in the TEM cells. This is further proven in the phase shift plots. The magnetic dipole moment causes a constant phase

shift of  $-\pi$ . If this was not the case, this would mean that the coupling behavior of the magnetic dipole moment in the TEM cell would change. Since the opposite is the case, this poses as good evidence against arguments of change in field regions causing the non-linear dipole moment behavior. Instead, it is very likely to be caused by the geometry of the antenna.

#### 4.10 Shielding materials

Rest of shielding material section still TODO

##### 4.10.1 Shielding effectiveness of graphite

The reference power  $P_{\text{ref}}$  has been set to 1 W. Using Equation 3.62 and the S-parameters from the simulation results,  $P_{\text{load}}$  may be determined. Figure 4.53 demonstrates the shielding effectiveness of graphite in dB  $SE_{\text{dB}}$  over the shielding material thickness. The solution frequency is 500 MHz. A frequency sweep shows that the reflection coefficient  $S_{11}$  does not depend much on the frequency.

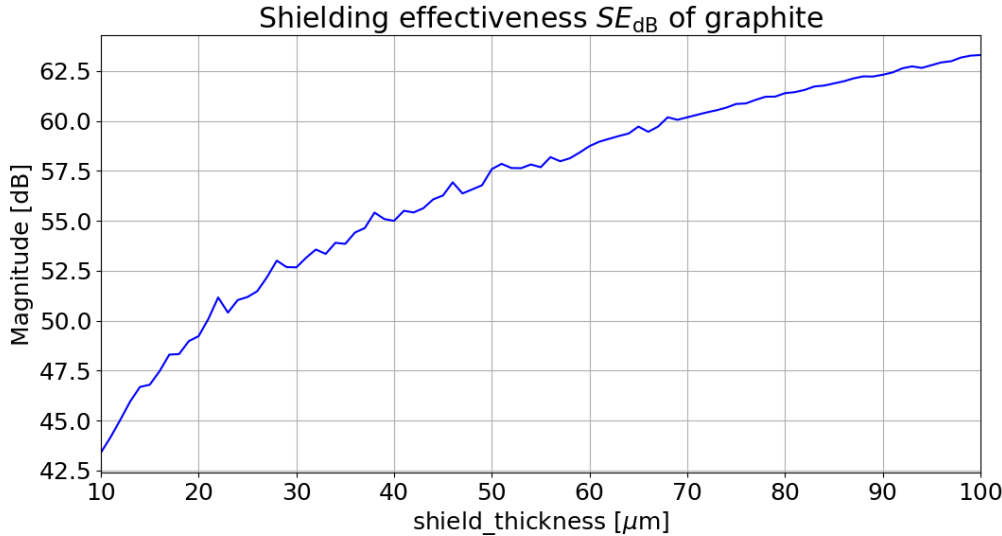


**Figure 4.53** Shielding effectiveness of graphite

The components of  $SE_{\text{dB}}$  are determined according to Equation 3.53.

##### 4.10.2 Shield effectiveness of FR4

The FR4 has a relative permittivity of  $\epsilon_r = 4.4$ . According to Equation 3.55, the relative wave impedance is  $Z = 0.476$ . This leads to a reflection coefficient of  $R = -0.355$  by Equation 3.54.

The reflection coefficient  $|S_{11}| = 0.045$ .

Forward transmission coefficient	Empty aperture	aperture filled with FR408
Waveport 1 to 3 $S_{13}$	-83.80 dB, -144.96°	-85.27 dB, -155.79°
Waveport 1 to 4 $S_{14}$	-90.31 dB, -144.96°	-87.14 dB, 25.00°

**Table 2** Forward transmission coefficients

#### 4.10.3 Dual TEM Cell

A simulation setup of a dual TEM cell is created. A rectangular aperture with a side length of  $l = 5\text{ cm}$ , inspired by [28], connects both TEM cells. One waveport 1, as in Figure 3.13, is excited with a power of  $P = 1\text{ W}$ . The simulation is conducted, leaving the aperture open. A second one determines the coupling of the waveports, when the aperture is filled with a graphite sheet with a thickness of  $t = 50\text{ }\mu\text{m}$ .

At a frequency of  $f = 500\text{ MHz}$ , the coupling between waveport 1 to the waveports 3 and 4 of the receiving TEM cell is shown in Table 2. Only one frequency point is investigated, as the results stay roughly constant over the inspected frequency range from 100 MHz to 1 GHz.

Using Equation 3.63a and Equation 3.63b leads to the shielding effectiveness for electric coupling  $SE_{\text{dB}}^{\text{e}} = 19.07\text{ dB}$  and magnetic coupling  $SE_{\text{dB}}^{\text{m}} = -9.22\text{ dB}$ . To get the sum  $P_{\text{sum}}$  and difference  $P_{\text{diff}}$  of powers, the phase of the signals have to be considered. With unit input power at the transmitting TEM cell, Equation 4.29a and Equation 4.29b are used for this purpose [23].

$$P_{\text{sum}} = (S_{13} + S_{14})(S_{13} + S_{14})^* \quad (4.29\text{a})$$

$$P_{\text{diff}} = (S_{13} - S_{14})(S_{13} - S_{14})^* \quad (4.29\text{b})$$

Indicated by the phase shift of roughly  $180^\circ$ , the coupling between the TEM cells occur mainly due to magnetic dipoles. Due to the relative permittivity of  $\epsilon_r = 3.66$  and the relative permeability of  $\mu_r \approx 1$  of the shielding material, the magnetic fields dominate. This leads to a energy transfer mainly due to magnetic dipole moments. The overall shielding effectiveness  $SE_{\text{dB}} = \text{Equation 4.30}$ .

$$P_{\text{total}} = |S_{13}|^2 + |S_{14}|^2 \quad (4.30)$$

Why -8dB difference in empty aperture? Explained in [28]

negative SE possible? Redo Simulations with finer Mesh around aperture

One port receives overall more power due to the material. Is it because of the magnetic/electric dipoles in it? Check mesh around the small aperture.

Const

## References

- [1] Constantine A. Balanis. *Advanced Engineering Electromagnetics*. John Wiley Sons, 2012.
- [2] Constantine A. Balanis. *Antenna theory: Analysis and design. Buch Constantine A. Balanis*. 3rd. Wiley, 1997.
- [3] Z. Cendes and D. Shenton. “Adaptive mesh refinement in the finite element computation of magnetic fields”. In: *IEEE Transactions on Magnetics* 21.5 (1985), pp. 1811–1816. DOI: 10.1109/TMAG.1985.1063929.
- [4] Z.J. Cendes. “Vector finite elements for electromagnetic field computation”. In: *IEEE Transactions on Magnetics* 27.5 (1991), 3958–3966. DOI: 10.1109/20.104970.
- [5] Z.J. Cendes and J.-F. Lee. “The transfinite element method for modeling MMIC devices”. In: *1988., IEEE MTT-S International Microwave Symposium Digest* (1988), 623–626. DOI: 10.1109/mwsym.1988.22111.
- [6] Robert E. Collin. *Field theory of guided waves*. IEEE Press, 2015.
- [7] Saju Daniel and Sabu Thomas. “Shielding Efficiency Measuring Methods and Systems”. In: *Advanced Materials for Electromagnetic Shielding: Fundamentals, Properties, and Applications*. 2019, pp. 61–87. DOI: 10.1002/9781119128625.ch4.
- [8] David J. Griffiths. *Introduction to electrodynamics*. Cambridge University Press, 2024.
- [9] C. Groh et al. “TEM waveguides for EMC measurements”. In: *IEEE Transactions on Electromagnetic Compatibility* 41.4 (1999), pp. 440–445. DOI: 10.1109/15.809846.
- [10] Robert C. Hansen and Robert E. Collin. *Small antenna handbook*. Wiley, 2013.
- [11] K.H. Huebner et al. *The Finite Element Method for Engineers*. A Wiley-Interscience publication. Wiley, 2001. ISBN: 9780471370789. URL: <https://books.google.at/books?id=f3MZE1BYq3AC>.
- [12] John David Jackson. *Classical Electromagnetism*. 2nd ed. Wiley.
- [13] J.P. Karst, C. Groh, and H. Garbe. “Calculable field generation using TEM cells applied to the calibration of a novel E-field probe”. In: *IEEE Transactions on Electromagnetic Compatibility* 44.1 (2002), pp. 59–71. DOI: 10.1109/15.990711.
- [14] M. Koch, C. Groh, and H. Garbe. “Exact Determination of Resonant Frequencies in TEM Cells”. In: *13th International Zurich Symposium and Technical Exhibition on Electromagnetic Compatibility*. 1999, pp. 653–658. DOI: 10.23919/EMC.1999.10791592.
- [15] Galen H Koepke. In: *Theory and measurements of radiated emissions using a TEM cell* (1989). DOI: 10.6028/nist.tn.1326.
- [16] Dominik Kreindl et al. “Evaluation of an analytical equivalent Hertzian dipole representation in tem cells applying the finite element method”. In: *IEEE Transactions on Magnetics* 60.3 (2024), 1–4. DOI: 10.1109/tmag.2023.3324698.
- [17] Dominik Kreindl et al. “Measurement and Simulation Methodology for Characterizing the Shielding Effectiveness of Coating Materials for Optical Sensors”. In: *2023 International Symposium on Electromagnetic Compatibility – EMC Europe*. 2023, pp. 1–6. DOI: 10.1109/EMCEurope57790.2023.10274360.
- [18] J.-F. Lee, D.-K. Sun, and Z.J. Cendes. “Full-wave analysis of dielectric waveguides using tangential vector finite elements”. In: *IEEE Transactions on Microwave Theory and Techniques* 39.8 (1991), pp. 1262–1271. DOI: 10.1109/22.85399.

- [19] J.F. Lee, D.K. Sun, and Z.J. Cendes. “Tangential vector finite elements for electromagnetic field computation”. In: *IEEE Transactions on Magnetics* 27.5 (1991), pp. 4032–4035. DOI: [10.1109/20.104986](https://doi.org/10.1109/20.104986).
- [20] M.F.N. Mohsen. “Some details of the Galerkin Finite Element Method”. In: *Applied Mathematical Modelling* 6.3 (1982), 165–170. DOI: [10.1016/0307-904x\(82\)90005-1](https://doi.org/10.1016/0307-904x(82)90005-1).
- [21] Cristian MORARI and Cristian BĂLAN. In: *Methods for determining shielding effectiveness of materials* (2015).
- [22] D. Shenton and Z. Cendes. “Three-dimensional finite element mesh generation using Delaunay tessellation”. In: *IEEE Transactions on Magnetics* 21.6 (1985), 2535–2538. DOI: [10.1109/tmag.1985.1064165](https://doi.org/10.1109/tmag.1985.1064165).
- [23] Ippalapalli Sreenivasiah, David Chang, and Mark Ma. “Emission characteristics of electrically small radiating sources from tests inside a tem cell”. In: *IEEE Transactions on Electromagnetic Compatibility* EMC-23.3 (1981), 113–121. DOI: [10.1109/temc.1981.303930](https://doi.org/10.1109/temc.1981.303930).
- [24] GILBERT STRANG. *Analysis of the finite element method*. WELLESLEY-CAMBRIDGE Press, 2018.
- [25] Son Xuat Ta, Ikmo Park, and Richard W. Ziolkowski. “Crossed Dipole Antennas: A review”. In: *IEEE Antennas and Propagation Magazine* 57.5 (2015), pp. 107–122. DOI: [10.1109/MAP.2015.2470680](https://doi.org/10.1109/MAP.2015.2470680).
- [26] John C Tippet, David C Chang, and Myron L Crawford. In: *An analytical and experimental determination of the cutoff frequencies of higher-order te modes in a Tem cell* (1976). DOI: [10.6028/nbs.ir.76-841](https://doi.org/10.6028/nbs.ir.76-841).
- [27] C.M. Weil and L. Gruner. “High-order mode cutoff in rectangular striplines (short papers)”. In: *IEEE Transactions on Microwave Theory and Techniques* 32.6 (1984), 638–641. DOI: [10.1109/tmtt.1984.1132745](https://doi.org/10.1109/tmtt.1984.1132745).
- [28] Perry F Wilson. In: *Excitation of a tem cell by a vertical electric Hertzian dipole* (1981). DOI: [10.6028/nbs.tn.1037](https://doi.org/10.6028/nbs.tn.1037).
- [29] Perry F. Wilson, David C. Chang, and Mark T. Ma. “Input Impedance of a Probe Antenna in a TEM Cell”. In: *IEEE Transactions on Electromagnetic Compatibility* EMC-26.4 (1984), pp. 154–161. DOI: [10.1109/TEMC.1984.304216](https://doi.org/10.1109/TEMC.1984.304216).
- [30] Perry F. Wilson and Mark T. Ma. “Shielding-Effectiveness Measurements with a Dual TEM Cell”. In: *IEEE Transactions on Electromagnetic Compatibility* EMC-27.3 (1985), pp. 137–142. DOI: [10.1109/TEMC.1985.304277](https://doi.org/10.1109/TEMC.1985.304277).
- [31] Perry F. Wilson and Mark T. Ma. “Simple approximate expressions for higher order mode cutoff and resonant frequencies in TEM cells”. In: *IEEE Transactions on Electromagnetic Compatibility* 28.3 (1986), 125–130. DOI: [10.1109/temc.1986.4307269](https://doi.org/10.1109/temc.1986.4307269).